

SIZE AND COMPOSITION EFFECTS ON IONIC CONDUCTIVITY:
DOPED CERIA BULK CERAMICS AND THIN FILM

By

ROBERT MARTIN KASSE

A THESIS PRESENTED TO THE GRADUATE SCHOOL
OF THE UNIVERSITY OF FLORIDA IN PARTIAL FULFILLMENT
OF THE REQUIREMENTS FOR THE DEGREE OF
MASTER OF SCIENCE

UNIVERSITY OF FLORIDA

2013

© 2013 Robert Martin Kasse

To my future self

ACKNOWLEDGMENTS

Though it is written by an individual, it would be nearly impossible to complete all of the work that goes into a thesis without significant help from others. Whether helping out with experiments, giving you time and space to struggle and figure things out on your own, or helping to keep you sane despite spending far too much time in the lab, a thesis is very much a group effort. I could simply list the names of everyone who helped me throughout the last few years but I feel there are a few who deserve more recognition than that.

First, I would like to thank my advisor Dr. Juan C. Nino for giving me the opportunity to feed the curiosity I had for performing scientific research. Throughout my three years with NRG he has trusted me to conduct my experiments in my own way at my own pace while at the same time providing necessary guidance to prevent me from getting too far off track and wasting my time. Had I not been given this opportunity I may have never discovered how much I enjoy (and at the same time hate) conducting research and would not have realized that this is what I would like to someday make a career out of.

Of course, I also need to thank my parents for helping me get to where I am today. Never once, have they questioned the decisions I have made regarding my education and their love and support have made these past few years easier than they could have been otherwise.

There have also been a number of students and professors who have helped me with my research that deserve special mention, and they are as follows: Dr. Kyeong-Won Kim and Dr. David Norton (PLD), Dr. Nicholas Rudawski and Dr. Kevin Jones (TEM), Mina Hanna and Dr. Scott Perry (AFM), and Dr. Jacob Jones and various

students in his research group for the use of their lab and equipment. This work could not have been completed without the use of equipment located at MAIC and NRF. I also need to give a special thanks to Microsoft Paint.

Along the way there have been many times when I needed to ask my fellow group members for help with something related to my project and they were more than willing (most of the time) to provide that help. This list of people includes, but is not limited to: Chris Turner, Trey Davis, Roberto Esquivel, Don Moore, Paul Johns, Hyuksu Han, Brittnee Mound, George Baure, Mehrad Mehr, Sasmit Gokhale, Satyajit Phadke, and Wei Qiu. However, it is the time spent doing everything except working on science that I will remember most when looking back on my time here. Whether it was Ninolympics, Lab Basketball, It's Kind of a Big Deal Friday, Food Truck Friday, Château L'George, or just general nonsensical conversations about nothing in particular, it was these moments that kept me from going crazy and getting fed up with research.

TABLE OF CONTENTS

	<u>page</u>
ACKNOWLEDGMENTS.....	4
LIST OF FIGURES.....	10
LIST OF ABBREVIATIONS.....	13
LIST OF SYMBOLS	15
ABSTRACT	17
CHAPTER	
1 INTRODUCTION	19
1.1 Statement of Problem and Motivation.....	19
1.2 Scientific Approach	19
1.3 Organization of Thesis	21
1.4 Contributions to the Field	21
2 BACKGROUND	23
2.1 Solid Oxide Fuel Cells.....	23
2.2 Structure of Relevant Materials.....	30
2.2.1 Ceria.....	30
2.2.2 Sapphire	34
2.2.3 Platinum	35
2.3 Electrochemical Impedance Spectroscopy	35
2.4 Thin Film Deposition	38
2.4.1 Pulsed Laser Deposition.....	38
2.4.2 DC Sputtering.....	44
3 EXPERIMENTAL PROCEDURES.....	46
3.1 Preparation of Thin Film Samples.....	46
3.1.1 Substrate Cleaning.....	46
3.1.2 Deposition of Highly Oriented Pt Layer Using DC Sputtering	46
3.1.3 Deposition of Highly Oriented $\text{Nd}_{0.1}\text{Ce}_{0.9}\text{O}_{2.5}$ Layer Using Pulsed Laser Deposition	47
3.1.4 Deposition of Pt Top Electrodes Using DC Sputtering.....	47
3.2 Preparation of Bulk Samples	47
3.2.1 Powder Synthesis.....	48
3.2.2 Formation of Ceramic Green Body	48
3.2.3 Pellet Sintering	48
3.3 Sample Characterization.....	49

3.3.1 Impedance Spectroscopy	49
3.3.1.1 Thin Film Samples	49
3.3.1.2 Bulk Samples	49
3.3.2 X-ray Diffraction.....	50
3.3.3 Profilometry	51
3.3.4 Transmission Electron Microscopy	51
3.3.5 Atomic Force Microscopy	52
3.3.6 Scanning Electron Microscopy	52
4 HIGHLY ORIENTED Nd_{0.1}Ce_{0.9}O_{2-δ} THIN FILMS ON Pt BOTTOM ELECTRODES	54
4.1 Introduction	54
4.2 Structural Characterization	58
4.3 Ionic Conductivity	63
4.4 Summary and Conclusions	65
5 IONIC CONDUCTIVITY OF Sm_xNd_yCe_{0.9}O_{2-δ}.....	66
5.1 Introduction	66
5.2 Phase Analysis and Microstructural Characterization	67
5.3 Ionic Conductivity	69
5.4 Conclusions	74
6 IONIC CONDUCTIVITY ACROSS THE DISORDER-ORDER PHASE TRANSITION IN THE NdO_{1.5}-CeO₂ SYSTEM	75
6.1 Introduction	75
6.2 Phase and Structural Analysis	78
6.2.1 X-ray Diffraction.....	78
6.2.2 Neutron Diffraction.....	81
6.3 Microstructural Analysis	85
6.4 Ionic Conductivity	86
6.5 Conclusions	92
7 SUMMARY AND FUTURE WORK	93
7.1 Summary	93
7.2 Future Work	94
7.2.1 Thin Films	94
7.2.2 Bulk	95
APPENDIX	
A NDC FILMS ON VARIOUS SUBSTRATES	97
B FITTING IMPEDANCE DATA USING ZVIEW	101

LIST OF REFERENCES 103
BIOGRAPHICAL SKETCH..... 113

LIST OF TABLES

<u>Table</u>		<u>page</u>
5-1	Activation energy, pre-exponential coefficient, configurational entropy, and effective index values for all of the compositions studied.	73
6-1	Detailed crystallographic information for $\text{Nd}_{0.55}\text{Ce}_{0.45}\text{O}_{1.725}$ obtained by Rietveld refinement.....	82
6-2	Grain sizes of the sintered pellets of different compositions.	86

LIST OF FIGURES

<u>Figure</u>	<u>page</u>
2-1 Schematic depiction of the operation of a solid oxide fuel cell.....	23
2-2 Large-area electrolyte supported YSZ-based FlexCells by Nextech.	24
2-3 Ragone plot comparing the specific power and specific energy of various devices to SOFCs.....	26
2-4 The log of ionic conductivity versus temperature for various fluorite structured oxides.	27
2-5 Cross-sectional SEM micrographs of the anode-supported single cells with GDC electrolyte films.....	29
2-6 The schematics show the crystal structure of doped and undoped ceria.	31
2-7 The C-type rare earth structure, space group $Ia\bar{3}$	32
2-8 Schematic depiction of the space charge region near grain boundaries in doped ceria.....	33
2-9 Concentration profile obtained via atom probe analysis of various species near a grain boundary in GDC.....	34
2-10 Various views of the sapphire crystal structure.....	34
2-11 Various views of the FCC crystal structure of platinum.	35
2-12 Plot showing the relationship between impedance and phase angle.....	36
2-13 Generic Nyquist plot showing the grain core, grain boundary, and electrode impedance arcs for a polycrystalline sample.	37
2-14 Equivalent circuit used to fit a Nyquist plot of complex impedance.....	37
2-15 Schematic view of the PLD process.	39
2-16 Bright white plume generated by the ablation of an $Nd_{0.1}Ce_{0.9}O_{2-\delta}$ target by a 248 nm wavelength KrF laser.....	41
2-17 Schematic view of various growth modes.....	42
2-18 Schematic showing the relationship between substrate temperature, gas pressure, and film morphology	43

4-1	Schematic illustration of films with single crystalline, columnar grain, and polycrystalline microstructures.....	55
4-2	Schematic illustration of electroding configurations for in-plane (left) and across-plane (right) electrical measurements of thin film samples.	55
4-3	X-ray diffraction pattern of a 43 nm thin film sample as compared to the theoretical patterns for Al ₂ O ₃ , Pt, and 10% Nd-doped ceria	59
4-4	X-ray diffraction patterns for thin film samples of different thicknesses ranging from 4-190 nm.	60
4-5	Convergent beam electron diffraction (left), selected area electron diffraction (center inset), and high resolution cross-sectional TEM (right).....	61
4-6	Atomic force microscopy topography maps and line scans of a Pt layer (top) and a 43 nm NDC film (bottom)	62
4-7	Typical Nyquist plot obtained from impedance measurements of thin film samples	64
4-8	Arrhenius plot of grain ionic conductivity for 10% Nd-doped ceria.....	64
4-9	Plot of the log of conductivity versus temperature	65
5-1	X-ray diffraction patterns for Sm _x Nd _y Ce _{0.9} O _{2-δ}	68
5-2	SEM image of a fracture surface of Sm _{0.025} Nd _{0.075} Ce _{0.9} O _{2-δ} showing the typical microstructure of all samples.....	69
5-3	Arrhenius plot of grain ionic conductivity for all nine compositions investigated in the Sm _x Nd _y Ce _{0.9} O _{2-δ} system.	73
5-4	Plot of grain ionic conductivity versus dopant concentration for Sm _x Nd _y Ce _{0.9} O _{2-δ} from 400-700°C.....	74
6-1	The ternary phase diagram of NdO _{1.5} -SmO _{1.5} -CeO ₂ at room temperature reported by T. Vanderah.....	76
6-2	XRD patterns of the calcined powders of Nd _x Ce _{1-x} O _{2-δ}	79
6-3	Lattice parameters of Nd _x Ce _{1-x} O _{2-δ} (0 ≤ x ≤ 0.45) as a function of Nd content....	80
6-4	Observed neutron diffraction profiles for 0.35 ≤ Nd ≤ 0.55.	83
6-5	Observed (cross), calculated (continuous line), and difference neutron diffraction profiles for Nd _{0.35} Ce _{0.65} O _{1.825} are shown.....	83

6-6	Observed (cross), calculated (continuous line), and difference neutron diffraction profiles for $\text{Nd}_{0.55}\text{Ce}_{0.45}\text{O}_{1.725}$ are shown.....	84
6-7	SEM micrograph for sintered pellets of $\text{Nd}_x\text{Ce}_{1-x}\text{O}_{2-\delta}$	86
6-8	Nyquist plot of impedance for $\text{Nd}_{0.25}\text{Ce}_{0.75}\text{O}_{1.875}$, measured at 250°C in air.	88
6-9	Arrhenius plot of grain conductivity of $\text{Nd}_x\text{Ce}_{1-x}\text{O}_{2-\delta}$ ($0 \leq x \leq 0.55$).	88
6-10	Grain conductivity of $\text{Nd}_x\text{Ce}_{1-x}\text{O}_{2-\delta}$ ($0 \leq x \leq 0.55$) as a function of Nd concentration (x) at temperatures from 450-700°C.....	89
6-11	Activation energy (E_A), pre-exponential factor (A_0), and shortest cation-anion distance as a function of Nd content.....	90
A-1	XRD pattern of a polycrystalline NDC film deposited on a platinized silicon substrate using PLD.	97
A-2	XRD pattern of a polycrystalline Pt layer deposited on a c -plane (0001) sapphire substrate using DC sputtering.....	98
A-3	XRD pattern of a highly oriented Pt layer deposited on an a -plane sapphire substrate using DC sputtering.	99
A-4	Omega scan of a highly oriented NDC film with a FWHM = 0.86°.....	100
A-5	The pole figure of an NDC film.	100
B-1	Equivalent circuit fitting window in ZView.	101
B-2	Fit resulting from equivalent circuit analysis performed using ZView.....	102

LIST OF ABBREVIATIONS

AC	Alternating current
AFM	Atomic force microscopy
ALD	Atomic layer deposition
CBED	Convergent beam electron diffraction
CPE	Constant phase element
CTE	Coefficient of thermal expansion
DC	Direct current
EIS	Electrochemical impedance spectroscopy
FCV	Fuel cell vehicle
FWHM	Full width at half max
FIB	Focused ion beam
GDC	Gadolinium doped ceria
HR-XTEM	High-resolution cross-sectional transmission electron microscopy
IT	Intermediate temperature
LOI	Loss on ignition
MBE	Molecular beam epitaxy
NDC	Neodymium doped ceria
PLD	Pulsed laser deposition
PVA	Polyvinyl alcohol
PVD	Physical vapor deposition
R	Resistor
RMS	Root mean square
SAED	Selected area electron diffraction
SCL	Space charge layer

SEM	Scanning electron microscopy
SOFC	Solid oxide fuel cell
TCE	Trichloroethylene
TEM	Transmission electron microscopy
XRD	X-ray diffraction
YSZ	Yttria stabilized zirconia

LIST OF SYMBOLS

σ	Ionic conductivity
σ_{gc}	Grain ionic conductivity
δ	Oxygen vacancy stoichiometry
Θ	Phase angle
a	Lattice parameter
A_0	Pre-exponential coefficient
A	Sample area
C_s	Spherical aberration coefficient
E_A	Activation energy
E_m	Activation energy of migration
$E_{ass.}$	Activation energy of association
k	Boltzmann constant
l	Sample thickness
Ln	Lanthanide
N_O	Number of oxygen sites per unit volume
q_v	Charge of an oxygen vacancy
r_o	Effective oxygen radius
r_c	Average cation radius
r_d	Radius of dopant cation
r_h	Radius of host cation
R	Ideal gas constant
S	Configurational entropy
ΔS_m	Entropy change during oxygen diffusion
T	Temperature

T_m	Melting temperature
ν_0	Jump frequency
$[V_{O''}]$	Concentration of oxygen vacancies
x	Dopant fraction
Z'	Real part of complex impedance
Z''	Imaginary part of complex impedance

Abstract of Thesis Presented to the Graduate School
of the University of Florida in Partial Fulfillment of the
Requirements for the Degree of Master of Science

SIZE AND COMPOSITION EFFECTS ON IONIC CONDUCTIVITY:
DOPED CERIA BULK CERAMICS AND THIN FILM

By

Robert Martin Kasse

May 2013

Chair: Juan C. Nino

Major: Materials Science and Engineering

Highly oriented $\text{Nd}_{0.1}\text{Ce}_{0.9}\text{O}_{2-\delta}$ thin films were deposited on Pt bottom electrodes for the first time and the first across-plane ionic conductivity measurements of these films were performed. Microstructure was investigated using X-ray diffraction, transmission electron microscopy, and atomic force microscopy. Conductivity measurements were performed using two-point AC electrochemical impedance spectroscopy (EIS). Such thin film samples allow for the first time the direct measurement of grain ionic conductivity of doped ceria. Ionic conductivity data indicates inconsistencies in literature may simply be a result of the experimental conditions used in each study.

Samples of $\text{Sm}_x\text{Nd}_y\text{Ce}_{0.9}\text{O}_{2-\delta}$ were prepared using solid state processing and conductivity measurements were done using EIS from 250-700°C. Activation energy was calculated from Arrhenius plots and values increased as composition shifted from pure Sm^{+3} to pure Nd^{+3} in agreement with literature and the effective index concept. The results of this study conclude that $\text{Sm}_x\text{Nd}_y\text{Ce}_{0.9}\text{O}_{2-\delta}$ constitutes a versatile system

impervious to potential performance degradation due to preferential dopant segregation and redistribution.

$\text{Nd}_x\text{Ce}_{1-x}\text{O}_{2-\delta}$ ($0.05 \leq x \leq 0.55$) was prepared using solid state processing and grain ionic conductivity was measured using EIS. X-ray and neutron diffraction indicate the highly defective fluorite stabilizes into a C-type rare earth oxide structure at compositions above $x=0.50$. The conductivity of the compounds follows an Arrhenius behavior showing a maximum conductivity of $0.054(1) \text{ S}\cdot\text{cm}^{-1}$ for $\text{Nd}_{0.15}\text{Ce}_{0.85}\text{O}_{2-\delta}$ at 700°C with an associated activation energy of $0.726(5) \text{ eV}$. Both activation energy and pre-exponential factor increase significantly during the phase transition from 35-40% Nd, resulting in an effective gradual decrease of conductivity across the phase transition.

CHAPTER 1 INTRODUCTION

1.1 Statement of Problem and Motivation

Growing worldwide energy demand along with a push to reduce greenhouse gas production, which contributes to global warming, has scientists looking for new sources of clean and renewable energy. Possible solutions include wind, solar, nuclear, and fuel cell technology though a combination of all of these is likely necessary. Solid oxide fuel cells (SOFCs) have received increased attention in recent years as an environmentally friendly power source, particularly those which operate in the intermediate temperature (IT) range of 400 - 800°C due to their flexibility in design, wider range of useable fuels, and potential uses in distributed and portable power.^{1,2} However, current SOFCs do not provide sufficient power at these intermediate temperatures and must operate at or above 1000°C which is far too high for use in technologies such as fuel cell vehicles (FCVs). Higher operating temperatures also require higher cost fuel cell components. A key component of an efficient IT-SOFC is a solid oxide electrolyte with a high ionic conductivity at intermediate temperatures. Many investigations have focused on rare-earth doped ceria as a potential candidate material for IT applications but there is still much work to be done in understanding the effects of composition and microstructure on the ionic conductivity of these materials.³

1.2 Scientific Approach

In recent years, the majority of investigations concerning SOFC electrolytes have focused on doped ceria systems. The main objective of this thesis is to determine the effects of size and different dopant strategies on the grain ionic conductivity of rare earth doped ceria systems.

A clear understanding of the effects of grain size on the ionic conductivity of doped ceria is currently unavailable. No studies in the current literature have been able to isolate and directly measure either grain core or grain boundary conductivity. Thin film samples free of grain boundaries will be synthesized and the ionic conductivity will be measured as a function of film thickness in order to directly determine the effect of size on grain ionic conductivity.

Uniformly co-doped samples in the $\text{Sm}_2\text{O}_3\text{-Nd}_2\text{O}_3\text{-CeO}_2$ system, with a dopant ratio of 1:1, have been investigated but no studies have reported the effects of changing the dopant ratio at constant total dopant content on grain ionic conductivity. A set of samples in the $\text{Sm}_x\text{Nd}_y\text{Ce}_{0.9}\text{O}_{2-\delta}$ system will be synthesized and their electrical properties measured such that the effect of co-dopant ratio on ionic conductivity can be determined.

An anion disorder-order phase transition as a function of dopant concentration has been observed in the $\text{Nd}_2\text{O}_3\text{-CeO}_2$ system and while a deleterious effect on conductivity is expected, this has not been corroborated experimentally. Samples with Nd dopant concentrations from 0.05-0.55 will be synthesized such that the effect of composition on structure and ionic conductivity can be determined.

Various characterization techniques will be used to complete the stated research goals. Ionic conductivity will be measured using two-point AC electrochemical impedance spectroscopy. Microstructure will be investigated using scanning electron microscopy, transmission electron microscopy, profilometry, and atomic force microscopy. Phase purity will be determined using X-ray diffraction.

1.3 Organization of Thesis

Chapter 2 provides background information necessary for better understanding the work presented in subsequent chapters. Information regarding solid oxide fuel cells, pulsed laser deposition, defect reactions and conduction mechanisms in doped ceria, and electrochemical impedance spectroscopy is provided. Chapter 3 discusses the experimental procedures, including sample preparation and materials characterization techniques, used in the execution of the research.

Chapter 4 discusses work investigating highly oriented thin films of doped ceria deposited on Pt bottom electrodes and presents the structural characterization and across-plane ionic conductivity results.

Chapter 5 reports the effects of co-doping ceria with uneven amounts of Sm and Nd and discusses the compositional flexibility of the $\text{Sm}_x\text{Nd}_y\text{Ce}_{0.9}\text{O}_{2-\delta}$ system. Chapter 6 details how activation energy, pre-exponential factor, and grain ionic conductivity change across the disorder-order phase transition in the $\text{NdO}_{1.5}\text{-CeO}_2$ system.

Chapter 7 summarizes the work detailed in the preceding chapters and outlines ideas for future investigations of both bulk and thin film doped ceria electrolyte materials.

1.4 Contributions to the Field

This work investigates the size and compositional effects on the ionic conductivity of rare earth doped ceria electrolytes. The main contributions of this work to the field of materials science are as summarized below:

1. Highly oriented doped ceria thin films were successfully deposited on Pt bottom electrodes for the first time.

2. The first ever across-plane ionic conductivity measurements of highly oriented doped ceria thin films were performed, which directly measures grain ionic conductivity. Measurements were performed as a function of film thickness such that size effects on the grain ionic conductivity could be determined.
3. The ionic conductivity of $\text{Sm}_x\text{Nd}_y\text{Ce}_{0.9}\text{O}_{2-\delta}$ ($x + y = 0.10$, with $x = 0, 0.0125, 0.025, \dots, 0.1$) was measured for the first time to determine the effect of different codoping ratios on ionic conductivity and it was found that the system is very compositionally flexible with regards to sinterability and ionic conductivity which follows the theory of effective index.
4. The effect of the disorder-order phase transition in the $\text{NdO}_{1.5}\text{-CeO}_2$ system on grain ionic conductivity was investigated for the first time. At room temperature, XRD and neutron diffraction determined that this transition occurs at ~50% Nd while conductivity measurements indicate that the transition occurs at ~40% Nd at higher temperatures. Both the activation energy and pre-exponential factor increase sharply at this transition causing ionic conductivity to decrease gradually.

CHAPTER 2 BACKGROUND

2.1 Solid Oxide Fuel Cells

Fuel cells have received renewed attention in recent decades due to their ability to provide a clean source of energy and operate with a high efficiency. There are many different types of fuel cells, with different electrolyte materials, different charge carrying mechanisms, and different operating temperatures. A schematic of a solid oxide fuel cell (SOFC) can be seen in Figure 2-1, with anode and cathode reactions shown in Equations 2-1 and 2-2.

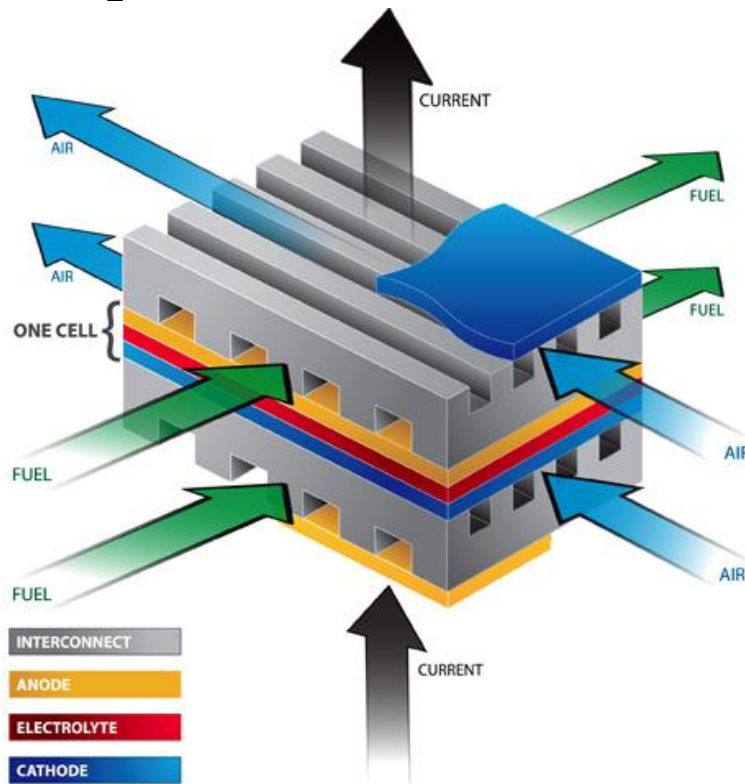
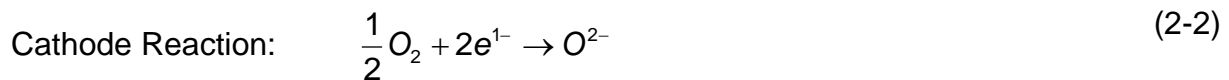


Figure 2-1. Schematic depiction of the operation of a solid oxide fuel cell.⁴

SOFCs directly convert chemical energy generated by the reduction of a gaseous fuel such as H_2 to electricity. Hydrogen gas, or whatever the source of hydrogen in the fuel may be (e.g. CH_4) is broken into protons and electrons at the anode. Since the solid oxide electrolyte is an electronic insulator, the electrons cannot pass through it, and are forced through an external circuit, generating a useful current. The electrons react with oxygen upon reaching the cathode to form oxygen ions which then travel through the electrolyte and recombine with protons at the anode to produce water in the form of steam, completing the circuit. Current state of the art SOFCs are generally used at temperatures around $1000^\circ C$ to increase fuel conversion efficiency. A commercial electrolyte-supported large-area YSZ-based FlexCell produced by Nextech is shown in Figure 2-2 below.

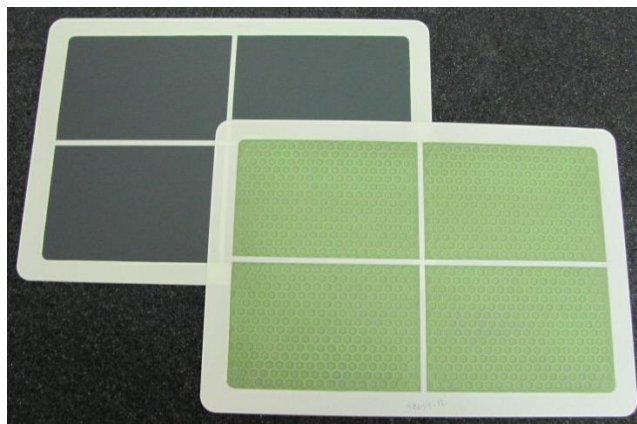


Figure 2-2. Large-area electrolyte supported YSZ-based FlexCells by Nextech. FlexCells with electrolytes less than $40\ \mu m$ thick can be manufactured with areas up to $470\ cm^2$.

SOFCs in current applications typically have yttria stabilized zirconia (YSZ) electrolytes. Other materials currently investigated for use as electrolytes include other fluorite-based oxides such as doped Bi_2O_3 and CeO_2 , perovskites such as lanthanum gallate, and $La_2Mo_2O_9$. Based on the conductivity of YSZ and the typical thickness (\sim

10 μm) of these electrolytes when employed in SOFCs, the minimum operating temperature is around 700°C .⁶ Electrodes, both anodes and cathodes, must be chemically and thermally compatible with the electrolyte they are used with and must be stable at the operating temperature.⁶ These electrodes are porous composites of a metal or electronically conducting oxide and an electrolyte material, with a large proportion of triple phase boundaries between metal, electrolyte, and gas to improve fuel conversion. Porous Pt used to be commonly used in electrodes but because of its very high cost, they are now typically made with a Ni/ZrO₂ cermet (anodes) and doped LaMnO₃ (cathodes).⁷ Good thermal expansion coefficient (CTE) matching is also important as cells will be thermally cycled between room and operating temperature, which could build up thermal stresses if the CTE mismatch is too large. Interconnects are metal or ceramic plates which separate individual cells in a fuel cell stack and connect them together in series to add together the power generated by each individual cell. High temperature SOFCs use interconnects made of doped LaCrO₃ or expensive high temperature metal alloys, though vaporization of Cr at high temperatures is an issue that has taken attention away from metal alloy interconnects. Interconnects also need to have a good thermal expansion match with other cell components for the reasons stated above.⁸

Unlike heat engines which operate more efficiently as temperature is increased, the oxidation and reduction reactions in SOFCs actually increase in efficiency when the temperature is lowered.⁷ A Ragone plot comparing various energy devices is shown in Figure 2-3. Lowering the operating temperature to the intermediate (IT) temperature range ($400\text{-}800^\circ\text{C}$) also opens up many more options for fuel cell stack materials

selection, which is restricted at higher temperatures. Lowering operating temperatures has the potential to lower production costs in multiple ways, including the fact that at lower temperatures interconnects can be made out of less expensive stainless steel as opposed to the ceramic interconnects used in high temperature SOFCs because stainless steel has a good CTE match with other cell components. A lower power density is generated at lower temperatures, but the lifetime of the fuel cell is extended and the overall cost of the fuel cell is reduced. One of the major necessary steps towards the expansion of SOFCs into automotive applications is to increase the power density at lower temperatures to the levels achieved with current high temperature SOFCs. One of the foci of research in this area is on developing electrolytes with higher ionic conductivities in the IT range.

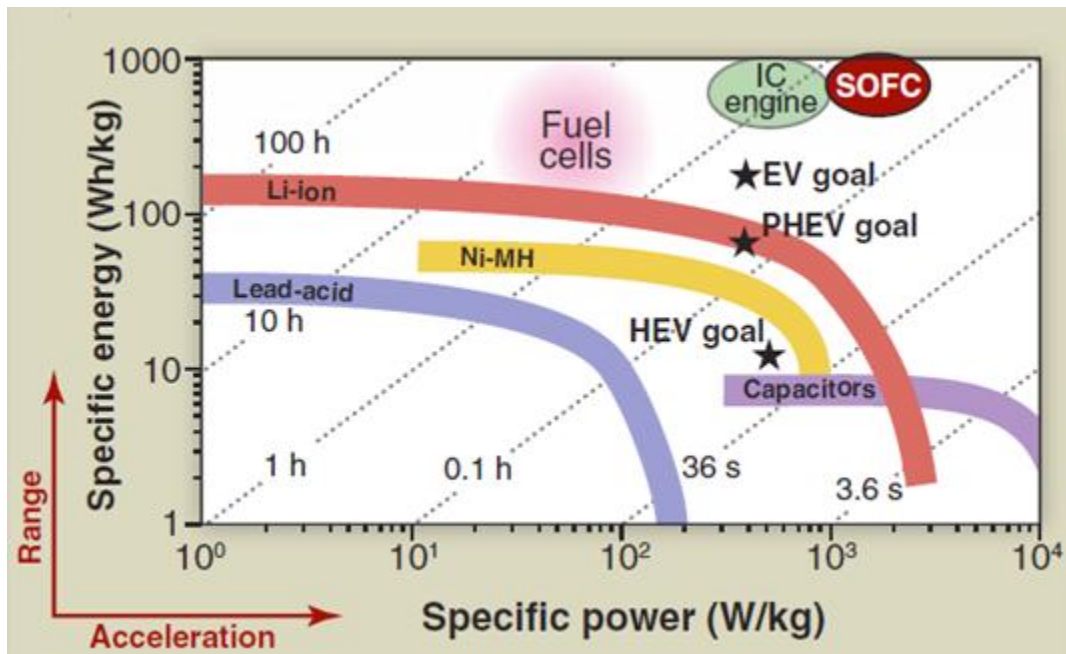


Figure 2-3. Ragone plot comparing the specific power and specific energy of various devices to SOFCs.²

While a high ionic conductivity is vitally important for SOFC electrolytes, high thermal and chemical stability at both room and operating temperatures, the ability to be

thermally cycled without performance degradation, and a good thermal expansion match with other cell components are also necessary. Cubic fluorite structured oxides are receiving a lot of attention as a potential candidate material for IT-SOFC electrolyte application because of their performance in these areas. Figure 2-42-4 shows an Arrhenius plot of the conductivity of various fluorite-structured oxides as a function of temperature. The slope of the line on this graph is related to the activation energy for ionic conduction, and the y-intercept is related to the pre-exponential coefficient.

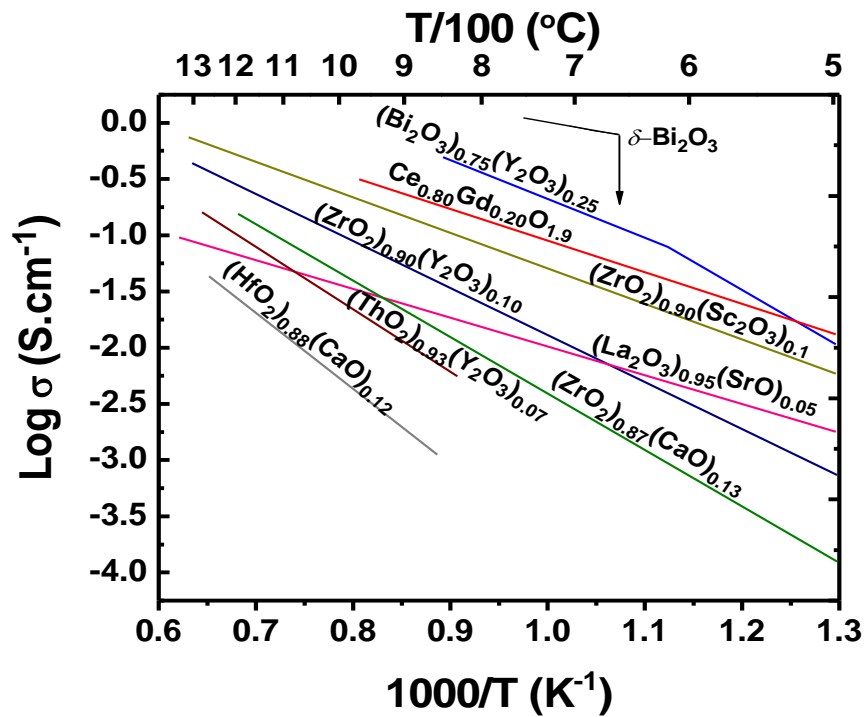


Figure 2-4. The log of ionic conductivity versus temperature for various fluorite structured oxides.⁹

As seen in Figure 2-42-4, $\delta\text{-Bi}_2\text{O}_3$ has the highest ionic conductivity at intermediate temperatures, however is not stable, as it undergoes a phase transformation to $\alpha\text{-Bi}_2\text{O}_3$ between room and operating temperatures which is not ionically conducting. Doped Bi_2O_3 is stable over a wider temperature range but still poses issues such as poor mechanical strength, volatilization of Bi_2O_3 , and high

corrosive activity.¹⁰ The material with the next highest ionic conductivity, and one that is the focus of many investigations^{9,11-25}, is rare-earth-doped CeO₂. Doped ceria is a good IT-SOFC electrolyte candidate material because of its high ionic conductivity, low electronic conductivity, good stability, and good thermal expansion coefficient match with stainless steel, which can be used as an inexpensive interconnect material as noted above.

A large portion of the research being performed on the ionic conductivity of SOFC electrolytes is done by measuring polycrystalline bulk ceramic pellets. However, the overall performance of these same materials in thin film form is increased because as electrolyte thickness is decreased, so are the ohmic losses associated with ionic conduction since most ohmic resistance comes from the slow rate of ion migration in the electrolyte relative to electron conduction.²⁶ However, the film still must be thick enough to prevent fuel cross over thus an ideal electrolyte should be around 10-20 μ m thick depending on the material, morphology, and how it is deposited.²⁷

To better understand the effect of electrolyte thickness on SOFC performance, many investigations have focused on thin film SOFCs.²⁸ From a practical standpoint it is difficult to deposit films of less than 1 μ m without cracks or pinholes that would allow gas crossover. Ding *et al.* investigated SOFCs with varying electrolyte thicknesses, seen in Figure 2-5 below, and found that for GDC deposited using dry co-pressing and spray dry co-pressing an electrolyte thickness of 5 μ m produced the greatest electrical performance.²⁸ Thin films can also be used as ultrathin protective layers between electrodes and electrolytes to help prevent the formation of undesired phases which

degrade cell performance, such as a layer of GDC between a YSZ electrolyte and a lanthanum–strontium–magnate cathode.²⁷

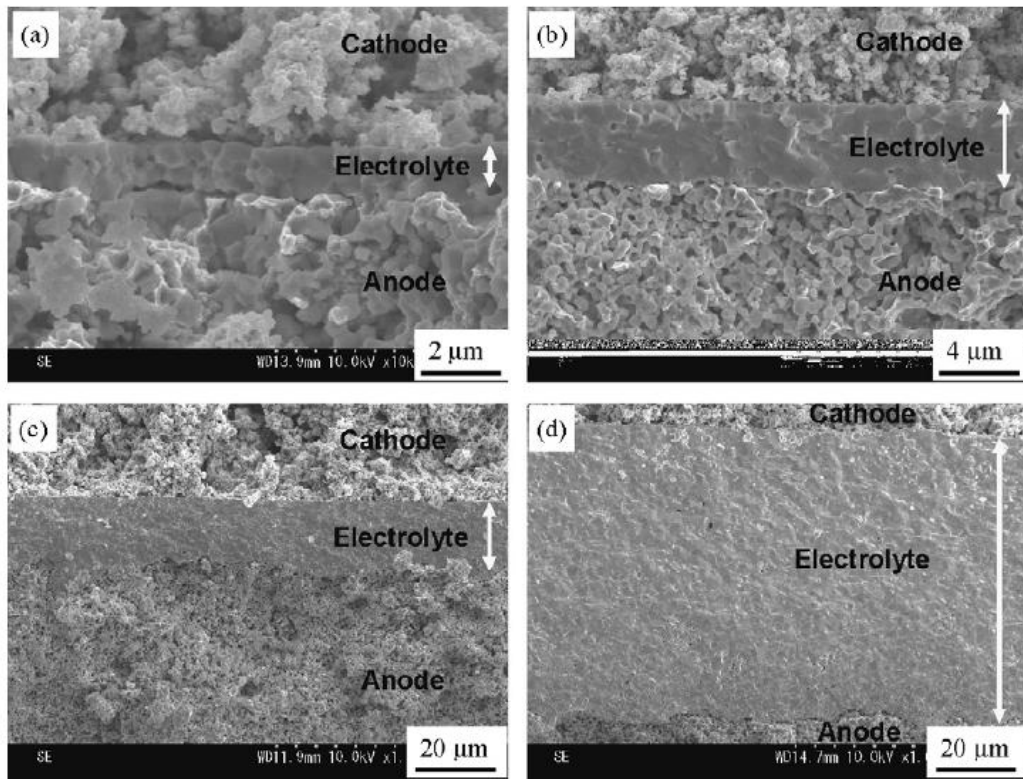


Figure 2-5. Cross-sectional SEM micrographs of the anode-supported single cells with GDC electrolyte films of (a) 1 μm, (b) 4 μm, (c) 16 μm and (d) 75 μm.²⁸

Smaller SOFC stacks that could be used to power individual buildings in remote locations or in military operations require stacks that operate at intermediate temperatures. IT-SOFCs could also possibly be used in portable power generators with similar power generating capabilities as those based on heat engines used today. Though fuel cell vehicles (FCVs) are not thought to be the most promising clean energy technology in the area of personal vehicles and other transportation over the long run, their ability to use any hydrocarbon as fuel, which have a much greater energy density than H₂²⁹, makes them an attractive transition technology.^{2,30} For this to happen, fuel cells will necessarily need to operate at lower temperatures and be smaller and more

compact. Using pure hydrogen gas as fuel may be more environmentally friendly considering the only waste product would be water, but SOFCs using hydrocarbon fuels would allow commercialization to happen much sooner.

High temperature SOFCs, when coupled with other fuel cell types or gas turbines can attain even higher efficiencies for large scale energy production.¹ For movement into the area of smaller stacks and portable power, better cell materials need to be developed for operation in the intermediate temperature range. Progress has been made in developing better electrolytes, more efficient electrodes, and less expensive interconnects but further improvements are needed before widespread commercialization is viable. The future of this technology is promising and one day SOFCs may be a part of a larger clean energy infrastructure.

2.2 Structure of Relevant Materials

As noted in section 2.1, a key component of an IT-SOFC is an electrolyte with a high ionic conductivity in the IT range. Being familiar with the structure of ceria is necessary for a complete understanding of the approaches taken to enhance ionic conductivity. This section presents information on the structure of ceria and other materials relevant to the work in this thesis.

2.2.1 Ceria

Undoped ceria has a fluorite structure, space group $Fm\bar{3}m$ and lattice parameter $a = 5.4114 \text{ \AA}$.³¹ The lowest energy surface in ceria is the (111). In doped ceria, ionic conductivity is the result of an oxygen vacancy diffusion mechanism. Doping introduces oxygen vacancies into the lattice as shown in Equation 2-3 and Figure 2-6 below.



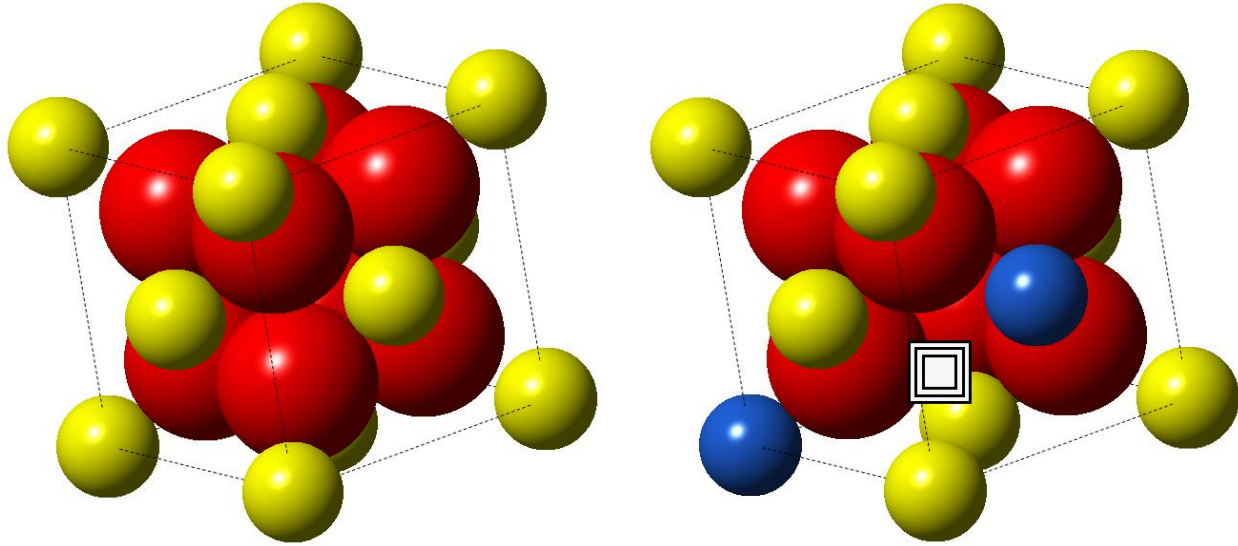


Figure 2-6. The schematics show the crystal structure of doped and undoped ceria. Pure ceria (left) has a fluorite crystal structure with space group $Fm\bar{3}m$. When doped with rare earth elements the dopant cation Ln^{3+} substitutes for Ce^{4+} and in order to maintain charge neutrality, oxygen vacancies are formed (right). In the figure, yellow spheres represent Ce^{4+} ions, red spheres represent oxygen ions, blue spheres represent Ln^{3+} cations, and the white square represents an oxygen vacancy.

When heavily doped with Ln^{3+} cations a phase transition occurs, as discussed in Chapter 6. The oxygen deficient fluorite structure becomes a C-type rare earth structure, space group $Ia\bar{3}$, seen in Figure 2-7 below. The general chemical formula for materials with this structure is typically A_2O_3 . It can be imagined as a fluorite cell with two oxygen vacancies along the body diagonal. Eight of these defect fluorite cells compose a C-type unit cell, thus associated with the phase transition is a doubling of the lattice parameter. For example, the lattice parameter of $Nd_{0.55}Ce_{0.45}O_{2-\delta}$ is $a = 10.998 \text{ \AA}$. The X-ray pattern of the C-type structure is only slightly different from that of the fluorite in that it features extra super-lattice peaks, which are very weak.

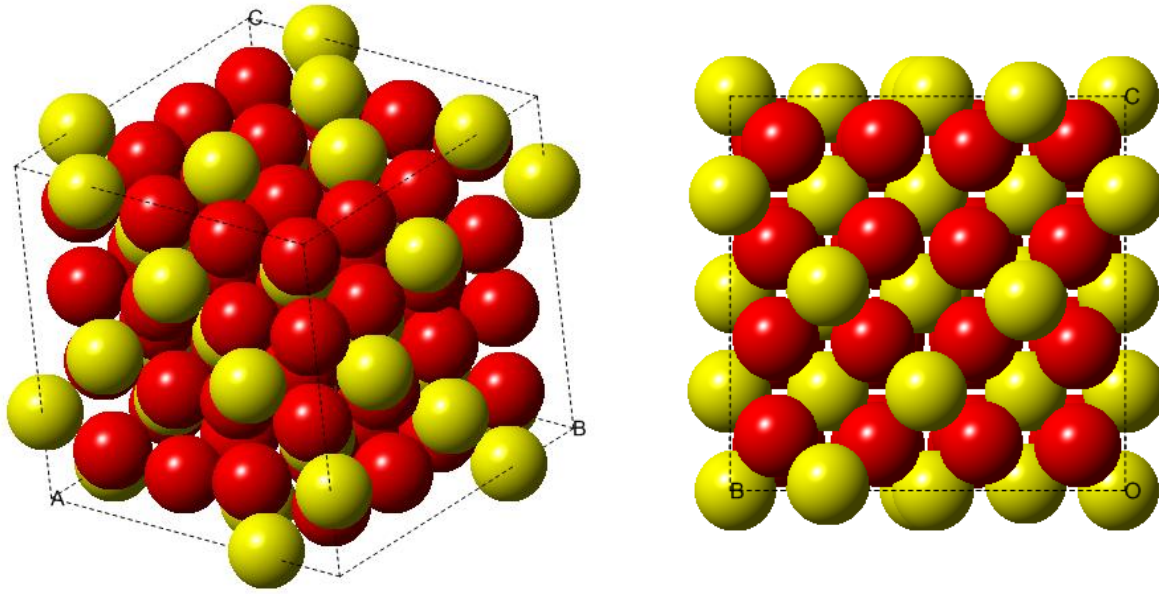


Figure 2-7. The C-type rare earth structure, space group $Ia\bar{3}$. The image on the right shows a view along the [001] direction. Yellow spheres can be Ce^{4+} or Ln^{3+} ions and the red spheres represent oxygen ion sites.

Before oxygen vacancy diffusion can occur a minimum activation energy, E_a , must be provided which is composed of both association ($E_{ass.}$) and migration (E_m) enthalpy such that $E_a = E_m + E_{ass.}$ $E_{ass.}$ is the energy need to overcome the association of defect clusters, which form when positively charged oxygen vacancies and negatively charged dopant cations are attracted to one another. E_m is the enthalpy related to the motion of oxygen ions in the material. Equation 2-4 shows the Arrhenius behavior of the ionic conductivity and that the conductivity is not only dependant on activation energy but also a pre-exponential term, A_0 . This term is expanded in Equation 2-5 where q_v is the charge of an oxygen vacancy, k is the Boltzmann constant, $[V_O^{\bullet\bullet}]$ is the fraction of free oxygen vacancies, N_O is the number of oxygen sites per unit volume, a is the ion jump distance, ν_0 is the jumping frequency, and ΔS_m is the entropy change during oxygen diffusion. To a first approximation, all of these terms, except $[V_O^{\bullet\bullet}]$, are

either constant or independent of total dopant concentration (within the dilute regime) so maximizing the number of mobile oxygen vacancies by using better doping schemes is the ideal way to increase the pre-exponential.

$$\sigma T = A_0 \exp\left(\frac{-\Delta H_a}{kT}\right) \quad (2-4)$$

$$A_0 = \frac{q_v^2}{k} [V_O^{\bullet\bullet}] N_0 a^2 v_0 \exp\left(\frac{\Delta S_m}{k}\right) \quad (2-5)$$

It is well understood that in microcrystalline doped ceria space charge regions near grain boundaries (depicted schematically in Figure 2-8) block the conduction of oxygen ions and reduce total ionic conductivity.³² Grain boundaries have positively charged cores due to an excess number of oxygen vacancies. To maintain charge neutrality, negatively charged dopant cations segregate to the grain boundaries creating the space charge layer as seen in Figure 2-9.¹⁴

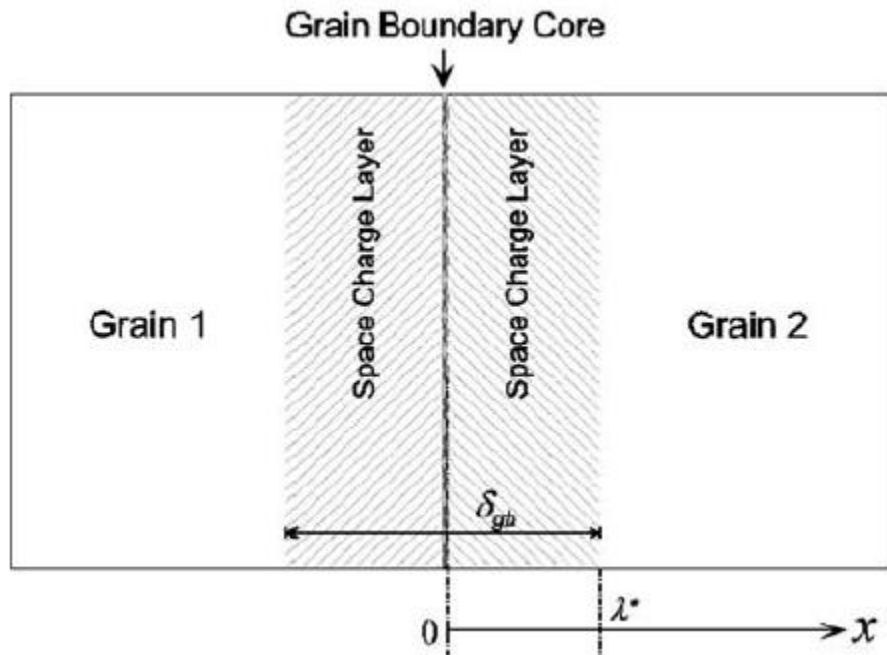


Figure 2-8. Schematic depiction of the space charge region near grain boundaries in doped ceria.³²

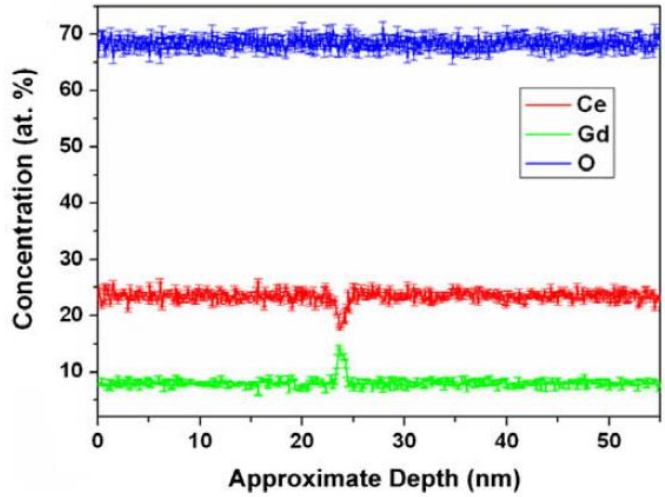


Figure 2-9. Concentration profile obtained via atom probe analysis of various species near a grain boundary in GDC.¹⁴

2.2.2 Sapphire

Sapphire, single crystal Al_2O_3 , has a hexagonal unit cell and is of the space group $R\bar{3}c$ and has lattice parameters $a = 4.735 \text{ \AA}$ and $c = 12.899 \text{ \AA}$.³³ Various views of the crystal structure can be seen in Figure 2-10 below.

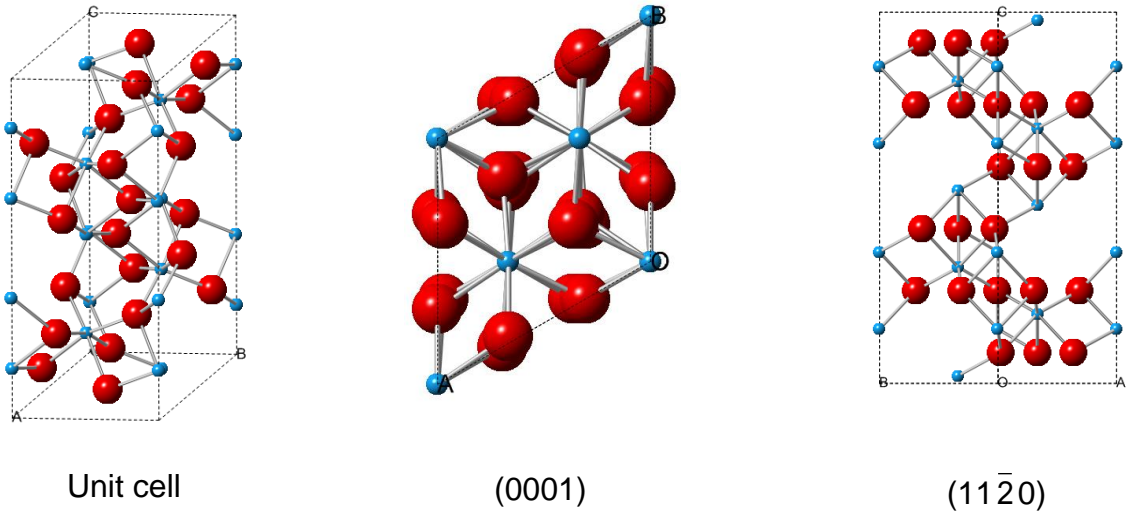


Figure 2-10. Various views of the sapphire crystal structure. The center image shows the (0001) plane, also referred to as the c-plane while the image on the right shows the $(11\bar{2}0)$ plane, also referred to as the a-plane.

2.2.3 Platinum

Platinum has an FCC crystal structure, space group $Fm\bar{3}m$ and lattice parameter $a = 3.9231 \text{ \AA}$.³⁴ Various views of the crystal structure can be seen in Figure 2-11 below including a view of the lowest energy surface in Pt which is the (111).

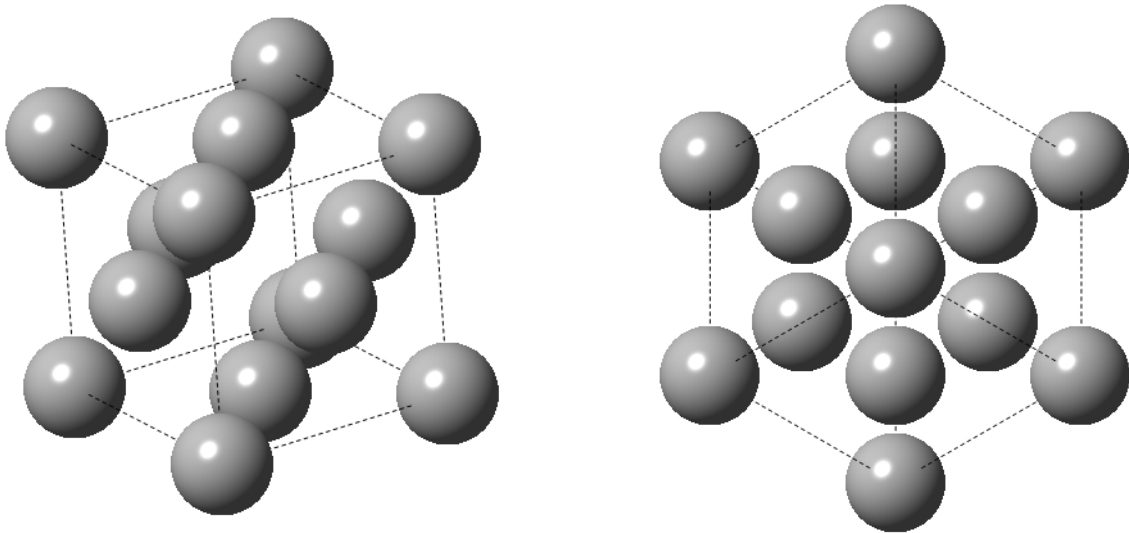


Figure 2-11. Various views of the FCC crystal structure of platinum. The image on the right is a view along the [111] direction.

2.3 Electrochemical Impedance Spectroscopy

The most important property of SOFC electrolytes is the ionic conductivity. One method commonly used to measure the ionic conductivity of oxide ceramics is two-point alternating current (AC) electrochemical impedance spectroscopy (EIS). EIS is ideal for these types of measurements due to its ability to distinguish between grain, grain boundary, and electrode impedance. In a typical experiment a voltage is applied to an electroded sample and the corresponding current is measured (or vice versa) as a function of frequency, usually in the range of 10^{-1} - 10^7 Hz.³⁵ The magnitude of the impedance is calculated using Ohm's law and is output along with phase angle (Θ), the difference in phase between the current and voltage, which is zero for a pure resistor, -

90° for a pure capacitor, and +90° for a pure inductor.³⁶ The real (Z') and imaginary (Z'') parts of the complex impedance are related to the phase angle as shown in Figure 2-12 below and can be calculated using Equations 2-6 and 2-7.

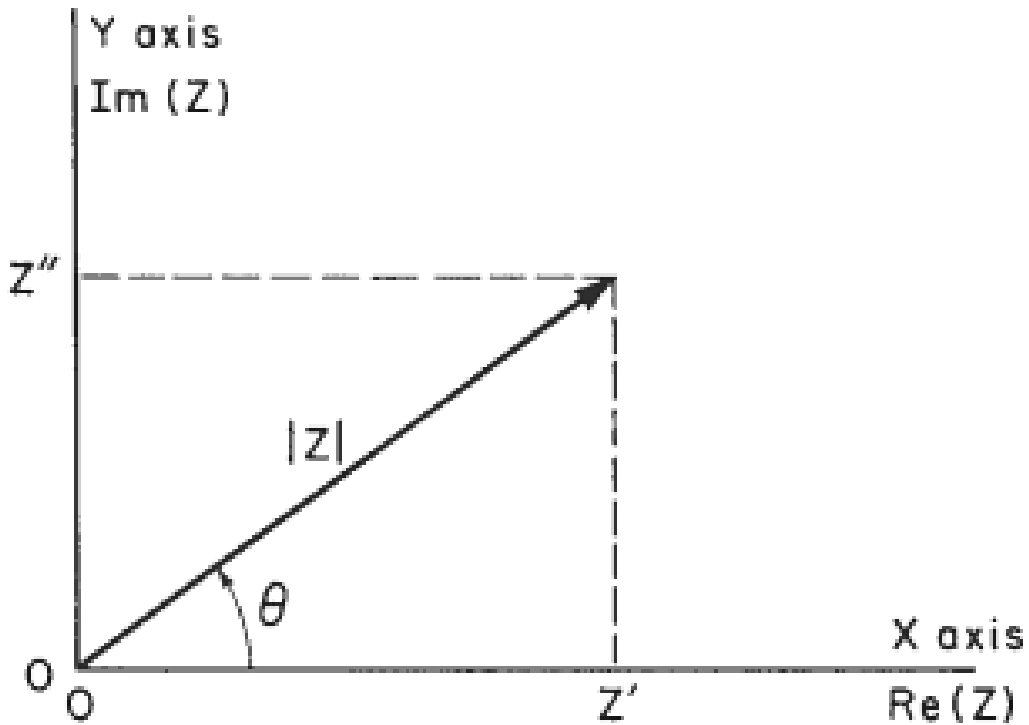


Figure 2-12. Plot showing the relationship between impedance and phase angle.³⁵

$$Z = |Z| \cos \theta \tag{2-6}$$

$$Z' = |Z| \sin \theta \tag{2-7}$$

When the real and the negative of the imaginary parts of the complex impedance are plotted against one another, the result is called a Nyquist plot, seen in Figure 2-13 below. For polycrystalline samples, three distinct semicircular arcs are present representing the grain, grain boundary, and electrode impedance, respectively. The frequency at the top of each arc corresponds to the characteristic frequency, which is related to the time constant for that conduction process.

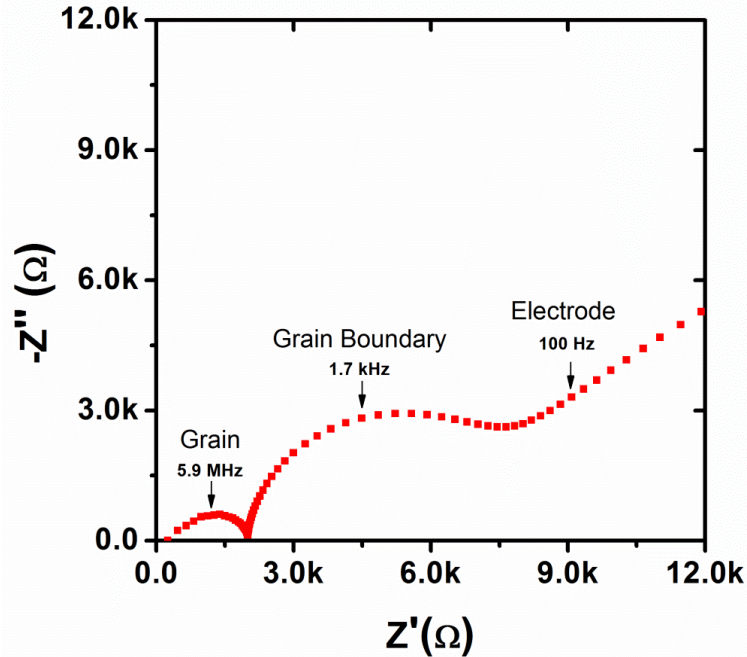


Figure 2-13. Generic Nyquist plot showing the grain core, grain boundary, and electrode impedance arcs for a polycrystalline sample.

An equivalent circuit analysis can be used to extract impedance from a Nyquist plot. One such circuit can be seen in Figure 2-14 where an inductor is used to model the experimental setup and a parallel resistor-constant phase element (CPE) element is used to model the grain, grain boundary, and electrode. A CPE is equivalent to a distribution of capacitors in parallel with a phase angle somewhat less than 90° .



Figure 2-14. Equivalent circuit used to fit a Nyquist plot of complex impedance. L1 is an inductor modeling the experimental setup while the R-CPE elements model grain core, grain boundary, and electrode impedance.

In this thesis, the primary focus is on the grain core ionic conductivity which corresponds to the first arc of the impedance spectrum. The resistance value obtained from the equivalent circuit fit can simply be plugged in to Equation 2-6 below, along with

the sample dimensions, to calculate the grain ionic conductivity. R_{GC} is the grain core resistivity, l is the sample thickness, and A is the sample area. A similar calculation can be done to calculate the grain boundary and total conductivity.

$$\sigma_{GC} = \frac{1}{R_{GC}} \times \frac{l}{A} \quad (2-6)$$

When grain size decreases into the nano-range the grain core and grain boundary arcs can begin to become indistinguishable and very difficult to fit accurately. Thus, techniques different from those discussed above must be used to determine the independent contributions. Due to connectivity or shape problems (i.e. grains are not cubes), brick layer models tend to fail when grain size and grain boundary width become comparable.³⁶ Newer models such as the nano-grain composite model can be used to extract grain core and grain boundary impedance and dielectric constants. Another solution to this problem is to work with thin film samples which allow the measurement of fundamental defect and interfacial properties that are not possible in bulk samples.³⁷

2.4 Thin Film Deposition

Two different thin film deposition techniques were employed in this work: pulsed laser deposition (PLD) and DC sputtering. This section will describe these processes.

2.4.1 Pulsed Laser Deposition

Micro-SOFCs employ thin film electrode and electrolyte layers, as discussed in section 2.1 above. Synthesis of materials in the form thin films has been the topic of research for many years.³⁸ Films on the order of only tens or hundreds of nanometers in thickness allow for the measurement of very small scale and fundamental materials properties which cannot be investigated using bulk samples.³⁹

There are numerous thin film deposition techniques including dip coating, spin coating, DC sputtering, atomic layer deposition (ALD), molecular beam epitaxy (MBE), and pulsed laser deposition (PLD). One of the main disadvantages associated with many of these techniques is that it is difficult to deposit films of materials with complex crystal structures, such as superconducting oxides and multilayer materials, while maintaining a reasonably high deposition rate. Materials with many different cations require many different precursors, precise control of the relative amounts of precursors, and if the material is an oxide, control of the oxidizing environment for these other processes. PLD is a relatively simple solution to many of these problems along with having other beneficial characteristics.^{39,40}

Pulsed laser deposition was first demonstrated to be a useful technique for thin film deposition in 1965.⁴¹ However, this process did not really take off until the 1980s after it had been proven to be a reliable, relatively inexpensive way of producing high quality films with the same stoichiometry as the target material.^{42,43} PLD is particularly popular in depositing a wide range of superconducting oxide materials, other electroceramics, and polymers.^{39,44,45}

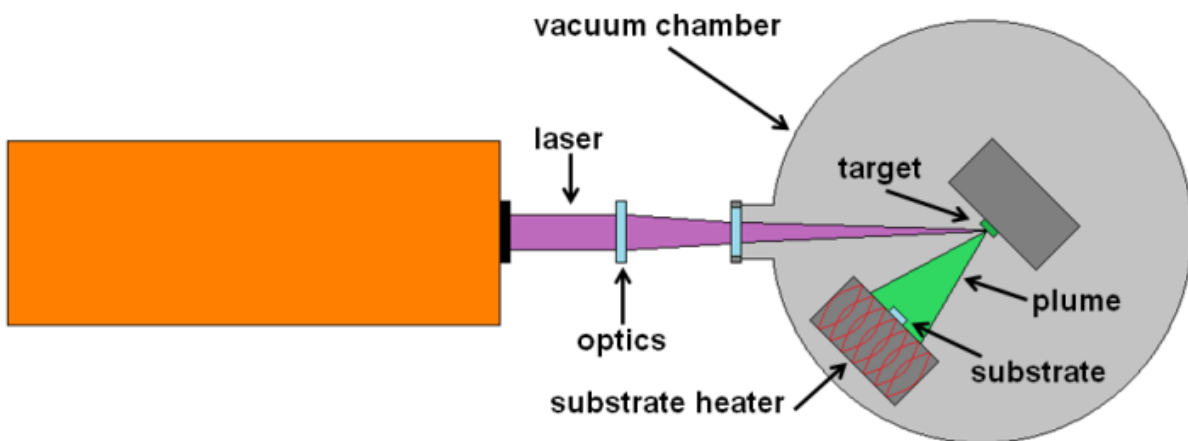


Figure 2-15. Schematic view of the PLD process.

Conceptually the PLD process is quite easy to understand.⁴³ A bulk target of the desired film material is ablated with a pulsed laser in a high vacuum environment creating a plasma plume of the target material. The plasma deposits on a substrate that is typically heated. A schematic of the PLD process is seen in Figure 2-15 above.

The laser is pulsed rather than continuous to increase energy efficiency such that energy is not lost thermally or otherwise.⁴³ Currently, nanosecond pulses are the most widely used though they are inefficient compared to femtosecond pulse lengths which are garnering a lot of attention.⁴⁰ For the deposition of insulating materials, lasers with wavelengths in the 200-400 nm range are most common because photons of this energy are strongly absorbed by insulators.⁴⁶ Two of the most common laser types are KrF and XeCl.⁴⁷

When the laser hits the target, absorption of photons causes the target to both melt and ablate; surface temperatures can reach as high as 3200 K.⁴⁸ Ions, atoms, molecules, and other neutral particles are ejected from the target creating a plume.⁴⁸ If the laser passes through the plume it can further ionize particles. The plume then expands adiabatically as thermal energy is converted to kinetic energy.⁴⁸ There may be a noise associated with the plume expansion as some particles could be travelling faster than the speed of sound.⁴³ To avoid uneven wear of the target and the formation of grooves or pits, the target is usually rotated and the laser moved back and forth across the target surface.^{44,49} This also helps to avoid the formation of droplets of the material being transferred to the substrate. How a target will respond depends on the characteristics of the target as well as the laser. This response is dominated by

electronic properties of the target for pulses of less than a picosecond but is dominated by thermal factors when the pulses are on the order of nanoseconds.⁴²

The plume, that can initially be as hot as 10,000 K, may be a bright white color due to free-free transitions within the plasma, as seen in Figure 2-16 below.^{42,47} It is interesting to note that the direction of the plume is always normal to the surface of the target regardless of the incident angle of the laser and is unaffected by the laser if it were to pass through the plume.⁴³ That being said, unless an advanced system is used to raster the plume across the substrate surface the thickness distribution of the deposited films is rather non-uniform thus PLD is generally only used to deposit over small areas.⁵⁰ The plume is also affected by any background gas, such as oxygen, that is introduced into the vacuum chamber. Gas may be used to be incorporated into the film, slow the velocity of the particles in the plume, confine the size of the plume, or decrease the energy of the particles to limit sputtering away of the growing film.⁴⁷ Controlling the average energy of a particle as it strikes a substrate is critical for producing films of certain a stoichiometry and microstructure.

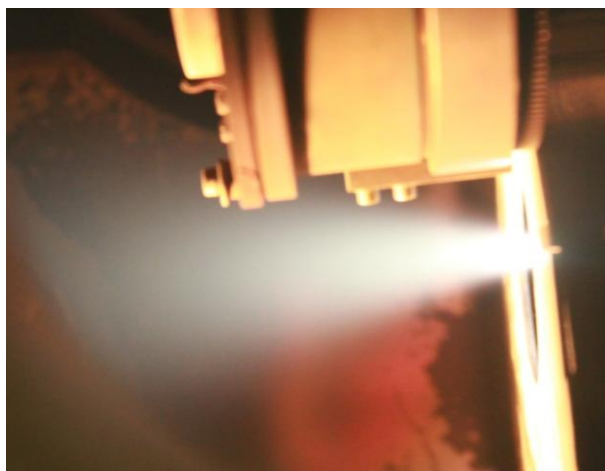


Figure 2-16. Bright white plume generated by the ablation of an $\text{Nd}_{0.1}\text{Ce}_{0.9}\text{O}_{2-\delta}$ target by a 248 nm wavelength KrF laser.

Films deposited using PLD generally have the same structure and composition as the target provided there is no preferential ablation, segregated phases on the target surface, or evaporation of only some of the target components.⁵¹ Other conditions that could cause films to not be stoichiometric include plume species having different sticking coefficients or resputtering of the already deposited film.⁵²

There are three basic ways in which a film can form, as shown schematically in Figure 2-17: island growth (Volmer-Weber), layer growth (Frank van der Merwe), or a combination of the two known as Stranski-Krastanov.⁵³ Which method of formation occurs is determined by the how particle-particle interactions compare to particle-substrate interactions. Island growth occurs when particle-particle bonds are preferred while layer growth is the result of particle-substrate interactions being favorable. Stranski-Krastanov is not well understood but occurs when metals are deposited on metal substrates.⁵³

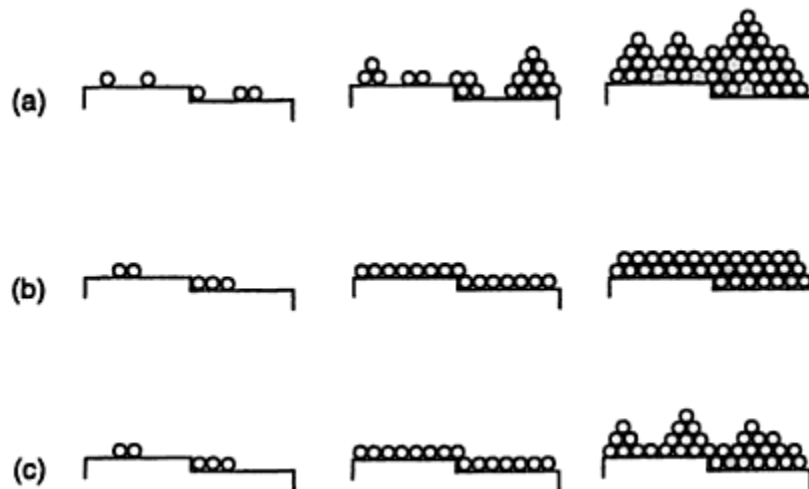


Figure 2-17. Schematic view of various growth modes: a) island growth (Volmer-Weber); b) layer growth (Frank van der Merwe); and c) Stranski-Krastanov.⁵⁴

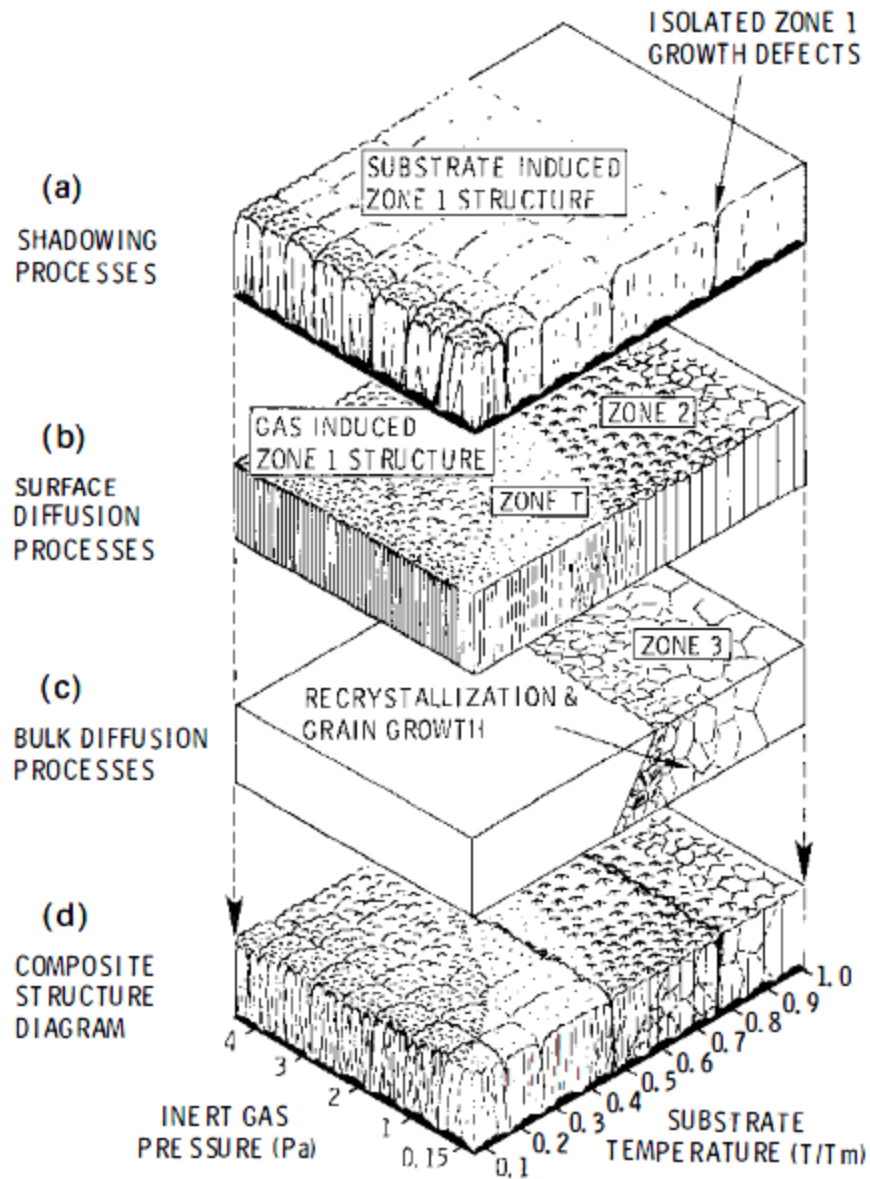


Figure 2-18. Schematic showing the relationship between substrate temperature, gas pressure, and film morphology.⁵⁵

Films deposited at room temperature are generally amorphous with the crystallinity of the films increasing with increasing substrate temperature.⁴² Structure zone models relate film microstructure to deposition conditions, such as the one developed by Thornton *et al.* which relates film morphology to gas pressure and the ratio of substrate temperature to film melting temperature.⁵⁵ A schematic of this model

can be seen in Figure 2-18 above. Morphologies like those shown in Zone 1 result from a lack of surface diffusion causing atoms to stick where they first hit the substrate yielding columnar structures. Zone T is characterized as having a fibrous structure similar to what is found within an individual column of Zone 1 morphology. Both Zone 1 and Zone T structures are considerably affected by gas pressure.⁵⁵ Zone 2 structures occur above about $0.3T_m$, where T_m is the melting point, and can form faceted needles or platelets. These structures are not affected by gas pressure and are the result of adatom diffusion. Zone 3 structures are due to bulk diffusion, such as recrystallization and grain growth, and occur at around $0.5T_m$. Grains may be columnar or equiaxed and this growth is not affected by gas pressure.⁵⁵

2.4.2 DC Sputtering

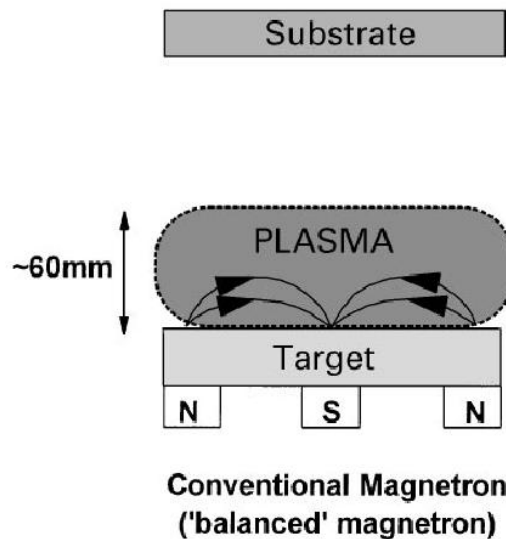


Figure 2-19. Schematic representation of the DC sputtering process.⁵⁶

During the DC sputtering process, a target (cathode) is bombarded with ions causing the formation of a glowing plasma which is deposited on a substrate (anode). Secondary electrons are also produced by the collision and they interact with the ejected particles causing further ionization. A magnetic field is used to trap secondary

electrons near the target surface increasing the probability of particle ionization events.⁵⁶ The increased ionization efficiency produces a dense plasma which leads to higher deposition rates than would be possible without the use of a magnetic field and allows for lower operating pressures and voltages.⁵⁶ Figure 2-19 schematically shows the DC sputtering process.

CHAPTER 3 EXPERIMENTAL PROCEDURES

This chapter will cover the synthesis of both thin film and bulk ceria samples, discussing starting materials, processing steps, and heat treatments, as well as the characterization techniques used to investigate sample properties.

3.1 Preparation of Thin Film Samples

Highly oriented doped ceria thin film samples on Pt bottom electrodes were synthesized using two different deposition techniques: DC sputtering and pulsed laser deposition (PLD). This section will outline the synthesis process in detail.

3.1.1 Substrate Cleaning

Single crystal *a*-plane sapphire (section 2.2.2) substrates purchased from MTI Corporation were cleaned using ultrasonication in trichloroethylene (TCE), acetone, and methanol for five minutes each, and dried using a nitrogen gun. Substrates measuring 1cm x 1cm or 5 mm x 5 mm were used.

3.1.2 Deposition of Highly Oriented Pt Layer Using DC Sputtering

DC sputtering (section 2.4.2) was used to deposit a 50 nm thick Pt layer on a clean sapphire substrate following Nefedov *et al.*⁵⁷ First the substrate was loaded into the deposition chamber ($\sim 10^{-8}$ Torr) and annealed at 500°C for ten minutes. The temperature was then dropped to 300°C for the Pt deposition step which was done under an atmosphere of 5 mTorr Ar. Pt was deposited for 90 seconds but growth rate depends on the gun and target used and must be calibrated. Heating and cooling rates were 10°C/min.

3.1.3 Deposition of Highly Oriented Nd_{0.1}Ce_{0.9}O_{2-δ} Layer Using Pulsed Laser Deposition

The platinized substrates were again clean as described above before being adhered to a substrate holder using Ag paste. PLD (section 2.4.1) was used to deposit the Nd_{0.1}Ce_{0.9}O_{2-δ} layer at 720°C following Gobel *et al.*³⁷, under an atmosphere of 10 mTorr O₂, laser energy of 320 mJ, and a repetition rate of 5 Hz. A KrF laser with a wavelength of 248 nm and a pulse width of 30 ns was used. One edge of the platinized substrate was masked using a second substrate to ensure a strip of the Pt bottom electrode remained exposed such that it could be used as bottom contact for electrical measurements. Oxygen was left in the chamber until the substrate had cooled back down to room temperature. The target used during PLD was synthesized using solid state processing as detailed in section 3.2 Preparation of Bulk Samples, below.

3.1.4 Deposition of Pt Top Electrodes Using DC Sputtering

Pt top electrodes 50 nm thick were deposited using DC sputtering with a shadow mask at room temperature. The shadow masks were purchased from Benchmark Technologies and feature 200 μm diameter holes in a hexagonal lattice pattern with the centers of the holes 500 μm apart. Samples were affixed to the holder using double sided Kapton® tape. To attach the mask, two substrates the same thickness as the sample were affixed to the holder on either side of the sample. The mask was then taped to these substrates to ensure it would lay flat and not bend.

3.2 Preparation of Bulk Samples

Bulk samples were synthesized using conventional solid state processing. This section will explain the processes used in detail.

3.2.1 Powder Synthesis

Starting materials for bulk samples were stoichiometric amounts of oxide powders with 99.99% purity (Alfa Aesar). Stoichiometric amounts were determined by taking loss on ignition (LOI) data into account. Purchased powders were weighed before and after heating to 800°C for 1 h, allowing water and other surface impurities to volatilize, to better determine the percentage of effective powder. Starting powders were wet ball milled in water for 24 h, using ammonium polyacrylate (DARVAN® 821-A) as a dispersant, dried in an oven at 120°C for 16 h, then ground and sieved using a 212 µm mesh before calcining at 1450°C for 10 h. Calcined powders were again wet ball milled for 24 h, dried at 120°C for 16 h, and ground and sieved using a mesh with a 212 µm aperture opening.

3.2.2 Formation of Ceramic Green Body

Up to 2 wt% binder (polyvinyl alcohol in deionized water) was added to the calcined powder which was then uniaxially pressed at 180 MPa using dies with diameters of 7, 9, and 13 mm. The pellets were then placed into balloons, which were evacuated using a roughing vacuum pump, and isostatically pressed at 250 MPa for 3 min.

3.2.3 Pellet Sintering

Pellets were sintered at 1600°C for 10 h in air. Sacrificial powder of the same composition was placed between the pellet and the zirconia setter to prevent any reaction. Heating and cooling rates were 200°C/hour. Pellets were held at 400°C for 1 hour to allow for binder burn out. Density was calculated geometrically and all pellets achieved a relative density of at least 95% of theoretical.

3.3 Sample Characterization

Microstructural and electrical properties of bulk and thin film samples were characterized using various methods. This section will detail the techniques used.

3.3.1 Impedance Spectroscopy

Due to the differences in sample geometry and microstructure, impedance measurements performed on thin film and bulk samples required the use of different equipment and experimental conditions. This section will describe in detail the impedance spectroscopy techniques used in this work. See section 2.3 for background information on EIS.

3.3.1.1 Thin Film Samples

Two-point AC electrochemical impedance spectroscopy (EIS) was performed on the samples in air from 100-300°C. Samples were heated using a digitally controlled hotplate and surface temperatures were confirmed using an optical pyrometer. Electrical contacts with top and bottom electrodes were made using a Micromanipulator 450 PM Test Station with tungsten probe tips. The test station was connected to an Agilent Precision Impedance Analyzer 4924A. Measurements were taken over the frequency range 40 Hz – 1 MHz using an oscillating voltage of 300 mV. Nyquist plots from the impedance data were fit with ZView software using an equivalent circuit composed of a resistor in parallel with a constant phase element until the %error of the fit was minimized.

3.3.1.2 Bulk Samples

Ionic conductivity measurements were performed using two-point AC electrochemical impedance spectroscopy (EIS). A Solartron SI 1260 impedance

analyzer was used to take measurements in air from 250 - 700°C over the frequency range 0.1 Hz – 32 MHz. Pellets were polished using SiC paper (up to 600 grit) to achieve smooth parallel surfaces that were then painted with Pt ink (Heraeus, CL 11-5349) and finally fired at 900°C for 1 h to ensure a good electrode-ceramic interface. Pt wires with a diameter of 127 µm were attached to the electrodes using conductive silver paste (SPI Supplies) which was allowed to dry before the samples were installed in a glass reactor for measuring. The thermocouple was kept in close proximity to the samples to ensure an accurate temperature reading and pellets were held at each temperature for at least 20 min to allow them to reach equilibrium. Data was fit with ZView software using equivalent circuit analysis consisting of an inductor, to model the experimental setup, in series with two constant phase element-resistor parallel components, to model the grain core and grain boundaries. Fits were performed such that the %error of the fit was minimized. Refer to Appendix B for more information. Reported conductivity values are the average of three samples.

3.3.2 X-ray Diffraction

XRD patterns from the calcined powders were collected using a Philips APD 3720 to ensure the complete dissolution of the dopants into the host ceria lattice. Lattice parameters were determined from XRD data using the Nelson-Riley extrapolation technique⁵⁸. XRD analysis was performed on thin film samples using a Philips APD 3720 after both the Pt and ceria deposition steps to ensure the layers were highly oriented. D-spacings for both layers were calculated using XRD data to determine if the layers were in tension or compression.

Though phi and omega scans would be helpful in further characterizing the microstructure of thin film samples, the inability to access necessary diffraction equipment has prevented the inclusion of this data.

3.3.3 Profilometry

Profilometry was performed using a Dektak 150 Surface Profiler to determine the thickness of the ceria films. Scans were 500 μm long beginning on the Pt layer and moving onto the NDC layer. To get a more reliable measurement, the probe was set to detect step changes in both the positive and negative directions. Thicknesses were determined based on an average of three separate scans.

3.3.4 Transmission Electron Microscopy

While the TEM work was performed by Dr. Nicholas Rudawski under guidance of Prof. Nino and R. M. Kasse, the general process is describe here for completeness. The microstructure of thin film samples were investigated by TEM using a combination of high-resolution cross-sectional TEM (HR-XTEM), selected area electron diffraction (SAED), and convergent beam electron diffraction (CBED) using a JEOL 2010F transmission electron microscope operating at 200 KeV with spherical aberration coefficient $C_s = 1.0$ mm. Samples for TEM analysis were prepared via site-specific focused ion beam (FIB) milling using an FEI DB235 dual beam scanning electron microscope/FIB system using an in-situ lift-out method as described elsewhere⁵⁹; the samples were prepared such that the beam direction (foil normal) used for TEM analysis was $B = [-1100]$. Prior to FIB processing, the specimens were coated with a ~ 100 nm-thick conductive C layer to protect the surface of the structure during the initial stages of in-situ FIB-assisted deposition of a protective Pt layer.⁶⁰ Immediately prior to

TEM analysis, the sample was plasma cleaned for 2 min using 75%/25% Ar/O₂ plasma to prevent carbon contamination. The specimen was etched for 10 s in a 25:1:26 (by volume) HNO₃:HF:H₂O solution, which was reported to be highly effective and selective in the removal of ion beam-damaged Al₂O₃.⁶¹ This etching strategy completely removed the protective C and Pt layers, but did not affect the thickness of the NDC or Pt layers; the resulting sample quality was sufficient to allow for high-quality HR-XTEM imaging.

3.3.5 Atomic Force Microscopy

While the AFM work was performed by Mina Hanna and Alexander Rudy under guidance of Prof. Nino and R. M. Kasse, the general process is describe here for completeness. AFM analysis was performed using an MFP-3D Stand Alone AFM (Asylum Research LLC). Images were taken in tapping mode using a model AC240TS (Olympus) silicon probe tip (radius 9 ± 2 nm) with an Al reflex coating. Root mean square (RMS) roughness data and line scans were analyzed using Igor Pro software (Wavemetrics Inc).

3.3.6 Scanning Electron Microscopy

Microstructure analysis of bulk samples was performed using a Jeol JCM-5000 Neoscope scanning electron microscope (SEM) on both fracture surfaces and polished and thermally etched pellet cross sections. Pellets were prepared for thermal etching by mechanical polishing using SiC polishing papers first and then finishing with Al₂O₃ slurries down to 0.05 μ m particle size. The polished samples were then ultrasonicated in methanol for 30 min, thermally etched at 1500°C for 1 h, and again ultrasonicated for

30 min in methanol. Grain size values were determined by examining SEM images of polished and thermally etched surfaces using ImageJ software.⁶²

CHAPTER 4
HIGHLY ORIENTED Nd_{0.1}Ce_{0.9}O_{2-δ} THIN FILMS ON Pt BOTTOM ELECTRODES

4.1 Introduction

Understanding the effects of composition and microstructure on the transport properties of rare-earth doped ceria is crucial to enhancing the ionic conductivity of these materials in the intermediate temperature range for use as electrolytes in SOFC applications. The role of grain size in determining the ionic conductivity is of particular interest. Distinguishing between grain and grain boundary ionic conductivity using data from bulk impedance measurements is difficult especially in samples with nanometer-sized grains, making it difficult to precisely determine the effect of grain size on grain ionic conductivity.⁶³ Nonetheless the development of newer methods for modeling conductivity in these materials has yielded some exciting results.³⁶ Some studies report that when nanostructured materials are synthesized, grain boundaries and interfaces become highly conductive paths for oxygen ion transport, thereby increasing the total ionic conductivity by orders of magnitude.⁶⁴⁻⁶⁶ Conversely, other investigations have concluded that since grain boundary concentration is increased as grain size decreases, and grain boundaries tend to block oxygen ion transport, total ionic conductivity is lower in nanostructured materials.^{37,67-69} Tuller suggests that this discrepancy may be due to a failure to separate ionic conductivity and total conductivity which includes contributions from electrons and holes, mechanisms that degrade SOFC performance.⁶⁶

The microstructure of thin film samples varies depending on the deposition method used, substrate material, heat treatment, and other processing variables. Films can be single crystals, have columnar grains, or be polycrystalline, as seen in Figure 4-

4-1 below. Since polycrystalline samples have grain boundaries at many random orientations it is not possible to completely separate grain and grain boundary conductivity. Single crystal films would allow for the direct measurement of grain conductivity due to the lack of grain boundaries. Films exhibiting columnar grain structures also allow for the direct measurement of grain conductivity provided across-plane impedance measurements are performed since there would be no grain boundaries perpendicular to the path of conduction. Figure 4- below illustrates potential in-plane and across-plane electrode geometries for measuring thin film samples.

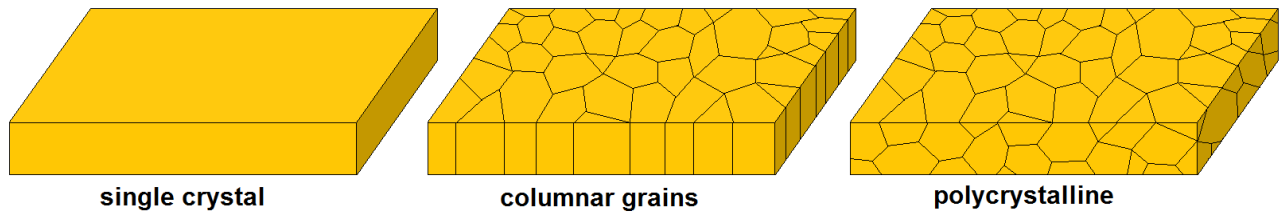


Figure 4-1. Schematic illustration of films with single crystalline, columnar grain, and polycrystalline microstructures, from left to right respectively.

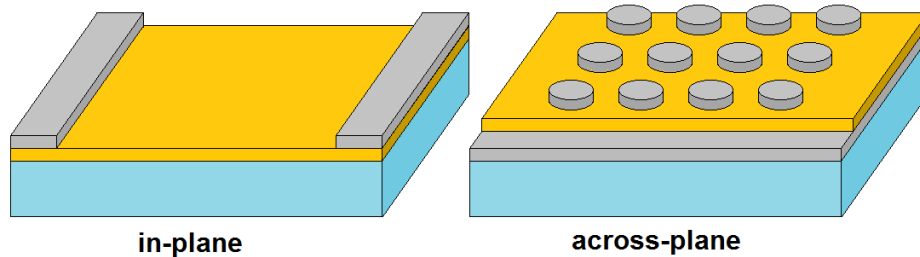


Figure 4-2. Schematic illustration of electroding configurations for in-plane (left) and across-plane (right) electrical measurements of thin film samples.

Gobel *et al.* investigated the effect of thickness on the ionic conductivity of both GDC and undoped ceria thin films with epitaxial and columnar grain microstructures.³⁷ Grain structure was controlled by depositing on different substrates; films deposited on Al_2O_3 (0001) were epitaxial while those deposited on SiO_2 (0001) exhibited columnar

grains. Since films were deposited on insulating substrates, in-plane electrical measurements were performed using an electrode setup similar to what is depicted in Figure 4-2. The individual contributions from grain and grain boundary could not be separated due to stray capacitance orders of magnitude larger than that of either the grain or grain boundary capacitance, so only total conductivity was reported.³⁷ Dewetting of the platinum electrodes was noticed after electrical measurements on polycrystalline samples and was attributed to the presence of grain boundaries as this was not observed for epitaxial samples. Ionic conductivity was not influenced by the dewetting as electrodes were still electrically interconnected in all cases.³⁷

Ionic conductivity in epitaxial GDC thin films showed no dependence on thickness. This indicates that the film/substrate interface has no effect on conductivity in epitaxial samples when measured in-plane. Columnar grain GDC samples, however, showed an increase in total ionic conductivity with an increase in film thickness. This is explained by the corresponding decrease in lateral grain size with increasing film thickness, resulting in a decrease in grain boundary concentration.³⁷ Important to note is the blocking nature of grain boundaries in these samples even with grain size on the order of tens of nanometers.

Huang *et al.* also measured the ionic conductivity of polycrystalline GDC films as a function of thickness and found that total ionic conductivity increases three to four orders of magnitude as thickness decreases.⁶⁸ Initially these results may seem to contradict those of Gobel *et al.* However, once experimental conditions are considered the results actually tell the same story. Polycrystalline thin film samples, with microstructures similar to that depicted in Figure 4-1, were deposited on platinized

silicon substrates and across-plane measurements were performed. Films synthesized in this study had grains on the order of 10-50 nm in diameter.

The increase in total ionic conductivity was attributed to the reduction in the number of grain boundaries perpendicular to the path of conduction with decreasing film thickness.⁶⁸ Again, grain boundaries in nanocrystalline samples are presented as being blocking, limiting the conduction of oxygen ions and reducing total ionic conductivity. Additionally, it is reported that grain conductivity increases with decreasing film thickness, further enhancing conductivity of thinner films. However, since there were grain boundaries present in the samples this could not be directly measured.

While the thin film studies discussed above seem to imply that grain boundaries remain blocking even in nanostructured samples, several other studies report that grain boundaries become highly conductive paths for oxygen ions when grain size is on the order of nanometers.⁶⁴⁻⁶⁶ Bellino *et al.* report an order of magnitude increase in total ionic conductivity in nanocrystalline samples compared to microcrystalline samples due to increased grain boundary ionic diffusivity.⁶⁴ A change in transport mechanism with temperature is also reported, with bulk transport being dominant at higher temperatures and grain boundary transport dominant at lower temperatures. Similar results are reported by Rupp *et al.* and Tuller *et al.* though both mention the possibility of the increased conductivity being attributed to electronic conduction rather than ionic conduction and suggest further studies to determine which mechanism is responsible.^{65,66} Across-plane ionic conductivity measurements on highly oriented films of varying thicknesses would provide critical new information regarding size effects in these materials by allowing grain ionic conductivity to be measured directly, but the

community has thus far been unable to successfully synthesize highly oriented doped ceria thin films on bottom electrodes.^{37,68,70}

In this study it has been shown for the first time the preparation of highly oriented thin film samples of doped ceria with a bottom electrode. The first ever impedance measurements of these samples have been performed as a function of film thickness to directly determine size effects on grain ionic conductivity.

4.2 Structural Characterization

Highly oriented thin film samples of $\text{Nd}_{0.1}\text{Ce}_{0.9}\text{O}_{2-\delta}$ with thicknesses ranging from 4-190 nm were prepared such that the across-plane ionic conductivity could be measured as a function of film thickness. Figure shows the X-ray diffraction (XRD) pattern of a 43 nm sample. It is evident that the film is highly oriented as the only peaks attributed to the ceria layer are the (111) and (222). The other peaks are from the single crystal *a*-plane sapphire substrate and the Pt bottom electrode layer, which is also highly oriented and oriented along the same direction as the ceria layer. That NDC grows so highly oriented on the highly oriented Pt (111) layer is somewhat interesting. Joo *et al.* deposited GDC on Pt (111) substrates and obtained films with a polycrystalline microstructure⁷⁰ while Abid *et al.* reported oriented growth of Pt (111) on CeO_2 (111).⁷¹ Lattice mismatch with the sapphire substrate could cause the Pt layer to be under strain which may contribute to the NDC layer being so highly oriented. Figure shows XRD patterns for films 4-190 nm thick, proving that this process is reproducible and can be used to deposit films covering a relatively wide range of thicknesses. It is proposed that the NDC layer grows epitaxially within each grain due to alignment of the Pt ($1\bar{1}0$) and NDC ($3\bar{2}\bar{1}$) directions based on coincident site lattice (CSL) calculations.

XRD patterns obtained for films ranging from 4-190 nm thick prove that this process is reproducible and can be used to deposit films covering a relatively wide range of thicknesses.

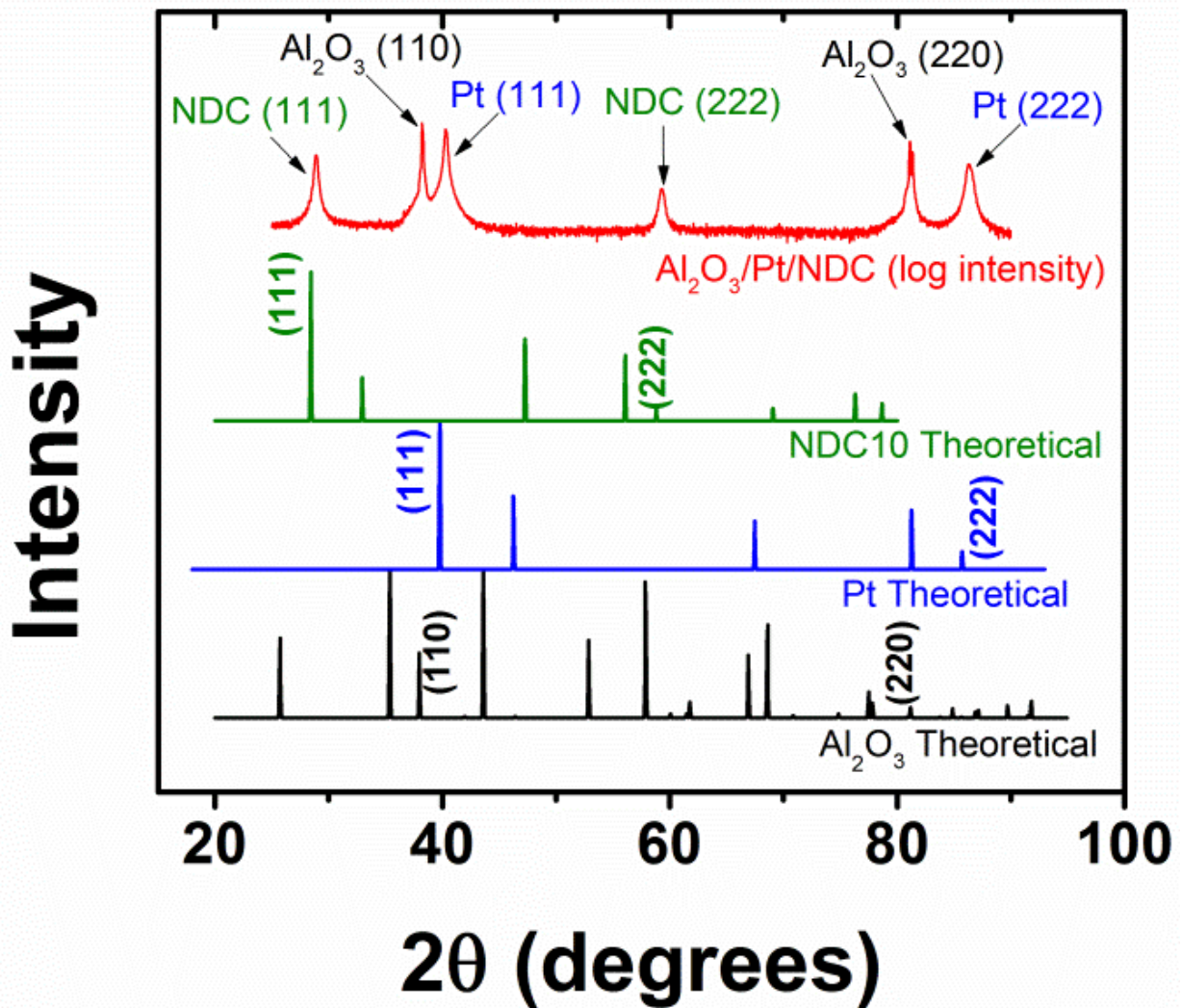


Figure 4-3. X-ray diffraction pattern of a 43 nm thin film sample as compared to the theoretical patterns for Al₂O₃, Pt, and 10% Nd-doped ceria.

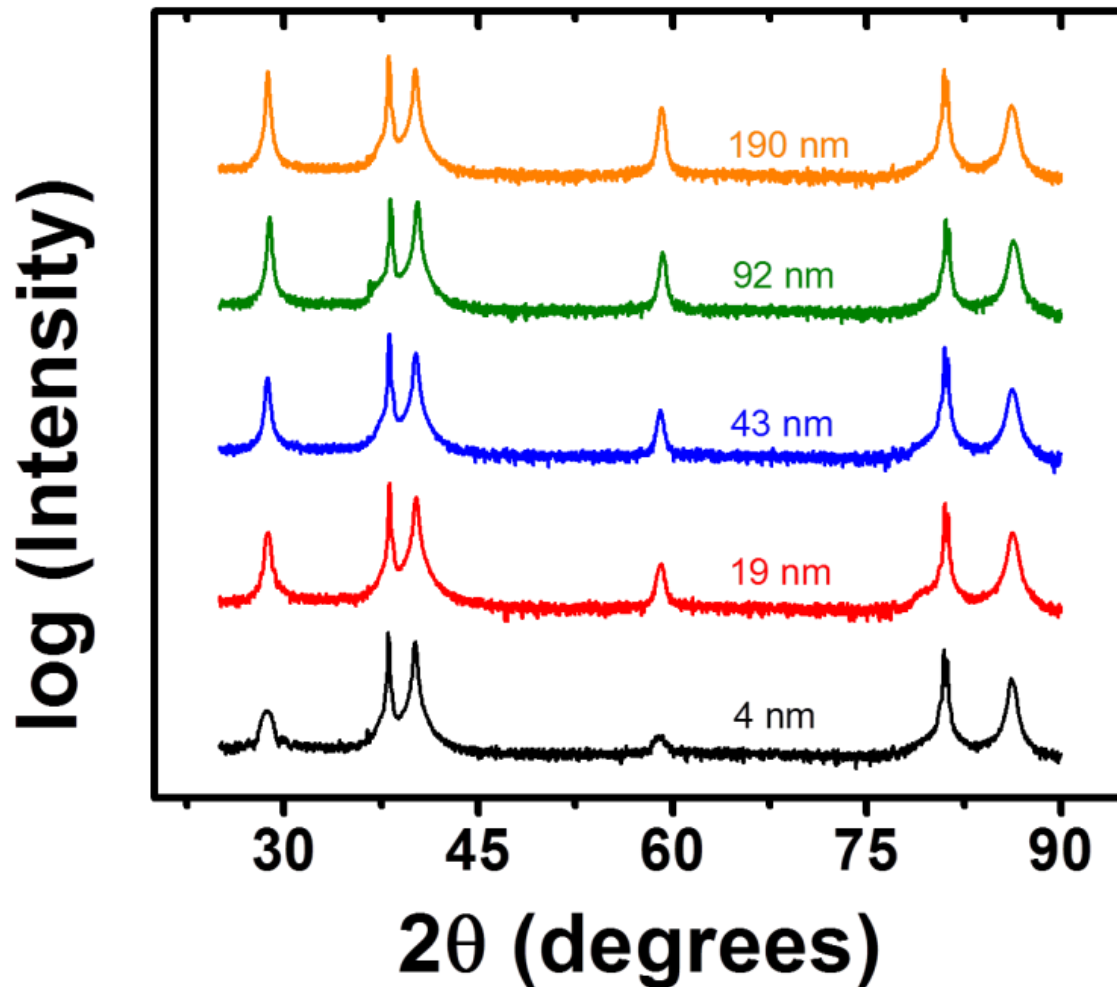


Figure 4-4. X-ray diffraction patterns for thin film samples of different thicknesses ranging from 4-190 nm.

Transmission electron microscopy (TEM) data confirms that both the Pt and ceria layers are highly oriented along the (111) direction, as seen in Figure 4-5. The high resolution cross-sectional TEM (HR-XTEM) images show alignment of the different lattice fringes across both interfaces. The selected area electron diffraction (SAED) and convergent beam electron diffraction (CBED) patterns show that certain crystallographic planes in each of the three materials are aligned. D-spacings measured from the high resolution TEM micrographs are in good agreement with bulk values reported in literature.

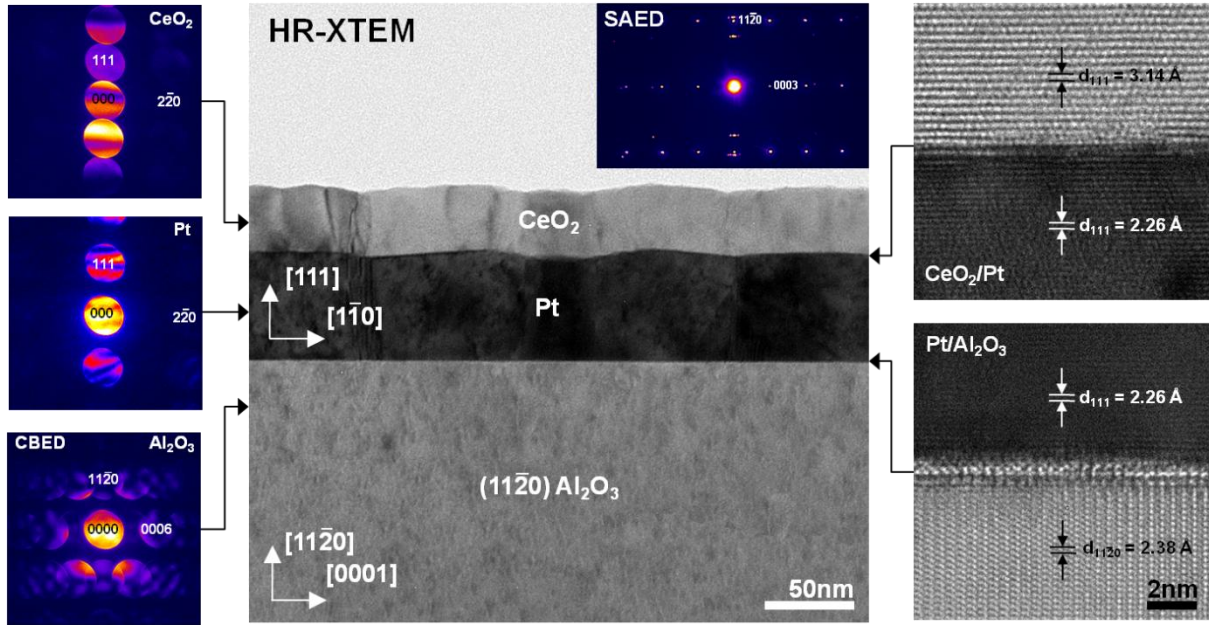
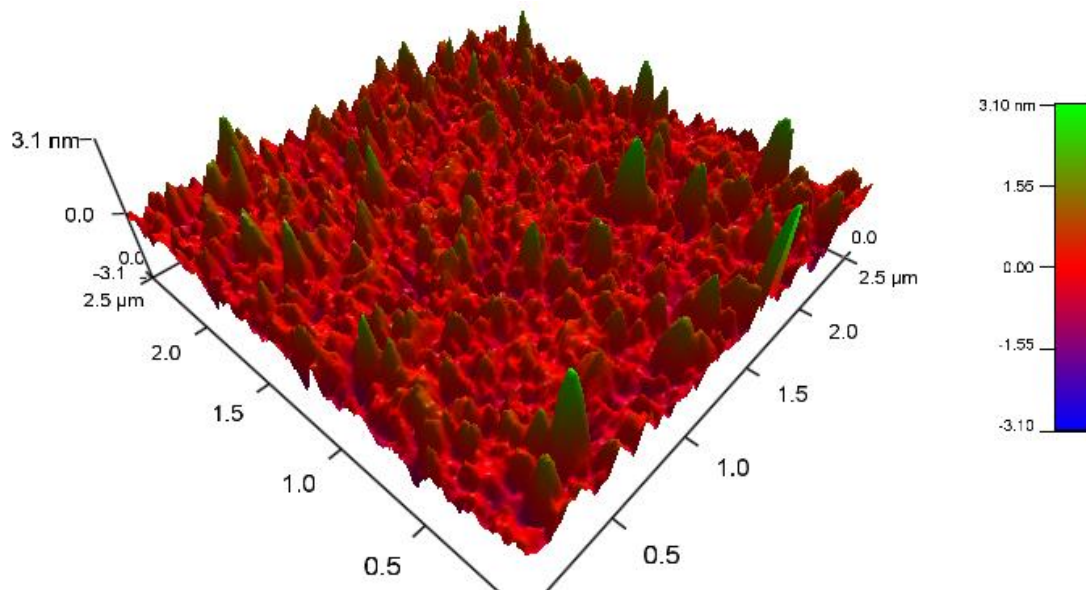


Figure 4-5. Convergent beam electron diffraction (left), selected area electron diffraction (center inset), and high resolution cross-sectional TEM (right) all confirm that both the Pt and NDCC layers are highly oriented in the $[111]$ direction.

Results of atomic force microscopy (AFM) analysis are shown in Figure . The root mean square (RMS) roughness of the Pt layer is $\sim 490 \text{ pm}$ while the ceria layer has a RMS roughness of $\sim 0.7\text{-}1.9 \text{ nm}$. This corresponds to a variation in thickness of less than 2% for even the thinnest ceria films tested.



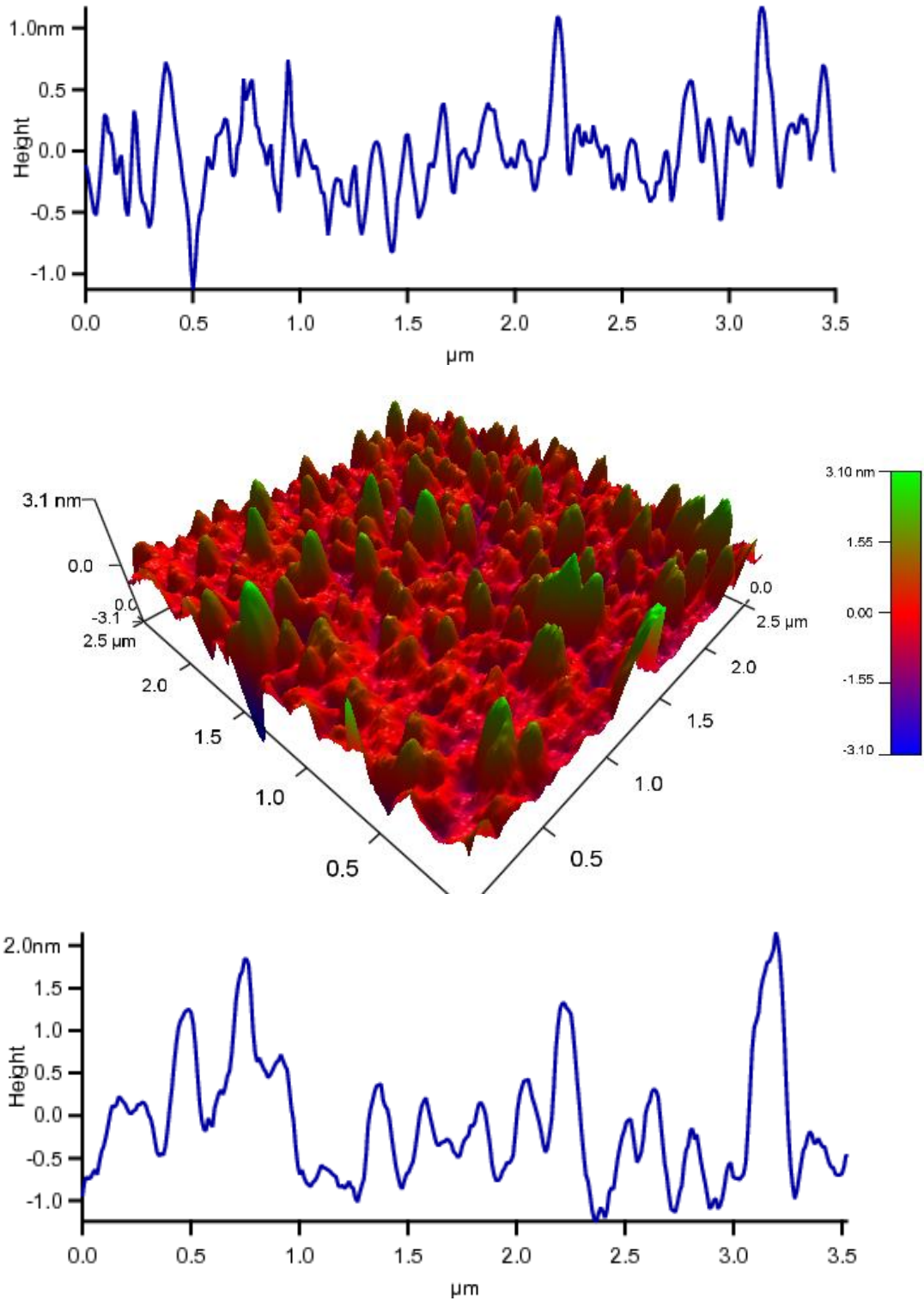


Figure 4-6. Atomic force microscopy topography maps and line scans of a Pt layer (top) and a 43 nm NDC film (bottom). Note the different scales used on the line scan plots.

4.3 Ionic Conductivity

Characteristic ionic conductivity data is shown in the figures below. Figure shows a typical Nyquist plot of the complex impedance obtained from an impedance measurement. Only one semicircle is present indicating that there was no grain boundary contribution to the conductivity. Measured conductivity values for thin film samples of 43 and 190 nm thicknesses are slightly lower but comparable to values obtained from bulk polycrystalline samples, as seen in Figure below. The measured conductivity of the films may be lower than that of the bulk for a few reasons. Liu *et al.* reported for Sm/Nd co-doped ceria films, conduction along the [111] direction may be lower than other directions.⁷² Also, Tsuchiya *et al.* found that the oxygen exchange rate is slower in highly textured films when compared to polycrystalline films.⁷³

Conductivity appears to be independent of film thickness, similar to that reported by Gobel *et al.* for in-plane measurements of epitaxial GDC films.³⁷ Considering the fact that the space charge layers (SCLs) near interfaces in doped ceria are on the order of 2-5 nm³⁶, and thus no interaction between SCLs would occur in films of the thicknesses studied, it makes sense that the grain core conductivity remains constant. Interestingly, the conductivity values here obtained for the films fall within broad conductivity values reported in literature for doped ceria thin films with different microstructures, see Figure . One possibility is that this is simply a result of the temperatures for which the values are reported. Recall that Bellino *et al.* reported a change in transport mechanism from grain boundary to bulk dominated with increasing temperature.⁶⁴ Additional measurements covering a wider range of thicknesses and temperatures may help to better determine the relationship between film thickness and grain ionic conductivity.

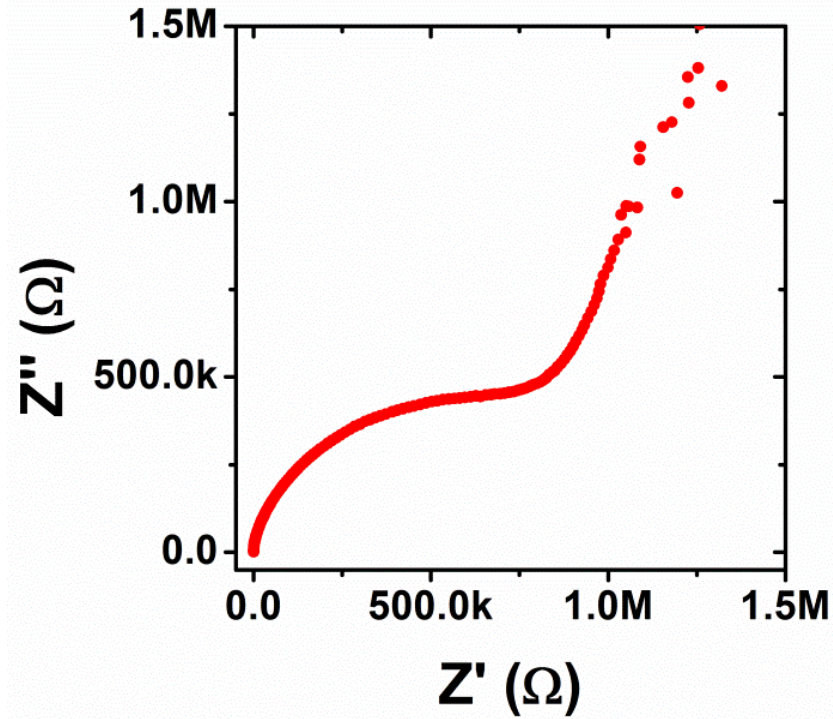


Figure 4-7. Typical Nyquist plot obtained from impedance measurements of thin film samples.

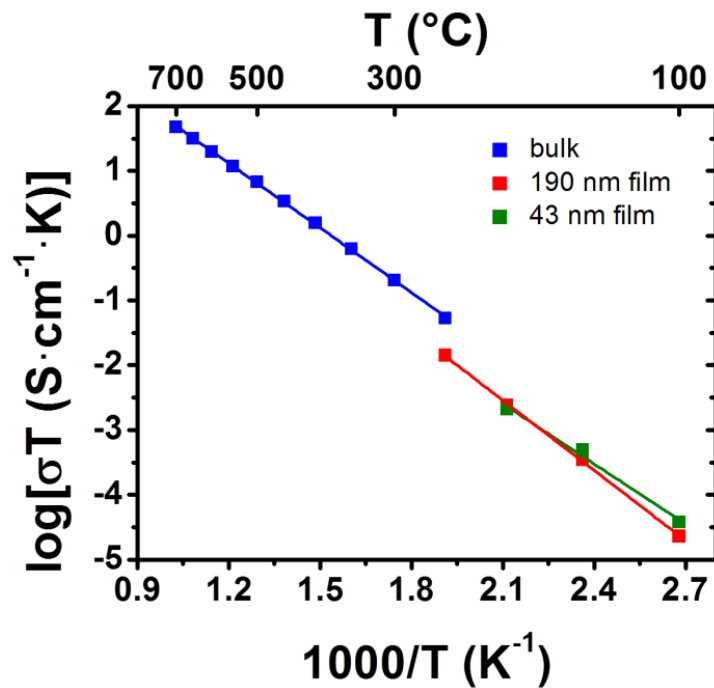


Figure 4-8. Arrhenius plot of grain ionic conductivity for 10% Nd-doped ceria comparing thin film samples of two different thicknesses and data obtained from a bulk polycrystalline sample.

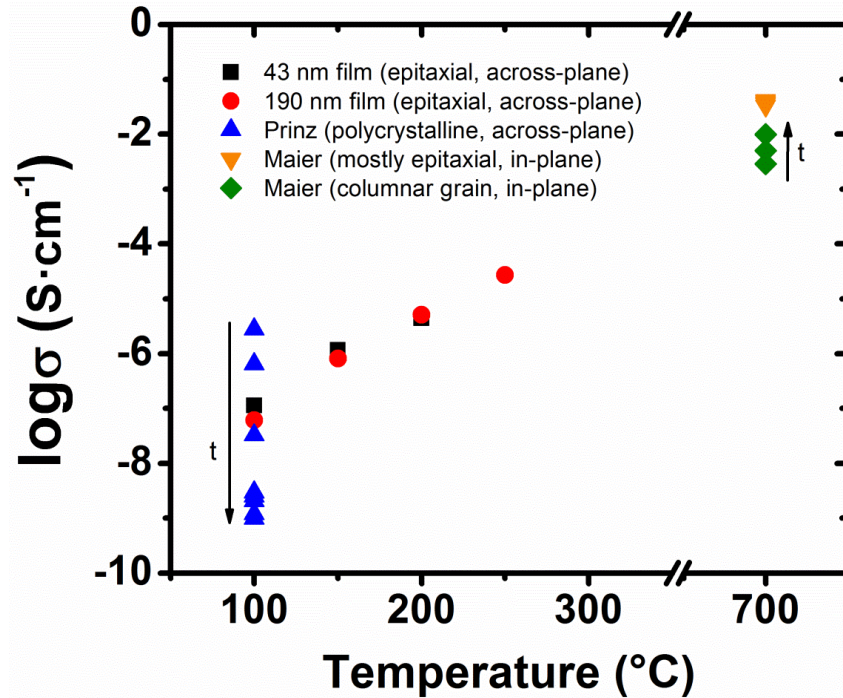


Figure 4-9. Plot of the log of conductivity versus temperature. Across-plane data from the highly oriented thin film samples measured in this study show good agreement with literature data. The arrows indicate increasing film thickness.^{37,68}

4.4 Summary and Conclusions

Highly oriented doped ceria thin films were deposited on Pt bottom electrodes for the first time and the first across-plane ionic conductivity measurements of these films were performed. DC sputtering was used to deposit a highly oriented layer of Pt (111) on *a*-plane sapphire substrates. The highly oriented doped ceria layer was then deposited using pulsed laser deposition. Such thin film samples allow for the first time the direct measurement of grain ionic conductivity of doped ceria since there is no grain boundary contribution to the across-plane conductivity measurements. Ionic conductivity data indicates inconsistencies in literature may simply be a result of the experimental conditions used in each study and failure to distinguish between ionic and electronic conduction.

CHAPTER 5
IONIC CONDUCTIVITY OF $\text{Sm}_x\text{Nd}_y\text{Ce}_{0.9}\text{O}_{2-\delta}$

5.1 Introduction

In the dilute region, when dopant concentration is small, the migration enthalpy, E_m , for ionic conduction is independent of dopant concentration so a minimization of defect association enthalpy, $E_{ass.}$, is necessary to increase ionic conductivity.¹² While finding the ideal dopant type and concentration is essential to both lowering activation energy and increasing ionic conductivity, the optimum composition may not be the same for both properties.⁹ Kilner *et al.* calculated association energies for dopants creating an effective charge of plus one and plus two and concluded that dopants causing an effective charge of plus one resulted in a lower association energy and thus a higher conductivity.⁷⁴ The composition with the highest conductivity will be the one with the best balance between a high pre-exponential and a low activation energy. Ceria doped with Gd^{3+} and Nd^{3+} has shown the highest grain ionic conductivity of all singly doped materials in the IT range.^{16,18} Co-doping ceria has been shown to increase ionic conductivity to values above those of singly doped materials^{19,22,25,75-80} though this is not the case for all systems.⁸¹ In co-doped materials a reduction in the growth of defect clusters is observed which lowers the association enthalpy.^{21,23} The reduction in defect clusters results in less local ordering of the structure which causes an increase in the conductivity.²⁴

Attempting to address this, density functional theory calculations by Andersson *et al.* predicted that a dopant with an atomic number near that of Pm^{3+} (61), which has an ionic radius of 1.093 Å, would result in the lowest activation energy and thus highest ionic conductivity because oxygen vacancies in this system show almost no preference

for being in nearest neighbor or next nearest neighbor positions with respect to the dopant cations.^{11,82} Since Pm^{3+} is radioactive and not suitable for use in fuel cell applications a co-doping scheme using Sm^{3+} (62) and Nd^{3+} (60) was suggested such that an average atomic radius near the ideal value could be achieved. Work by Omar *et al.* showed that 1:1 co-doping in $\text{Sm}_{x/2}\text{Nd}_{x/2}\text{Ce}_{1-x}\text{O}_{2-\delta}$ showed conductivity values intermediate between the singly doped materials with Nd-doped ceria exhibiting the highest grain ionic conductivity.^{16,20} More recent studies have determined that the addition of small amounts of a second dopant enhances conductivity beyond that of singly doped materials and 1:1 co-doped.^{25,75} For example, Park *et al.* report that in the $\text{Ce}_{0.8}\text{Gd}_{0.2-x}\text{Dy}_x\text{O}_{2-\delta}$ system, while 1:1 co-doping actually degrades ionic conductivity, when $0.1 \leq x \leq 0.3$ ionic conductivity is increased.²⁵ Similarly, Dholabhai *et al.* found that for ceria doubly doped with Pr^{3+} and Gd^{3+} , Gd-rich compositions exhibited the highest conductivity.⁷⁵ Therefore, a systematic investigation of this effect within the $\text{Sm}_x\text{Nd}_y\text{Ce}_{0.9}\text{O}_{2-\delta}$ system is of significant interest and is the focus of this chapter.

5.2 Phase Analysis and Microstructural Characterization

Fig shows the room temperature XRD patterns for all of the measured compositions. All samples show peaks corresponding to the cubic fluorite structure with no additional peaks confirming the complete dissolution of dopants into the host ceria lattice. Lattice parameters calculated from X-ray data increased as dopants shifted from pure Sm^{+3} to pure Nd^{+3} , following Vegard's law⁸³ as expected since the ionic radius of Nd^{+3} is larger than that of Sm^{+3} .⁸²

The secondary SEM image of a fracture surface in Fig shows the typical microstructure of all of the samples tested. All samples showed very low porosity which

confirms the high relative densities calculated from geometrical measurements. Grain size analysis using ImageJ software showed that the average grain size was around 11 μm and is independent of dopant content; starting powders had a mean particle size of 0.135 μm . Some studies have reported grain sizes around 5 μm ^{16,20,24} while others reported samples with average grain diameters of 1 μm or less. ^{14,17,25} The larger average grain size reported here is the result of a higher sintering temperature (1600°C) which may also affect dopant segregation to grain boundaries and increase grain ionic conductivity.⁸⁴

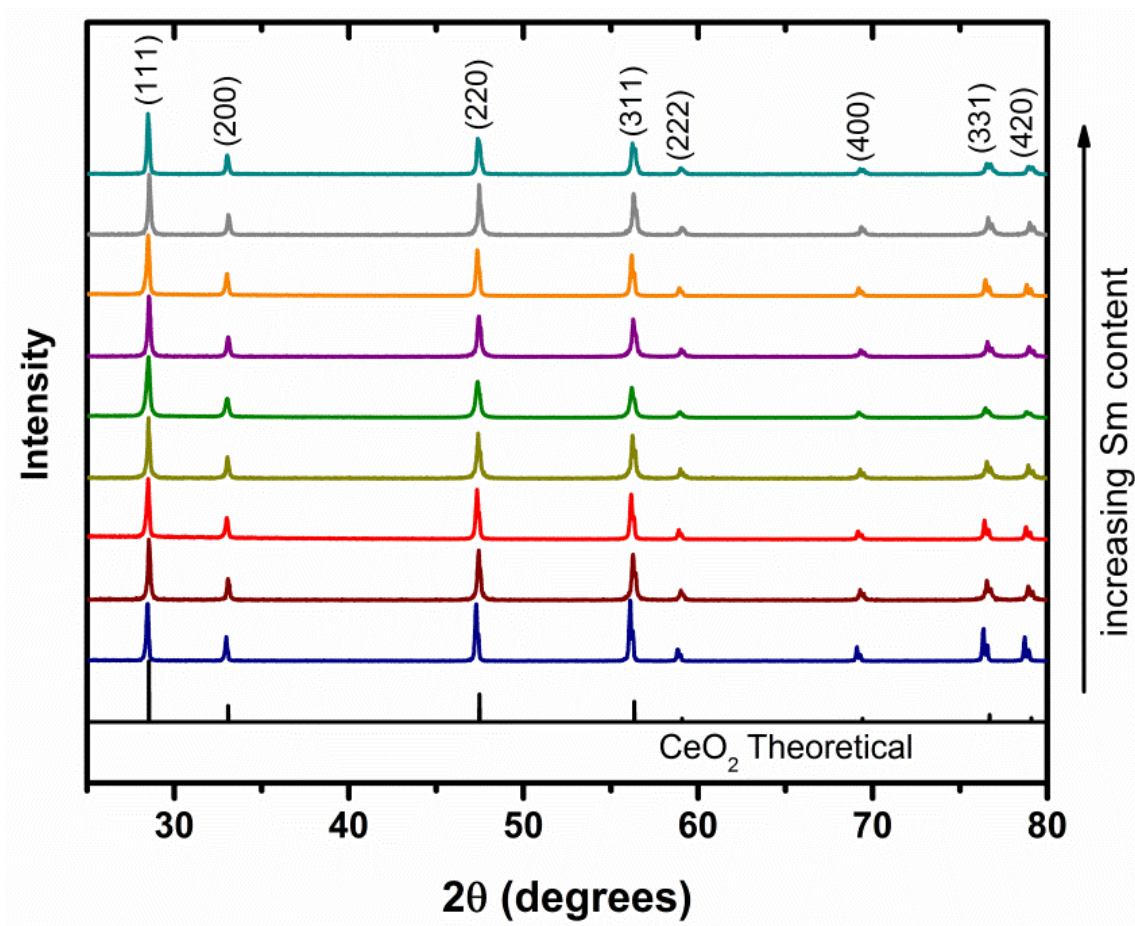


Figure 5-1. X-ray diffraction patterns for $\text{Sm}_x\text{Nd}_y\text{Ce}_{0.9}\text{O}_{2-\delta}$.

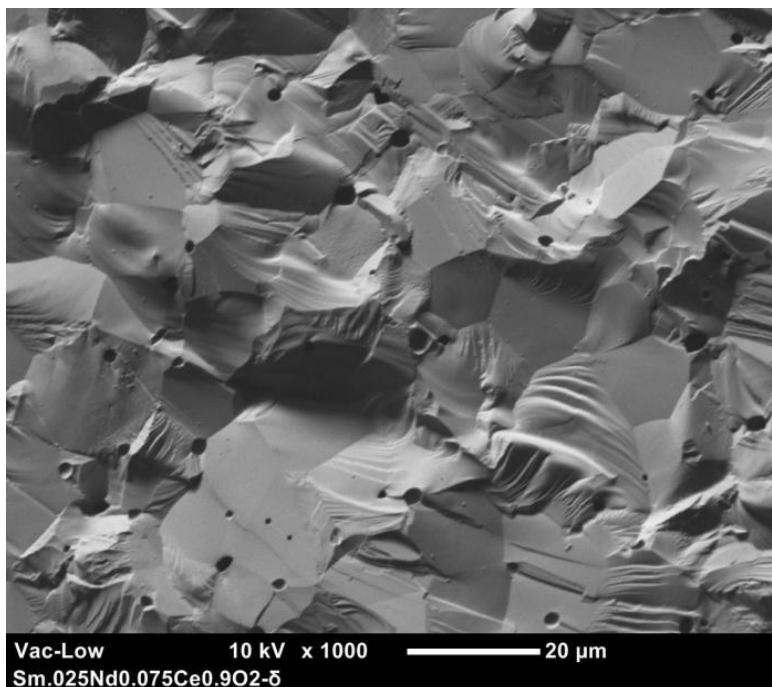


Figure 5-2. SEM image of a fracture surface of $\text{Sm}_{0.025}\text{Nd}_{0.075}\text{Ce}_{0.9}\text{O}_{2-\delta}$ showing the typical microstructure of all samples.

5.3 Ionic Conductivity

Fig shows the plot of $\log(\sigma T)$ versus $1000/T$ for the nine compositions examined. Note that all of the compositions exhibit Arrhenius behavior and the lines are nearly superimposed upon one another. It is important to note that all the conductivity values reported are the density corrected averages of three pellets of different geometric aspect ratios. Density corrections involved dividing the measured conductivity by the calculated relative density.⁸⁵

The plot of grain ionic conductivity versus dopant concentration at temperatures ranging from 400-700°C presented in Fig shows a maximum in conductivity for $\text{Sm}_{0.075}\text{Nd}_{0.025}\text{Ce}_{0.9}\text{O}_{2-\delta}$ with a value of $0.0507 \pm 0.0015 \text{ S}\cdot\text{cm}^{-1}$ at 700°C. However this increase is only ~8% over the 1:1 co-doped composition which is statistically insignificant given the experimental error. The variation in conductivity also appears to

increase with increasing temperature, but when the error bars, which also get larger, are taken into account, it is clear that this perceived variation is statistically insignificant. It is anecdotal to note that Andersson *et al.*¹¹ suggested that an ideal dopant should have an effective atomic number between 61 and 62 and this dopant combination has an effective atomic number of 61.5. However, it is clear that at the unit cell level a material is composed of individual atoms, not averages of atoms. Also, it is important to note that the critical dopant radius (or atomic number) of the ideal dopant is temperature dependent; thus these values are to be assessed at the operating temperatures of interest as recently shown.¹⁶

Furthermore and interestingly, although it shows the highest conductivity, $\text{Sm}_{0.075}\text{Nd}_{0.025}\text{Ce}_{0.9}\text{O}_{2-\delta}$ is not the composition with the lowest activation energy nor does it have the highest pre-exponential coefficient as seen in Table . This results from the fact that there are two competing mechanisms affecting the activation energy. Reduction in the amount of oxygen vacancy ordering due to an increase in configurational entropy will reduce the activation energy.⁸⁶ At the same time, the increase in the lattice parameter from that of pure ceria (5.4126 Å) tends to increase the activation energy.⁷⁷ Configurational entropy values, calculated following Guan *et al.*⁷⁶ using Equation 5-1 below where R is the ideal gas constant , are reported in Table 5-1. As dopants shift from pure samarium to pure neodymium, both the activation energy and pre-exponential coefficient increase as seen in 5-1. Sha *et al.* also reported about samples of co-doped ceria electrolytes that had higher conductivity values despite also having higher activation energy values.⁷⁷

$$S = R[0.9\ln 0.9 + (0.1 - x)\ln(0.1 - x) + x\ln x] \quad (5-1)$$

As noted above, Park *et al.*²⁵ reported that conductivity values increased significantly in $\text{Ce}_{0.8}\text{Gd}_{0.2-x}\text{Dy}_x\text{O}_{2-\delta}$ co-doped ceria with the addition of small concentrations (2-3%) of the second dopant while larger concentrations actually diminished conductivity and Dholabhai *et al.*⁷⁵ reported a similar increase in conductivity in the Pr-Gd co-doped ceria system for samples rich in Gd relative to Pr. This enhancement may occur because the addition of small amounts of a second dopant with a similar ionic radius disrupts local ordering of the cations and oxygen vacancies as suggested by Yamamura *et al.*²⁴ without any significant increase in activation energy. However, the compositions studied in this work indicate that this behavior is not exhibited by the $\text{Sm}_x\text{Nd}_y\text{Ce}_{0.9}\text{O}_{2-\delta}$ system as no enhancement in conductivity is observed.

Mori *et al.*⁸⁷ proposed the idea of an effective index to explain ionic conductivity in doped ceria systems, shown in Equations 5-2 and 5-3 below. Effective index takes into account the ionic radius of the host cation r_h , the average cation radius r_c , the average dopant radius r_d , and the effective oxygen radius r_o , which is dependent on the fraction of oxygen vacancies δ . Kilner *et al.* had previously suggested that ionic conductivity in fluorite oxides was related to r_d/r_h ⁸⁸, however, this fails to take into account oxygen vacancies. This approach suggests that a material with an effective index approaching 1 has an ideal fluorite crystal structure which leads to a higher ionic conductivity. Effective index values for the compositions studied can be found in Table 5-1 and agree with the experimental data in that both conductivity and effective index increase with increasing Nd content. However, it is important to note that the ionic radius values used in these calculations are at room temperature. A more appropriate

measure of effective index could be obtained if ionic radius values are operating temperatures were used.

$$\text{Effective Index} = \frac{r_c}{r_o} \times \frac{r_d}{r_h} \quad (5-2)$$

$$r_o = 1.4 \times \left(\frac{2-\delta}{2} \right) \quad (5-3)$$

Grain ionic conductivity in rare-earth-doped ceria has been shown to be a function of both dopant type and concentration and increases with temperature following an Arrhenius type relationship. Enhancement of ionic conductivity can be achieved by co-doping ceria with different elements. This work has shown that while further increases in conductivity can be realized by using a co-doping scheme which uses only small additions of a second dopant in some systems, allowing for larger increases in the pre-exponential coefficient relative to activation energy, this doping scheme does not enhance conductivity in all systems. The $\text{Sm}_x\text{Nd}_y\text{Ce}_{0.9}\text{O}_{2-\delta}$ system correlates well with the theory of effective index.

Finally, it is important to note that in doped ceria systems, segregation of dopants to the grain boundaries and microdomains containing ordered oxygen vacancies tends to lower ionic conductivity and degrade material performance. In co-doped systems, one dopant may preferentially segregate leading to non-uniform cation distribution and an increased deleterious effect on grain and grain boundary conductivity. The $\text{Sm}_x\text{Nd}_y\text{Ce}_{0.9}\text{O}_{2-\delta}$ system, exhibiting uniform conductivity across all (x/y) dopant ratios measured, appears to be free of these problems thus presenting a compositionally versatile system for use in IT-SOFC applications.

Table 5-1. Activation energy, pre-exponential coefficient, configurational entropy, and effective index values for all of the compositions studied.

Compound	Activation energy (eV)	Log(pre-exponential)	Configurational entropy, S (JK ⁻¹ mol ⁻¹)	Effective index
Sm _{0.1} Ce _{0.9} O _{2-δ}	0.646 ± 0.002	5.027 ± 0.022	2.703	0.799
Sm _{0.0875} Nd _{0.0125} Ce _{0.9} O _{2-δ}	0.647 ± 0.007	5.004 ± 0.052	3.016	0.802
Sm _{0.075} Nd _{0.025} Ce _{0.9} O _{2-δ}	0.654 ± 0.004	5.100 ± 0.029	3.170	0.806
Sm _{0.0625} Nd _{0.0375} Ce _{0.9} O _{2-δ}	0.657 ± 0.008	5.054 ± 0.050	3.253	0.809
Sm _{0.05} Nd _{0.05} Ce _{0.9} O _{2-δ}	0.653 ± 0.006	5.067 ± 0.045	3.279	0.812
Sm _{0.0375} Nd _{0.0625} Ce _{0.9} O _{2-δ}	0.659 ± 0.003	5.077 ± 0.027	3.253	0.815
Sm _{0.025} Nd _{0.075} Ce _{0.9} O _{2-δ}	0.663 ± 0.003	5.132 ± 0.021	3.170	0.818
Sm _{0.0125} Nd _{0.0875} Ce _{0.9} O _{2-δ}	0.659 ± 0.007	5.063 ± 0.047	3.016	0.821
Nd _{0.1} Ce _{0.9} O _{2-δ}	0.660 ± 0.006	5.108 ± 0.047	2.703	0.824

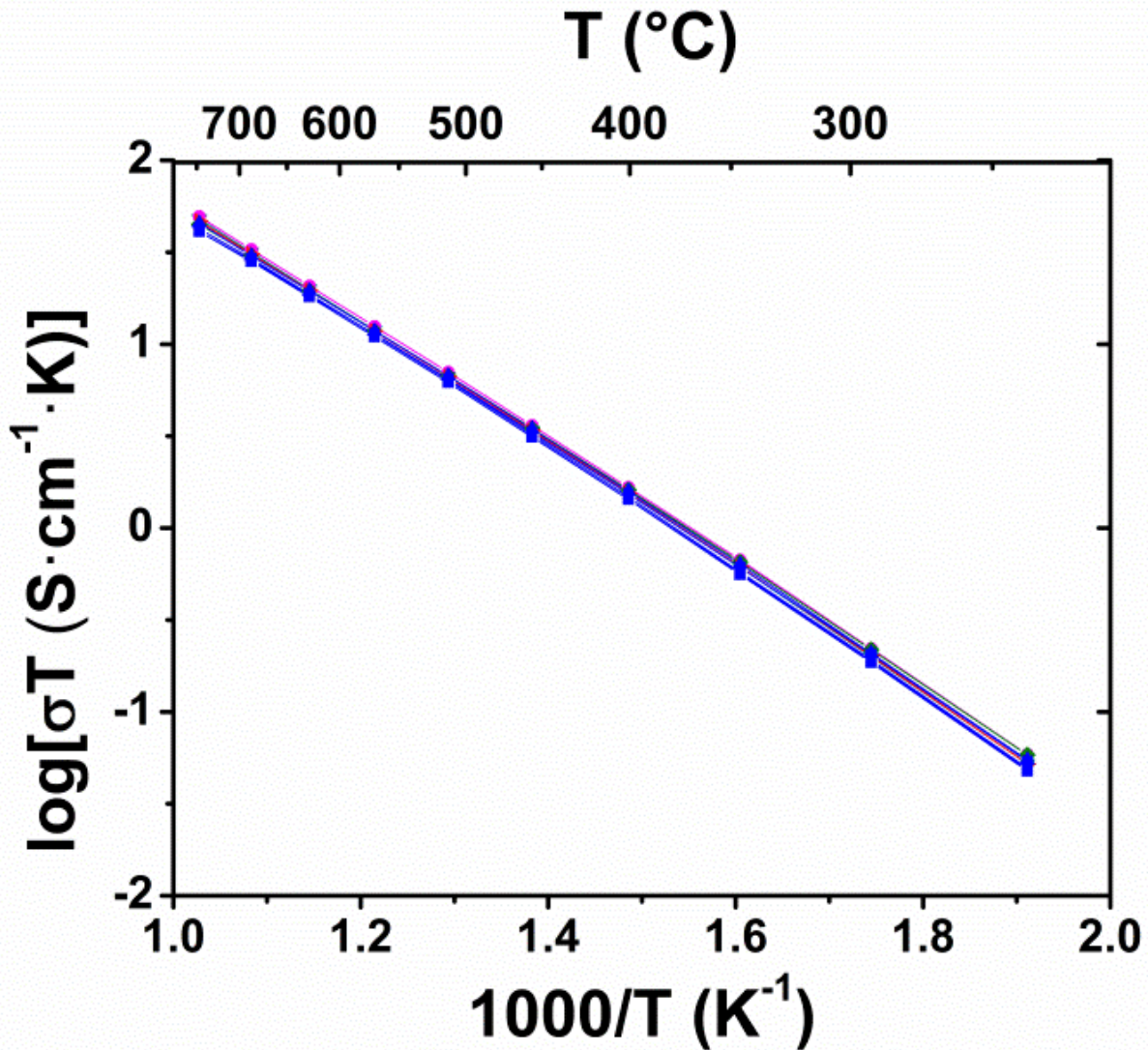


Figure 5-3. Arrhenius plot of grain ionic conductivity for all nine compositions investigated in the Sm_xNd_yCe_{0.9}O_{2-δ} system. There is no apparent variation in conductivity with composition.

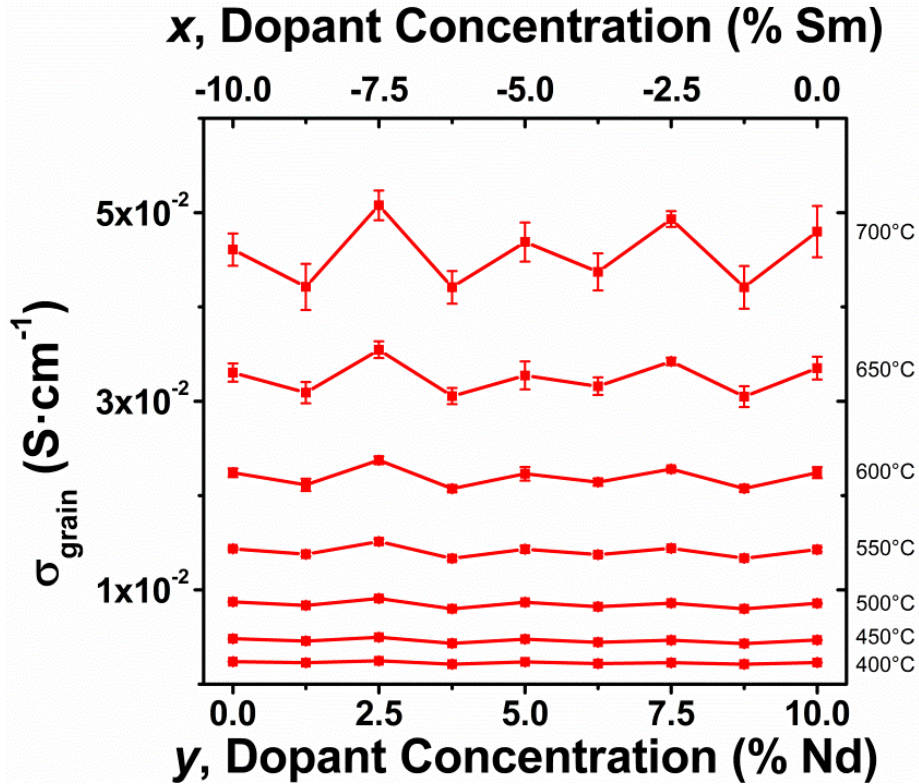


Figure 5-4. Plot of grain ionic conductivity versus dopant concentration for $\text{Sm}_x\text{Nd}_y\text{Ce}_{0.9}\text{O}_{2-\delta}$ from 400-700°C.

5.4 Conclusions

The development of materials with higher ionic conductivities in the intermediate temperature range is necessary for the advancement of IT-SOFC technology. Co-doping using Sm^{+3} and Nd^{+3} has demonstrated only intermediate values between those of the respective singly doped materials with Nd-doped ceria exhibiting the highest conductivity. This work investigated the $\text{Sm}_x\text{Nd}_y\text{Ce}_{0.9}\text{O}_{2-\delta}$ system and found that non 1:1 co-doping does not result in higher conductivity values than singly doped or evenly co-doped materials but rather follows the theory of effective index. Since co-dopant ratio (x/y) variations within the $\text{Sm}_x\text{Nd}_y\text{Ce}_{0.9}\text{O}_{2-\delta}$ system do not lead to significant conductivity changes it constitutes a versatile system impervious to potential performance degradation due to preferential dopant segregation and redistribution.

CHAPTER 6
IONIC CONDUCTIVITY ACROSS THE DISORDER-ORDER PHASE TRANSITION IN
THE NdO_{1.5}-CeO₂ SYSTEM¹

6.1 Introduction

Rare earth elements are considered the main candidates for doping ceria because of the resulting low activation energy for conduction.¹¹ They are also shown to slightly improve the mechanical properties of ceria⁹⁰, which is beneficial during cell fabrication and operation. Through doping, oxygen vacancies are introduced into the ceria lattice to maintain the overall charge neutrality of the material. At low dopant concentrations, these oxygen vacancies will distribute randomly in the host lattice in a disordered manner. However, in heavily doped ceria the oxygen vacancies tend to occupy preferential lattice sites around the dopant cations⁹¹ leading to the ordering of oxygen vacancies. The short-range ordering in ceria-based materials has been investigated by several groups.⁹¹⁻⁹⁵ For instance, Ou *et al.*⁹² observed experimentally the formation of nanosized domains exhibiting a C-type rare-earth oxide structure (C-type structure) in 25 mol% lanthanide (Ln)-doped ceria (Ln=Sm, Gd, Dy, and Yb); these ordered domains were believed to be the cause of the degraded ionic conductivity.

In heavily doped ceria oxygen vacancies tend to occupy preferential lattice sites around the dopant cations⁹¹ leading to the ordering of oxygen vacancies. The short-range ordering in ceria-based materials has been investigated by several groups.⁹¹⁻⁹⁵ For instance, Ou *et al.*⁹² observed experimentally the formation of nanosized domains exhibiting a C-type rare-earth oxide structure (C-type structure) in 25 mol% lanthanide

¹ Adapted from reference 89, Li, L. *et al.* Ionic conductivity across the disorder–order phase transition in the NdO_{1.5}–CeO₂ system. *Solid State Ionics* **221**, 15-21, doi:10.1016/j.ssi.2012.06.007 (2012).

(Ln)-doped ceria (Ln=Sm, Gd, Dy, and Yb); these ordered domains were believed to be the cause of the degraded ionic conductivity.

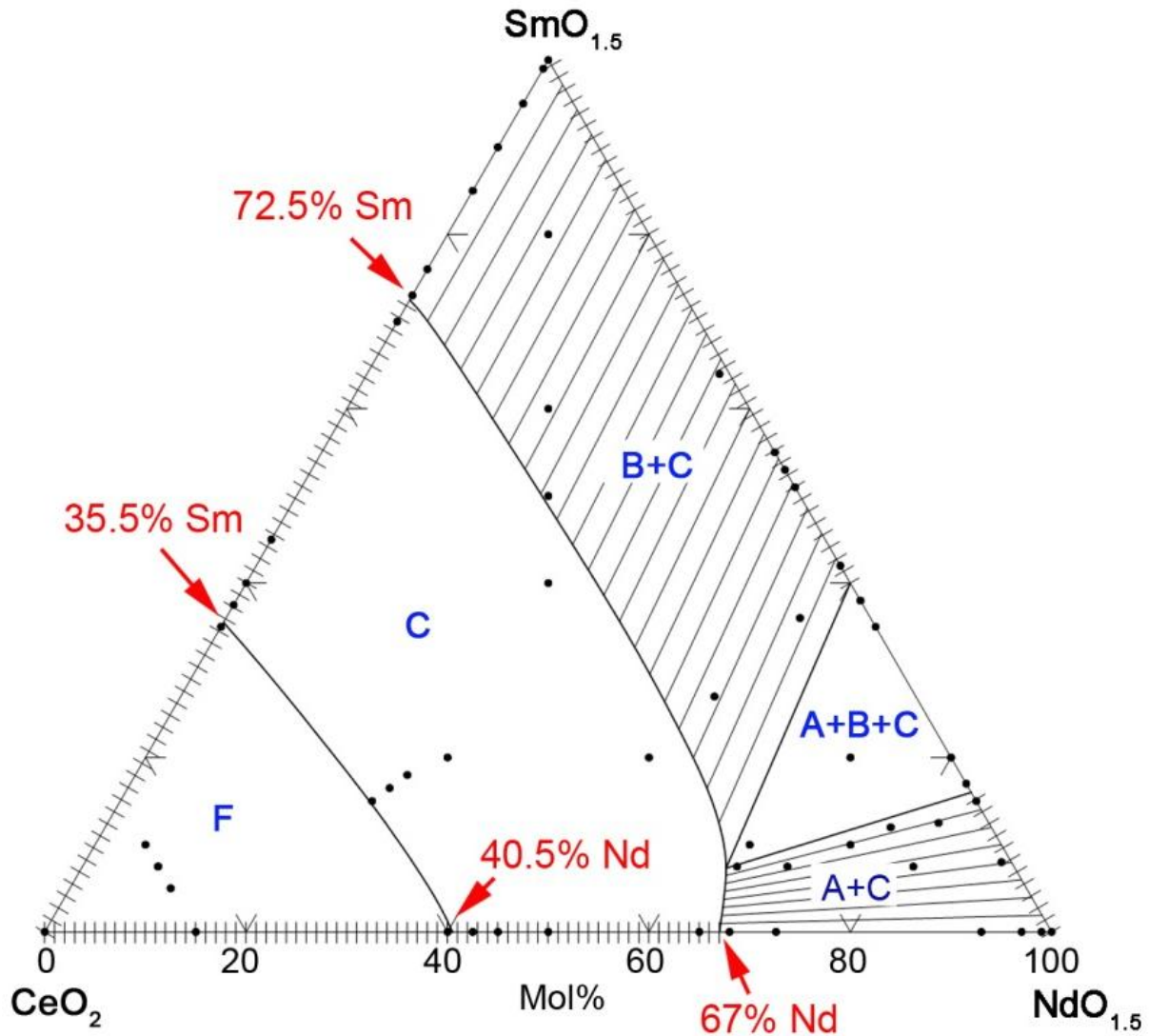


Figure 6-1. The ternary phase diagram of $\text{NdO}_{1.5}\text{-SmO}_{1.5}\text{-CeO}_2$ at room temperature reported by T. Vanderah⁹⁶. The dots on the graph represent experimental compositions examined by XRD; F indicates the region crystallizing with the fluorite structure; A, B, and C indicate the regions with A-, B-, and C-type rare-earth oxide structure, respectively.

While short-range ordering causes defect clustering and nanosized domains in the lattice, long-range ordering results in phase change of the bulk material. Pure ceria has a cubic fluorite structure and at certain Nd concentration the $\text{NdO}_{1.5}\text{-CeO}_2$ system

will stabilize into the C-type structure, as mentioned in section 2.2.1. Samples with different Nd content have been reported for the onset of C-type phase. For instance, Chavan *et al.*⁹⁷ found C-type phase started to show up at 52.5% Nd. Parks *et al.*⁹⁸ reported the first composition exhibiting weak C-type reflections to be 50% Nd and 40% Nd was said to show “very weak” C-type peaks. Quite recently, the phase equilibrium relations of the NdO_{1.5}-SmO_{1.5}-CeO₂ system were investigated by T. Vanderah⁹⁶ and the reported ternary phase diagram (redrawn for clarity) is presented in Figure 6-1. It is seen that the disorder-order transition happens at 40.5 mol% Nd and 35.5 mol% Sm concentrations along the NdO_{1.5}-CeO₂ and SmO_{1.5}-CeO₂ tie-lines, respectively.

The conductivity of neodymium doped ceria (NDC) has been studied by different groups.⁹⁹⁻¹⁰⁴ However, the conductivity of NdO_{1.5}-CeO₂ system and in particular the conductivity across the disorder-order phase transition has not been systematically examined. Furthermore, although heavy doping of ceria was believed to affect the conductivity adversely, in the work by Omar *et al.*²⁰ the grain conductivity of Sm³⁺ and Nd³⁺ co-doped ceria continued to increase up to 18% total dopant concentration. More recent work by Fu *et al.*¹⁰⁴ also showed that the total conductivity was still increasing at 25% NDC, posing the possibility of further conductivity enhancement upon increased Nd content.

In this work, the disorder-order phase transition of the NdO_{1.5}-CeO₂ system is examined by XRD and neutron diffraction at room temperature in order to elucidate the phase transition within the NdO_{1.5}-CeO₂ system. The ionic conductivity and the changes of pre-exponential factor and activation energy across the disorder-order

transition is evaluated in order to better understand the impact of oxygen-vacancy ordering on the ionic conductivity of ceria-based electrolytes.

6.2 Phase and Structural Analysis

6.2.1 X-ray Diffraction

The as-calcined powders were characterized by XRD and the results are shown in Figure 6-2 (a and b). In Figure 6-2 (a) it is shown that all XRD patterns of $0.05 \leq x \leq 0.45$ correspond to cubic fluorite structure, which is the same structure as pure ceria. It is thus confirmed that Nd was fully dissolved into ceria and solid solutions were formed. As more Nd was added, the peaks shifted to lower 2θ values due to the increased expansion of the host lattice, which resulted from the fact that the ionic radius of Nd is larger than that of Ce ($r_{\text{Ce}^{4+}} = 0.97 \text{ \AA}$ and $r_{\text{Nd}^{3+}} = 1.109 \text{ \AA}^{82}$). Figure 6-2 (b) shows the XRD profiles for $x = 0.50$ and 0.55 in addition to the theoretical pattern of the C-type structure for $\text{Nd}_{0.50}\text{Ce}_{0.50}\text{O}_{1.75}$. It is clear that the XRD profiles for $x = 0.50$ and 0.55 match the theoretical pattern. In order to identify the minor peaks of the C-type structure, the inset in Figure 6-2 (b) shows a close-up of the theoretical positions, the experimental XRD profiles for $x = 0.50$ and 0.55 , and the profiles for $x = 0.40$ and 0.45 for comparison. While for $x = 0.40$ and 0.45 no peaks can be identified, the reflections for $x = 0.50$ and 0.55 correspond well with the theoretical positions. According to Grover *et al.*¹⁰⁵, and as discussed in section 2.2.1, the XRD profile of C-type structure only differs from the fluorite in that the former has extra super-lattice peaks in addition to the reflections by the cubic structure and these extra super-lattice peaks are especially weak. Thus it is inferred that at about 50% Nd the compound crystallizes with the C-type structure.

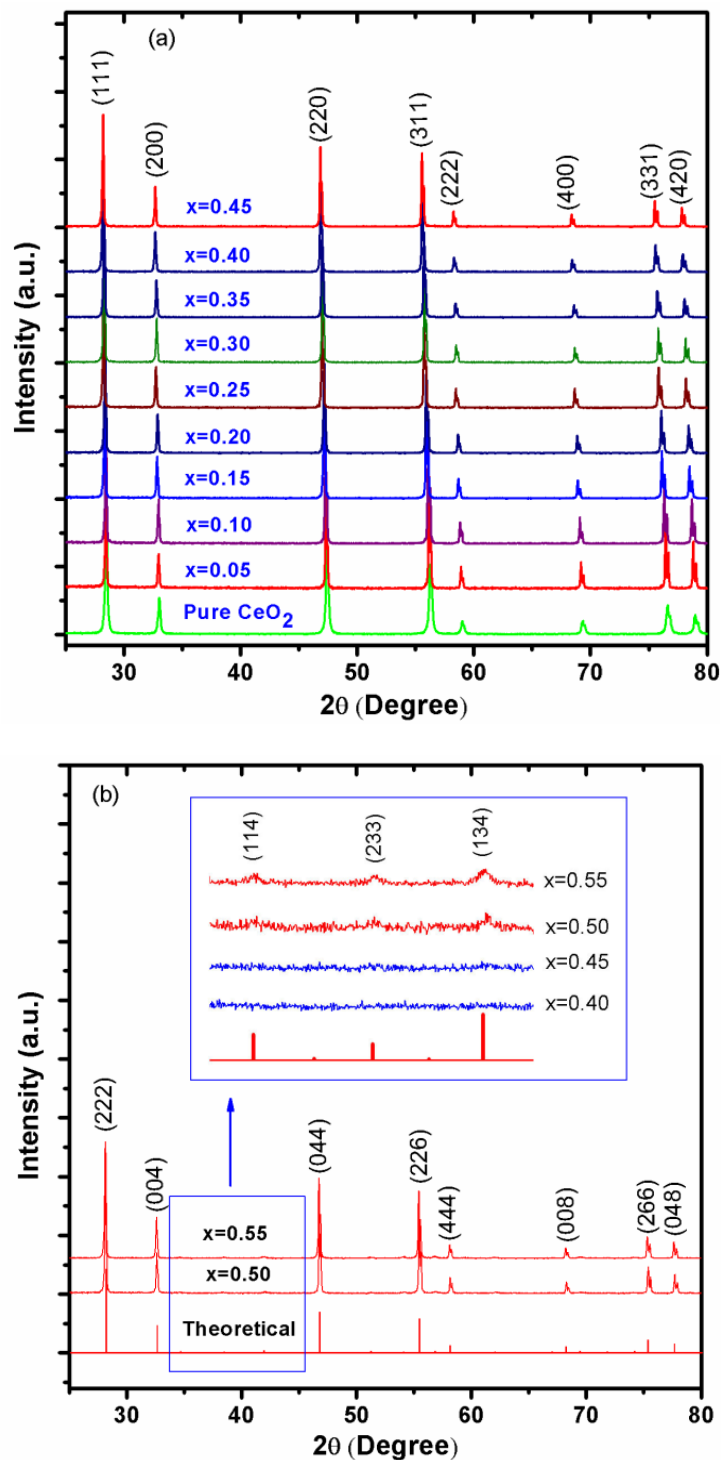


Figure 6-2. XRD patterns of the calcined powders of $\text{Nd}_x\text{Ce}_{1-x}\text{O}_{2-\delta}$ (a) ($0 \leq x \leq 0.45$) showing fluorite structure. (b) for $x = 0.50$ and 0.55 exhibiting C-type structure. The inset in (b) shows a close-up of the theoretical positions of the C-type structure, and the experimental patterns for $x = 0.40-0.55$.

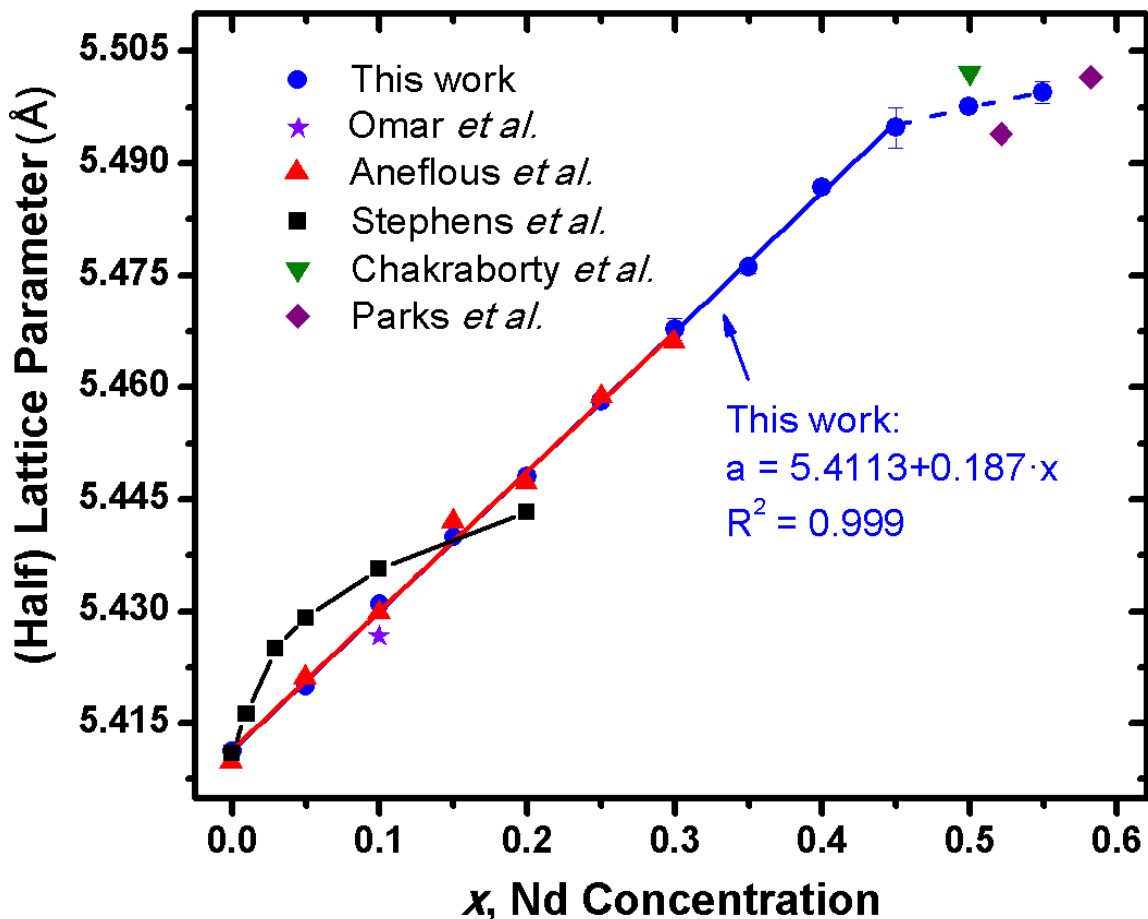


Figure 6-3. Lattice parameters of $\text{Nd}_x\text{Ce}_{1-x}\text{O}_{2-\delta}$ ($0 \leq x \leq 0.45$) as a function of Nd content; half lattice parameters are plotted for $x = 0.50$ and 0.55 , for which C-type structure is observed. The results reported by Omar *et al.*¹⁶, Aneflous *et al.*¹⁰³, Stephens *et al.*¹⁰², Chakraborty *et al.*¹⁰⁶, and Parks *et al.*⁹⁸ are added for comparison. Note the lattice parameters for $0 \leq x \leq 0.30$ in this work overlapped with those by Aneflous.

In order to quantify the lattice expansion, the cell parameters were calculated using the Nelson-Riley extrapolation method.⁵⁸ The results are presented as a function of Nd concentration in Figure 6-3, with lattice parameters reported in literature are also included for comparison. It should be noted that in Figure 6-3 half lattice parameters are plotted for $x = 0.50$ and 0.55 , after transition to C-type structure and doubling of the unit cell, as discussed in section 2.2.1. For $0.05 \leq x \leq 0.45$ the lattice parameters

increase linearly with increasing Nd content, following Vegard's law.⁸³ The fitted linear function can be expressed as

$$a = 5.4113 + 0.187x(0.05 \leq x \leq 0.45) \quad (6-1)$$

where x = Nd concentration, and a = lattice parameter (Å). The lattice constant determined in this work had excellent agreement with that of Aneflous *et al.*¹⁰³ On the other hand, the results by Stephens *et al.* could be fitted by a 2nd order polynomial equation and was explained as having attractive interactions among defects.¹⁰² The differences may be due to varying purity of starting materials: Chemicals used in this work and that of Aneflous *et al.* are 99.9% pure or above, while the purity for ceria nitrate in the work by Stephens *et al.* is only above 99%. Another factor that may have caused the disparity in lattice parameters is sample preparation. In this work solid state reactions are used, while Aneflous *et al.* and Stephens *et al.* used sol-gel and nitrate decomposition techniques, respectively.

A substantial deviation from the linear increase of lattice parameters is observed above 0.50. The contraction of the lattice may be attributed to the possibly enhanced defective interactions of C-type structure, which is already forming by $x = 0.50$ as evidenced by XRD.

6.2.2 Neutron Diffraction

Neutron diffraction was carried out on powders with compositions where $0.35 \leq x \leq 0.55$. The observed patterns for all samples tested are plotted in Figure 6-4. The calculated peak positions for fluorite and C-type structures are also shown at the bottom and the top of Figure 6-4. For samples with 35-45% Nd, the neutron diffraction profiles can be indexed with fluorite structure and no reflections of the C-type structure were

observed. C-type reflections began to appear in the sample containing 50% Nd, and these reflections became more prominent with 55% Nd. As an example for the fluorite structure, the observed, calculated, and difference neutron diffraction patterns of $\text{Nd}_{0.35}\text{Ce}_{0.65}\text{O}_{1.825}$ are presented in Figure 6-5. The calculated peak positions are also added as ticks in Figure 6-5. Figure 6-6 shows the obtained, calculated, and difference neutron diffraction profiles of $\text{Nd}_{0.55}\text{Ce}_{0.45}\text{O}_{1.725}$, having the C-type structure. The crystallographic structure reported by Chakraborty *et al.*¹⁰⁶ was used as the initial parameters for the Rietveld refinement of C-type structure. The background was modeled by function 1 (Shifted Chebyshev) with a sixth-order polynomial. Profile function 4 with Stephens asymmetry incorporated¹⁰⁷ was used to fit the diffraction peak profile. Subsequently, unit-cell parameter, atomic positions, isotropic displacement parameters, and site occupancies were refined. The refinement results for $\text{Nd}_{0.55}\text{Ce}_{0.45}\text{O}_{1.725}$ are listed in Table 6-1. The fitted lattice parameter (10.9980(3) Å) is quite close to what was calculated in Sec. 3.1 (10.998(3) Å).

Table 6-1. Detailed crystallographic information for $\text{Nd}_{0.55}\text{Ce}_{0.45}\text{O}_{1.725}$ obtained by Rietveld refinement.

Space Group: Ia-3						
Lattice parameter: a = 10.9980(3) Å						
Name	X	Y	Z	Ui/Ue*100	Multiplicity	Occupancy
Nd1	0.250000	0.250000	0.250000	1.50(8)	8	0.566(3)
Ce1	0.250000	0.250000	0.250000	1.50(8)	8	0.427(3)
Nd2	-0.0166(9)	0.000000	0.250000	1.30(5)	24	0.548(7)
Ce2	-0.0166(9)	0.000000	0.250000	1.30(5)	24	0.452(7)
O1	0.3828(7)	0.1374(5)	0.3786(4)	2.08(7)	48	0.89(1)
O2	0.3868(8)	0.3868(8)	0.3868(8)	4.6(1)	16	0.85(2)

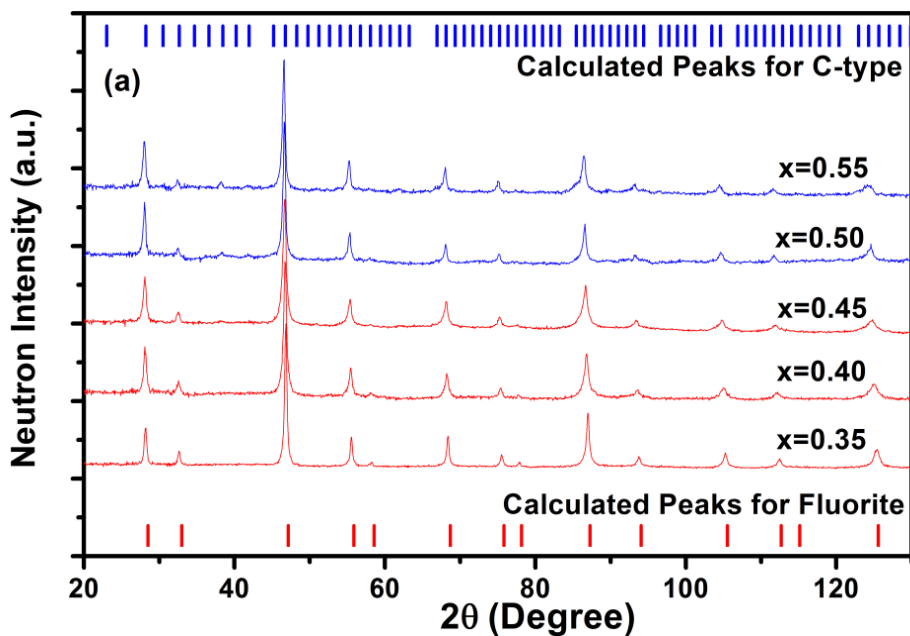


Figure 6-4. Observed neutron diffraction profiles for $0.35 \leq Nd \leq 0.55$. Calculated peak positions for fluorite and C-type structure are added as ticks at the bottom and top of the graph, respectively.

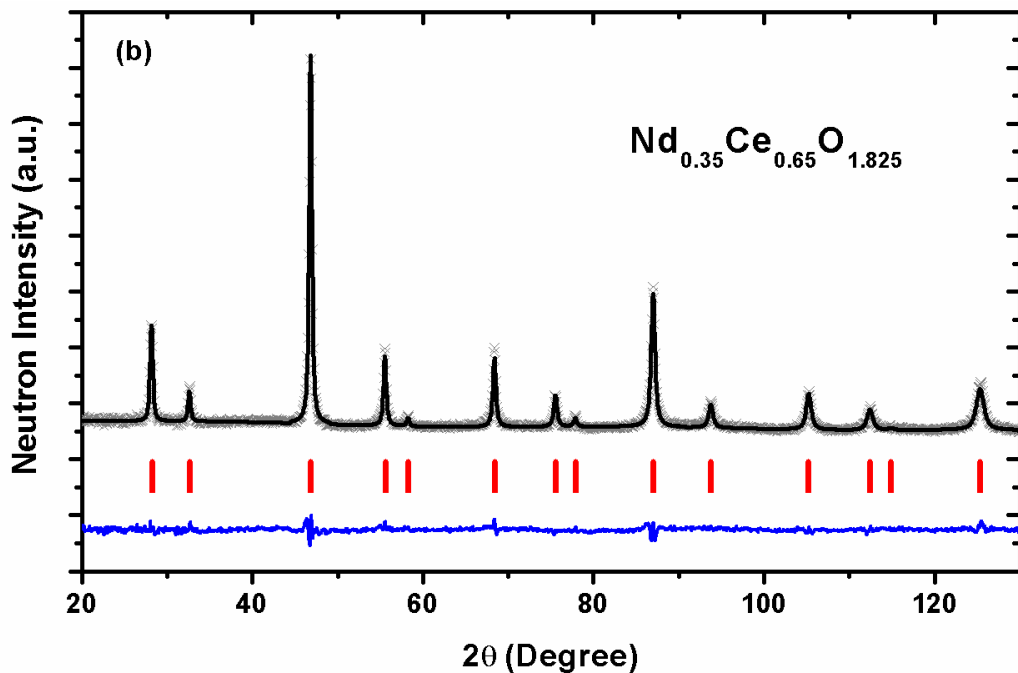


Figure 6-5. Observed (cross), calculated (continuous line), and difference neutron diffraction profiles for $Nd_{0.35}Ce_{0.65}O_{1.825}$ are shown.

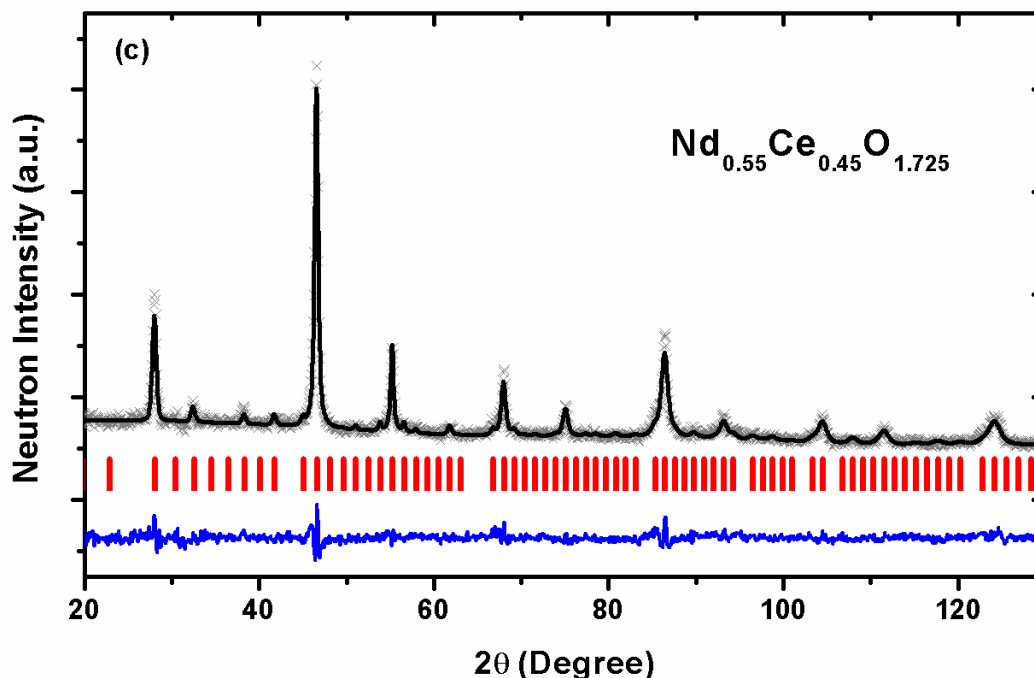


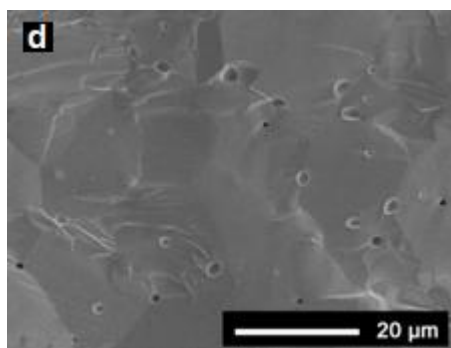
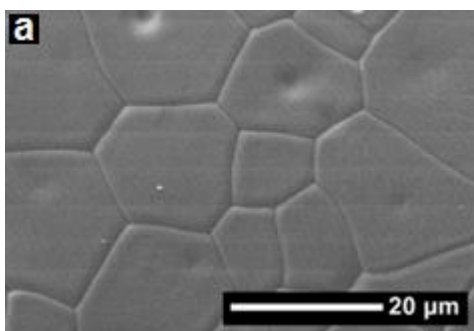
Figure 6-6. Observed (cross), calculated (continuous line), and difference neutron diffraction profiles for $\text{Nd}_{0.55}\text{Ce}_{0.45}\text{O}_{1.725}$ are shown.

While T. Vanderah⁹⁶ and Chavan *et al.*⁹⁷ found the composition that started to exhibit C-type structure had 40.5% and 52.5% Nd respectively, both neutron diffraction and XRD in this work indicates the formation of C-type structure happens at 50% Nd, which is also the value reported by Parks *et al.*⁹⁸, as noted earlier. Since the formation of C-type phase is kinetically controlled⁹⁷, the disparity may be due to different sample preparation, including synthesis method, heat treatment, etc., considering that T. Vanderah⁹⁶ used solid-state reactions and the samples were calcined at 1400°C for 40 h twice, followed by a third calcination at 1400°C for 64 h, with an intermediate grinding of samples between each heat treatment. Chavan *et al.*⁹⁷ also used solid-state reaction method with slow cooling (2°C/min) after heat treatment. In this work all samples were ball milled for 24 h, calcined at 1450°C for 10 h and cooled down at ~3°C/min. Parks *et*

a.⁹⁸ prepared samples by co-precipitation technique and various heat treatments were used, followed by air quenching.

6.3 Microstructural Analysis

The microstructure of the sintered pellets was characterized by SEM and micrographs for $x = 0.05, 0.15$ and 0.25 are presented in Figure 6-7, where (a-c) are thermally-etched surfaces and (d-f) represent cross sections. It can be seen that the pellets are well-densified, which is in accordance with the measured high relative densities. The individual grains on the cross-section SEM micrographs are barely visible. Grain sizes are calculated by Heyn's method^{108,109} using thermally etched large SEM images and the results are listed in Table 6-2. In the current study the Nd concentration doesn't have a marked impact on grain size, which is in agreement with observations reported by Fu and Chen¹⁰⁴, who sintered samples of $\text{Nd}_x\text{Ce}_{1-x}\text{O}_{2-\delta}$ ($0.05 \leq x \leq 0.25$) at 1500°C for 5h and reported grain size in the range of 3.45 to $7.54 \mu\text{m}$. For other lanthanide-doped ceria systems, both increases¹³ and decreases¹¹⁰ in grain size with an increase in trivalent ions have been reported. However, the grain ionic conductivity is expected to be independent of grain size in bulk samples since it is an intrinsic property of the material.



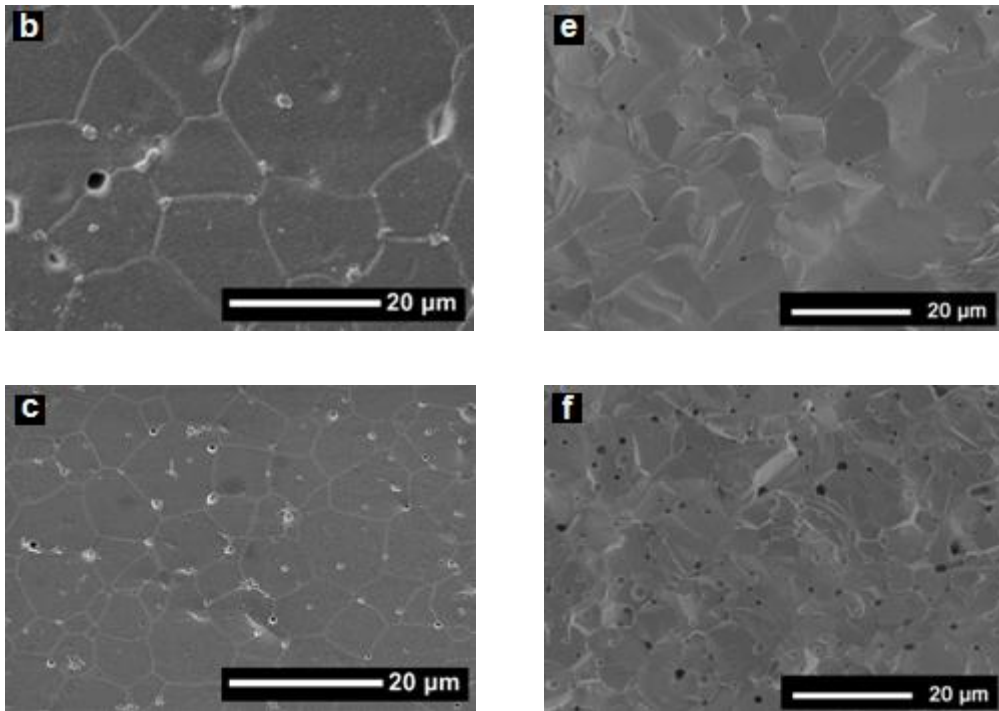


Figure 6-7. SEM micrograph for sintered pellets of $\text{Nd}_x\text{Ce}_{1-x}\text{O}_{2.5}$: a, d) $x = 0.05$; b, e) $x = 0.15$; and c, f) $x = 0.25$. The images on the left-hand side are for thermally etched surfaces, while the images on the right-hand side represent fractured cross sections.

Table 6-2. Grain sizes of the sintered pellets of different compositions.

Composition	Grain size (μm)
$\text{Nd}_{0.05}\text{Ce}_{0.95}\text{O}_{1.975}$	12.3(0.4)
$\text{Nd}_{0.15}\text{Ce}_{0.85}\text{O}_{1.925}$	14.0(0.7)
$\text{Nd}_{0.25}\text{Ce}_{0.75}\text{O}_{1.875}$	5.7(0.1)

6.4 Ionic Conductivity

The grain ionic conductivity was measured from 250-700°C in air and the Nyquist plot of impedance for $\text{Nd}_{0.25}\text{Ce}_{0.75}\text{O}_{1.875}$ (at 250°C) is shown in Figure 6-8. Two well-defined semi-circles, representing the grain and grain boundary resistances respectively, can be easily identified. Electronic conduction in the materials was assumed to be negligible since it has been shown the reduction of Ce^{4+} to Ce^{3+}

happens only at reducing atmospheres and high temperatures ($\sim 1000^\circ\text{C}$)^{111,112}. Figure 6-9 shows the Arrhenius plot and it is seen that the conductivity follows Arrhenius-type behavior. The straight lines in Figure 6-9 are the least-square linear fitting results and the adjusted coefficients of determination (R^2_{adj}) are above 0.999 for all linear fittings. Although Arrhenius plots are sometimes fit using two straight lines (i.e., one line for high temperature region and the other for low temperature), minimum deviation from linearity in the whole temperature range was observed in this work. Therefore fits using only one straight line per composition were performed. Similar practices have recently been reported for the $\text{NdO}_{1.5}\text{-CeO}_2$ system¹⁰⁴, as well as for the $\text{SmO}_{1.5}\text{-CeO}_2$ ¹¹³ and $\text{GdO}_{1.5}\text{-CeO}_2$ ¹¹⁴ systems. The isothermal plot of ionic conductivity as a function of Nd content at temperatures between $450\text{-}700^\circ\text{C}$ is shown in Figure 6-8. The maximum conductivity is found to be $0.054(1) \text{ S}\cdot\text{cm}^{-1}$ exhibited by $\text{Nd}_{0.15}\text{Ce}_{0.85}\text{O}_{1.925}$ at 700°C with an associated activation energy of $0.726(5) \text{ eV}$. In Figure 6-10 the grain conductivity reported by Stephens *et al.*¹⁰² and Omar *et al.*²⁰ is also added for comparison. It is observed that at a fixed temperature, as the Nd content increases, the conductivity first increased and reached its maximum values at 10% or 15% Nd content (depending on the temperature), then starts to decrease steadily. The initial increase in conductivity is attributed to the increase of charge carriers (oxygen vacancies) into the host lattice. However, as more Nd is added the fraction of trivalent ion-oxygen vacancy associates increases leading to the immobilization of these oxygen vacancies. Therefore the decrease in conductivity is seen at higher Nd regions in Figure 6-9. In contrast to this work, Fu *et al.*¹⁰⁴ found that $\text{Nd}_{0.25}\text{Ce}_{0.75}\text{O}_{1.875}$ delivered the highest total conductivity among all compositions tested. It should be stressed that grain conductivity is

examined in this work while Fu *et al.* evaluated total conductivity (sum of grain and grain boundary conductivity). Consequently the different trend observed is explained by the fact that grain conductivity is a fundamental material property while microstructure and impurity, in addition to chemical formation, affect grain boundary conductivity as well.²⁰

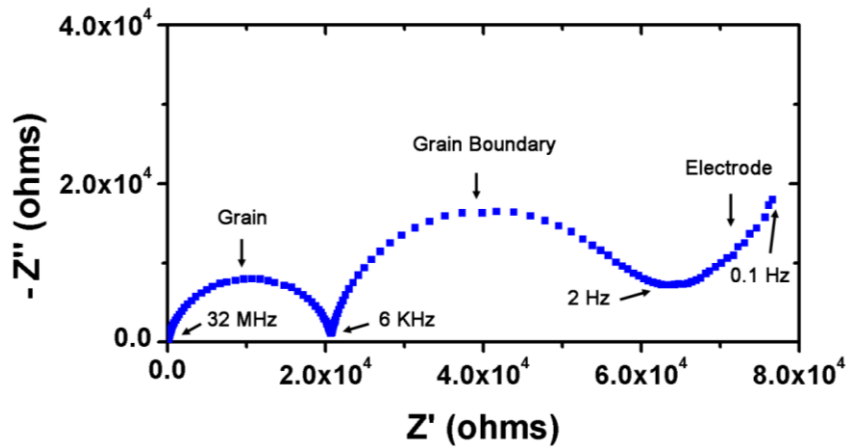


Figure 6-8. Nyquist plot of impedance for $\text{Nd}_{0.25}\text{Ce}_{0.75}\text{O}_{1.875}$, measured at 250°C in air.

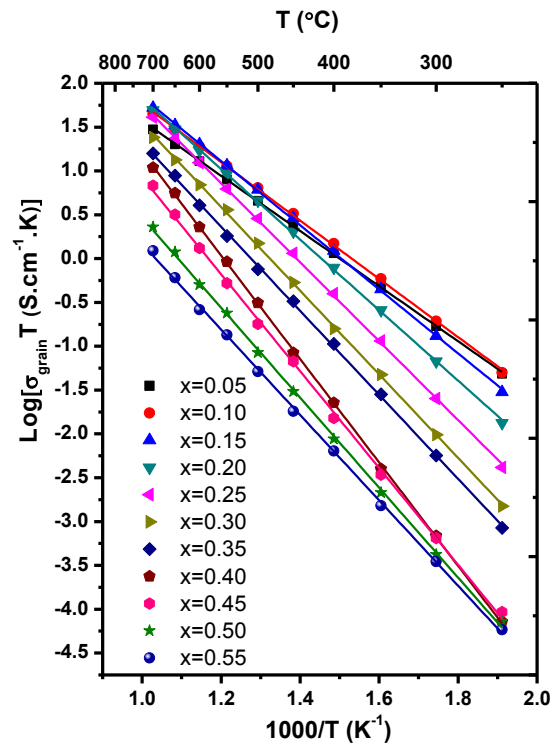


Figure 6-9. Arrhenius plot of grain conductivity of $\text{Nd}_x\text{Ce}_{1-x}\text{O}_{2-\delta}$ ($0 \leq x \leq 0.55$).

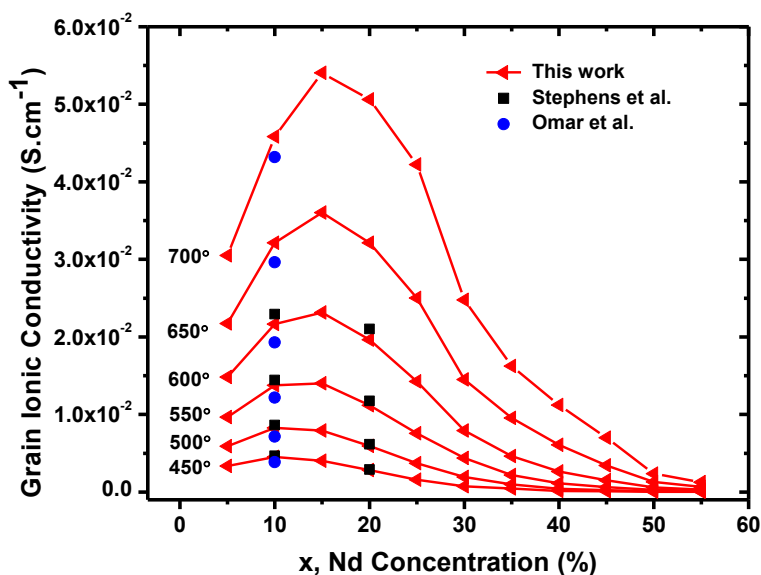


Figure 6-10. Grain conductivity of $\text{Nd}_x\text{Ce}_{1-x}\text{O}_{2-\delta}$ ($0 \leq x \leq 0.55$) as a function of Nd concentration (x) at temperatures from 450-700°C. The results reported by Stephens *et al.*¹⁰² and Omar *et al.*²⁰ are added for comparison.

It is worthwhile to mention that across the expected disorder-order transition region (either 40.5% or 50%), no drastic change of conductivity is observed, which is in direct contrast to phase transition of Bi_2O_3 . Harwig *et al.*¹¹⁵ found the conductivity increased 3 orders of magnitude upon the transition from α - Bi_2O_3 to δ - Bi_2O_3 at 729°C. δ - Bi_2O_3 , which has fluorite-type structure with a quarter of the oxygen anion sublattice unoccupied, has the highest oxide-ion conductivity among all known fluorite based oxides¹¹⁶ ($\sim 1 \text{ S}\cdot\text{cm}^{-1}$ above 730°C¹¹⁵), which is ascribed to highly disordered state and high mobility of anion vacancies.¹¹⁵

To further understand the observed change in grain conductivity across the phase transition, A_0 and E_A for different Nd concentrations were calculated from the ordinate intercept and the slope of the fitted lines in Figure 6-9, respectively. The results are shown in Figure 6-9, where the shortest cation-anion distance is also presented. It should be noted that in Figure 6-9 $\log(A_0)$ is used as one of the vertical

axes instead of A_0 . It is seen both $\log(A_0)$ and E_A exhibit similar trend: they first increased with increasing Nd concentration and then started to drop above 40% Nd. Most notably, when Nd content went from 35% to 40%, both $\log(A_0)$ and E_A experienced drastic increases, which can be attributed to the disorder-order transition that happened at around 40% Nd, which is the composition reported by Bevan¹¹⁷ that started to exhibit C-type peaks. Although both XRD and neutron diffraction established earlier that $\text{Nd}_{0.50}\text{Ce}_{0.50}\text{O}_{1.75}$ is the first composition to have C-type reflection at room temperature, all impedance measurements were carried out at 250°C or above; therefore it is likely that at higher temperatures the disorder-order transition in the $\text{NdO}_{1.5}\text{-CeO}_2$ system may be shifted to lower Nd content. Such shift in the $\text{NdO}_{1.5}\text{-CeO}_2$ system was also reported by others.⁹⁷

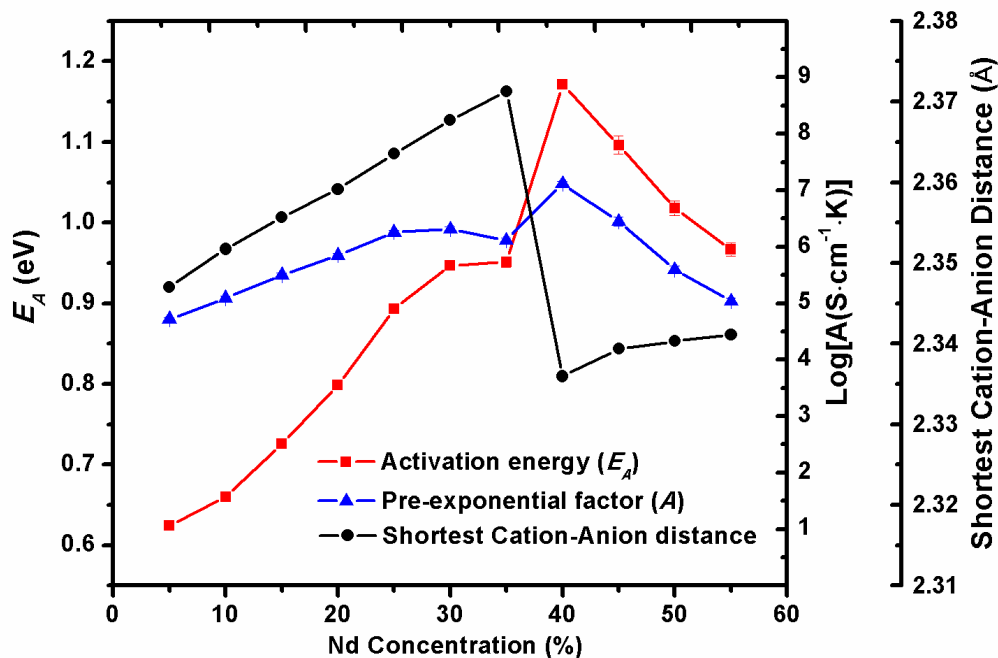


Figure 6-11. Activation energy (E_A), pre-exponential factor (A_0), and shortest cation-anion distance as a function of Nd content.

In Figure 6-11, $\log(A_0)$ increases from 6.11(4) to 7.12(4) between 35% and 40% Nd, indicating an order of magnitude change for A_0 . This large increase is consistent with the change in the local crystallographic environment (such as coordination number, bond distance, and change in concentration of vacancies due to emergence of vacant crystallographic sites [in the ordered structure]) for the anion when transitioning from fluorite to C-type structure. Possible sources for the increase of A_0 include the change of mobile oxygen-vacancy fraction $[V_O^{**}]$ and configurational entropy (part of ΔS) due to the ordering of oxygen vacancies in C-type structure.

During the phase transition E_A shows a marked increase as seen in Figure 6-11. The observed increase is due to the stabilization of oxygen vacancies in C-type structure. These stabilized oxygen vacancies are likely to have higher binding energies¹¹⁸ and form deep traps, which prevent oxygen migration.⁹³ It is also shown in Figure 6-11 the increase of E_A is accompanied by the decrease of the shortest cation-anion distance, which may contribute to higher E_A since stronger columbic attraction can be expected when the cation and anion come closer. It is not surprising to observe the marked increase of E_A during the phase transition of the bulk material, given that E_A is already seen to increase greatly when the size of the micro C-type domain became larger in $YO_{1.5}$ - CeO_2 system.¹¹⁹

Although both A_0 and E_A vary noticeably across the disorder-order transition, as seen in Figure 6-10, they seem to counteract each other resulting in an overall gradual decrease in conductivity. In Figure 6-9, at low temperatures the gap between $x = 0.35$ and 0.40 is clearly larger than those between the other concentrations, indicating greater changes in conductivity during the phase transition. However, given the small

conductivity values at 450°C these changes are not readily noticeable in Figure 6-10. For NdO_{1.5}-CeO₂ system the optimal conductivities in the intermediate temperature range are achieved with materials containing 10 to 15% of Nd.

6.5 Conclusions

Samples of Nd_xCe_{1-x}O_{2-δ} (0 ≤ x ≤ 0.55) were prepared by conventional solid-state reactions and the grain conductivity for all samples was evaluated. The lattice parameters for 0 ≤ x ≤ 0.45 increased linearly with increasing Nd content, complying with Vegard's law. Both XRD and neutron diffraction suggested that the first composition that exhibited C-type reflections at room temperature was Nd_{0.50}Ce_{0.50}O_{1.75}. Although both the pre-exponential factor (A_0) and activation energy (E_A) increased noticeably when Nd content went from 35% to 40%, they counteracted each other and the overall effect is that the conductivity declined gradually. The disorder-order transition during the impedance measurements was shown to happen at around 40% Nd concentration, deviating from the XRD and neutron diffraction results due to different testing conditions. No unusual change of conductivity was observed either around 40.5% or 50% Nd, which are the possible disorder-order transition compositions reported in literature. The maximum conductivity of 0.054(1) S·cm⁻¹ was exhibited by Nd_{0.15}Ce_{0.85}O_{1.925} at 700°C and the associated activation energy was 0.726(5) eV.

CHAPTER 7 SUMMARY AND FUTURE WORK

7.1 Summary

The development of materials with higher ionic conductivity in the intermediate temperature range is necessary for the advancement of IT-SOFC technology. The work reported in this thesis investigates size and compositional effects on ionic conductivity in doped ceria. Highly oriented doped ceria thin films were deposited on Pt bottom electrodes for the first time and the first across-plane ionic conductivity measurements of these films were performed. DC sputtering was used to deposit a highly oriented layer of Pt (111) on *a*-plane sapphire substrates. The highly oriented doped ceria layer was then deposited using pulsed laser deposition. Such thin film samples allow for the first time the direct measurement of grain ionic conductivity of doped ceria since there is no grain boundary contribution to the across-plane conductivity measurements. Ionic conductivity data indicates inconsistencies in literature may simply be a result of the different experimental conditions used in each study.

Prior to this work, co-doping using Sm^{+3} and Nd^{+3} has demonstrated only intermediate values between those of the respective singly doped materials with Nd-doped ceria exhibiting the highest conductivity. This work investigated the $\text{Sm}_x\text{Nd}_y\text{Ce}_{0.9}\text{O}_{2-\delta}$ system and found that non 1:1 co-doping does not result in higher conductivity values than singly doped or evenly co-doped materials but rather follows the theory of effective index. Since co-dopant ratio (x/y) variations within the $\text{Sm}_x\text{Nd}_y\text{Ce}_{0.9}\text{O}_{2-\delta}$ system do not lead to significant conductivity changes it constitutes a versatile system impervious to potential performance degradation due to preferential dopant segregation and redistribution.

Samples of $\text{Nd}_x\text{Ce}_{1-x}\text{O}_{2-\delta}$ ($0 \leq x \leq 0.55$) were prepared by conventional solid-state reactions and the grain conductivity for all samples was evaluated. The lattice parameters for $0 \leq x \leq 0.45$ increased linearly with increasing Nd content, complying with Vegard's law. Both XRD and neutron diffraction suggested that the first composition that exhibited C-type reflections at room temperature was $\text{Nd}_{0.50}\text{Ce}_{0.50}\text{O}_{1.75}$. Although both the pre-exponential factor (A_0) and activation energy (E_A) increased noticeably when Nd content went from 35% to 40%, they counteracted each other and the overall effect is that the conductivity declined gradually. The disorder-order transition during the impedance measurements was shown to happen at around 40% Nd concentration, deviating from the XRD and neutron diffraction results due to different testing conditions. No unusual change of conductivity was observed around either possible disorder-order transition compositions reported in literature, 40.5% or 50% Nd. The maximum conductivity of $0.054(1) \text{ S}\cdot\text{cm}^{-1}$ was exhibited by $\text{Nd}_{0.15}\text{Ce}_{0.85}\text{O}_{1.925}$ at 700°C and the associated activation energy was $0.726(5) \text{ eV}$.

7.2 Future Work

7.2.1 Thin Films

Investigating the across-plane ionic conductivity of highly oriented ceria thin films over a wider range of dopants, thicknesses, and temperatures is necessary to better understand the behavior in these promising electrolyte materials. Finding ways to deposit higher quality films could provide the ability to measure thinner films, perhaps accomplished using atomic layer deposition. Measuring films as thin as 4-10 nm, the typical size of the space charge layer (SCL) in doped ceria materials being 2-5 nm³⁶,

would allow for the direct observation of the effect of SCL interactions on grain ionic conductivity.

Developing a better setup for the measurement of ionic conductivity of thin films, particularly focusing on sample heating and atmospheric control would also be helpful. The ability to heat the sample up to 800°C under various oxygen partial pressures while ensuring the film does not move (potentially using vacuum to secure the film) would provide data that could more easily be compared to typical bulk data while increasing reproducibility. Measuring conductivity of the films as a function of oxygen partial pressure could confirm that the conductivity is ionic.

It would also be interesting to use atom probe analysis to investigate the segregation of various species to surfaces and interfaces in thin film samples to determine whether or not this segregation is similar to what is observed in bulk samples. This would also be useful in determining if segregation is affected by film thickness, and thus grain size.

7.2.2 Bulk

The primary focus of this thesis was on enhancing the grain ionic conductivity of doped ceria. However, the presence of grain boundaries in bulk ceria limits the total ionic conductivity and is thus also very important. Additional work relating various doping strategies to the grain boundary and total ionic conductivity is need for a complete understanding.

It has been demonstrated that when bulk samples are synthesized using coprecipitated nanopowder and microwave sintering, grain boundary impedance is reduced.¹²⁰ However, due to the smaller grain size, the grain boundary density is

significantly higher thus the total ionic conductivity is lower since the grain boundaries are still blocking. Synthesizing samples using micron-sized coprecipitated powder and microwave sintering could produce bulk material with both low grain boundary impedance and grain boundary density resulting in a higher total ionic conductivity.

APPENDIX A
NDC FILMS ON VARIOUS SUBSTRATES

Highly oriented thin films of NDC were successfully deposited on platinized substrates, as reported above, but there were many prior unsuccessful attempts. The parameters which were varied include substrate material and substrate orientation.

The simplest approach involved using platinized silicon substrates since they could be used as purchased without the need to deposit a Pt layer. However, the resulting films were polycrystalline as evidenced by the appearance of additional peaks in the XRD pattern, as seen in Figure A-1 below. This is attributed to the fact that the Pt layer on the platinized silicon substrates was also not preferentially oriented.

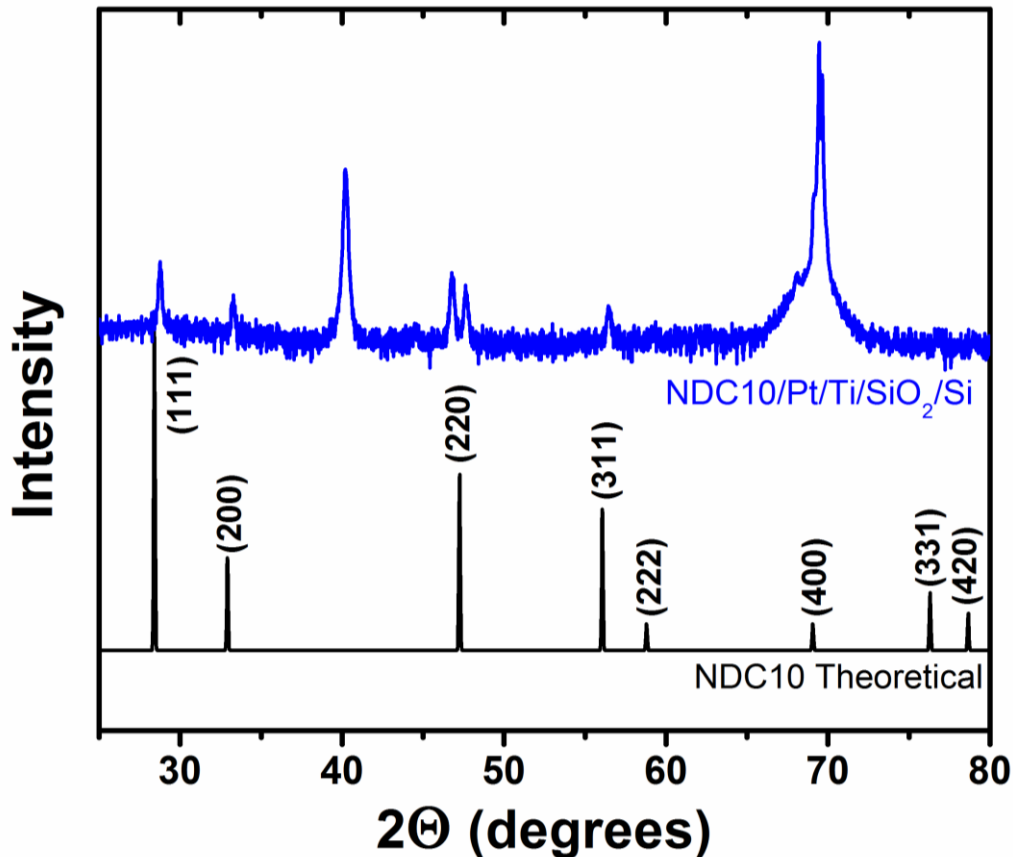


Figure A-1. XRD pattern of a polycrystalline NDC film deposited on a platinized silicon substrate using PLD. The unlabeled peaks are attributed to Si and Pt layers.

In order to deposit an highly oriented film of NDC, it was determined that it is necessary to start with a highly oriented layer of Pt. The first attempt used RF sputtering to deposit Pt on *c*-plane (0001) sapphire substrates. However, the equipment used was not capable of matching the temperature and pressure conditions stated by Bachelet *et al.*¹²¹ and the Pt layer was polycrystalline, as seen in Figure A-2 below.

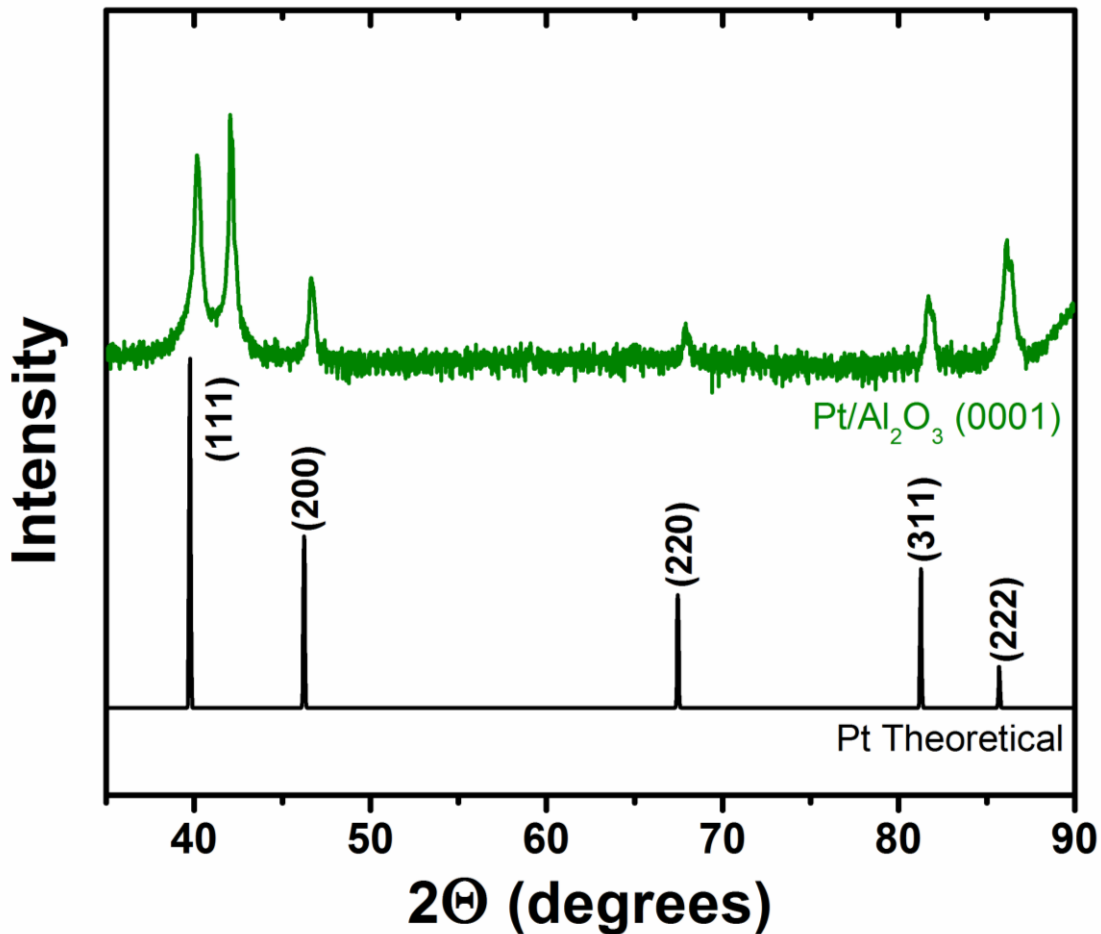


Figure A-2. XRD pattern of a polycrystalline Pt layer deposited on a *c*-plane (0001) sapphire substrate using DC sputtering.

The next attempt used DC sputtering to deposit Pt on *a*-plane (11-20) sapphire substrates following Nefedov *et al.*⁵⁷ The absence of the (200) and (220) peaks in Figure A-3 below indicate that the Pt layer is highly oriented. Films deposited on these

platinized substrates were highly oriented confirming that a highly oriented Pt layer is a necessary condition for the deposition of highly oriented NDC films.

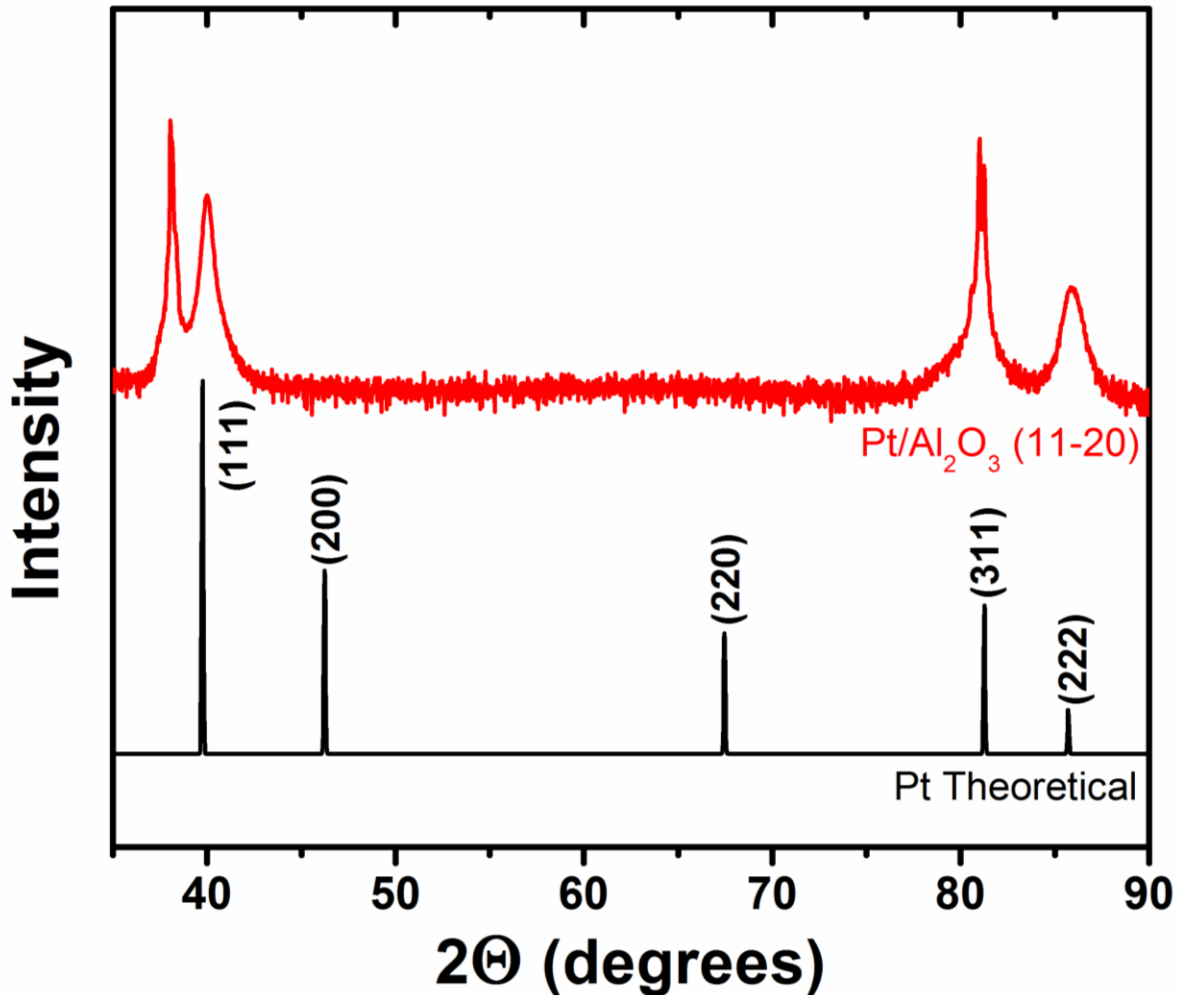


Figure A-3. XRD pattern of a highly oriented Pt layer deposited on an *a*-plane sapphire substrate using DC sputtering. *The peak around 81° is the (220) peak attributed to the substrate.

These films are highly oriented but not epitaxial. The high degree of orientation is confirmed by the omega scan seen in Figure A-4. The full width at half max (FWHM) is below one degree, indicating a high level of orientation. However, the pole figure seen in Figure A-5 exhibits a ring of intensity and not discrete spots, indicating the film is not epitaxial.

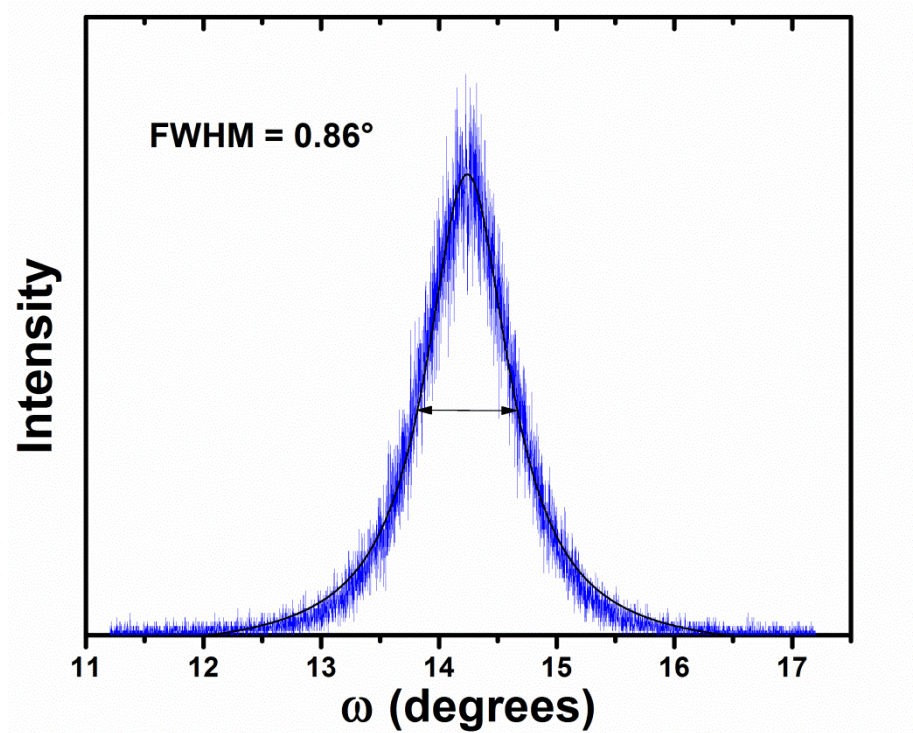


Figure A-4. Omega scan of a highly oriented NDC film with a FWHM = 0.86°.

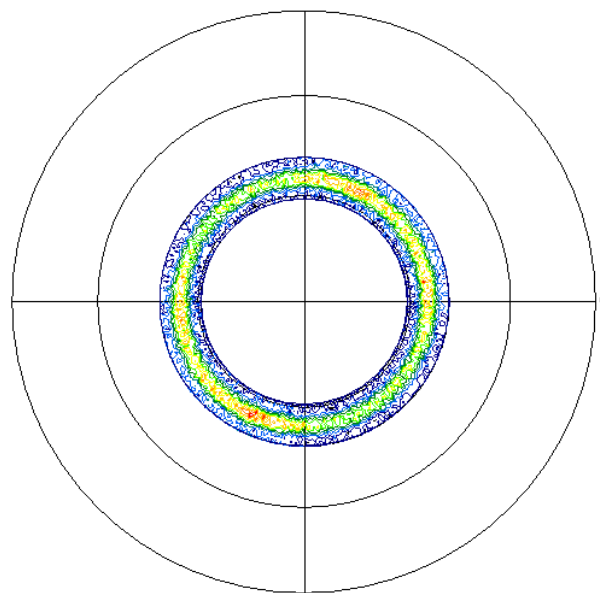


Figure A-5. The pole figure of an NDC film exhibits a ring of intensity indicating the film is not epitaxial. The pole was the [022] direction and the scan covered chi angles 29-41°.

APPENDIX B FITTING IMPEDANCE DATA USING ZVIEW

Fitting impedance data using equivalent circuit analysis is made quite simple by the use of ZView software. Once the data file is opened in ZView, the range of data points which is to be fit is selected and initial guesses are made for circuit components; only data points for the first two arcs (grain and grain boundary) are fit. To minimize the error of the fit, it may be necessary to fix certain parameters for initial fitting runs, which can be done by clicking the \pm button until it changes to an X. For example, fixing the values of L1, R1, and R2 can help better fit the values of CPE1-T and CPE2-T. Once this is complete, changing all values back to \pm and running another fit usually produces lower error. An example for an $\text{Nd}_{0.1}\text{Ce}_{0.9}\text{O}_{2-\delta}$ sample at 250°C is seen in Figure B-1.

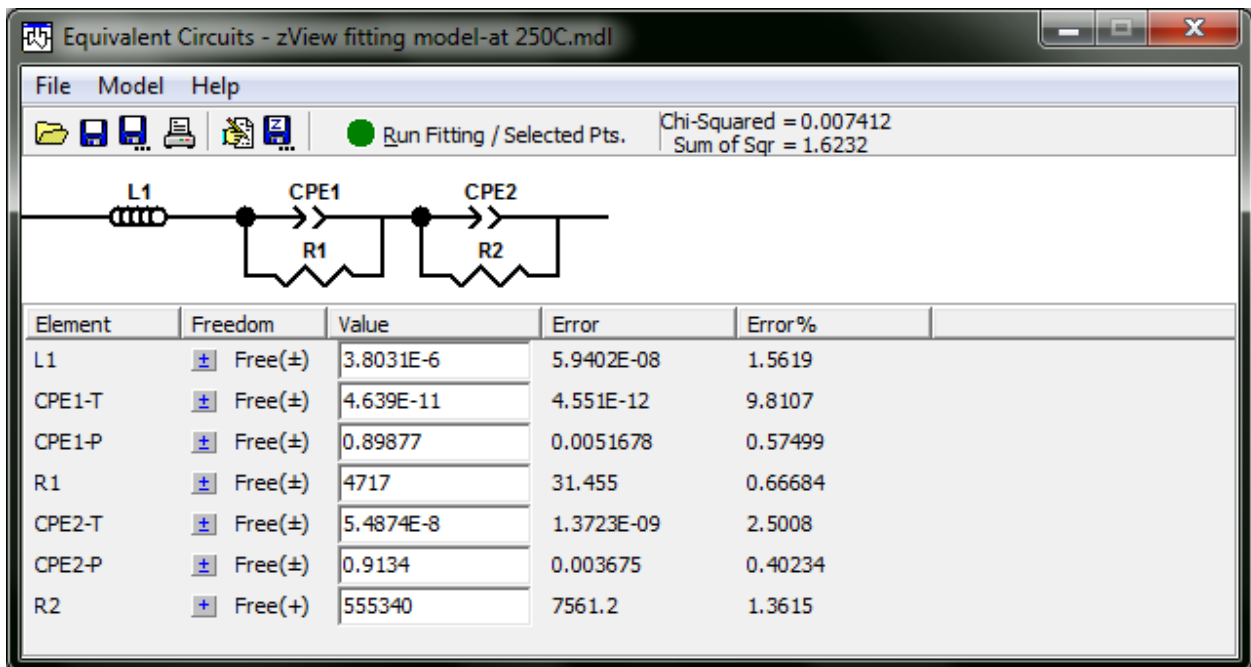


Figure B-1. Equivalent circuit fitting window in ZView.

The values of R1 and R2 correspond to the diameters of the semicircular arcs associated with grain and grain boundary impedance. Values for CPE1-T are typically

on the order of 10^{-11} - 10^{-13} while values for CPE2-T are typically on the order of 10^{-6} - 10^{-8} depending on composition and temperature. CPE1-P and CPE2-P are typically between 0.8-1.1. L1, which is a measure of the inductance of the experimental setup, is usually around 10^{-6} - 10^{-8} . Figure B-2 shows the result of the equivalent circuit fit whose component values are presented in Figure B-1.

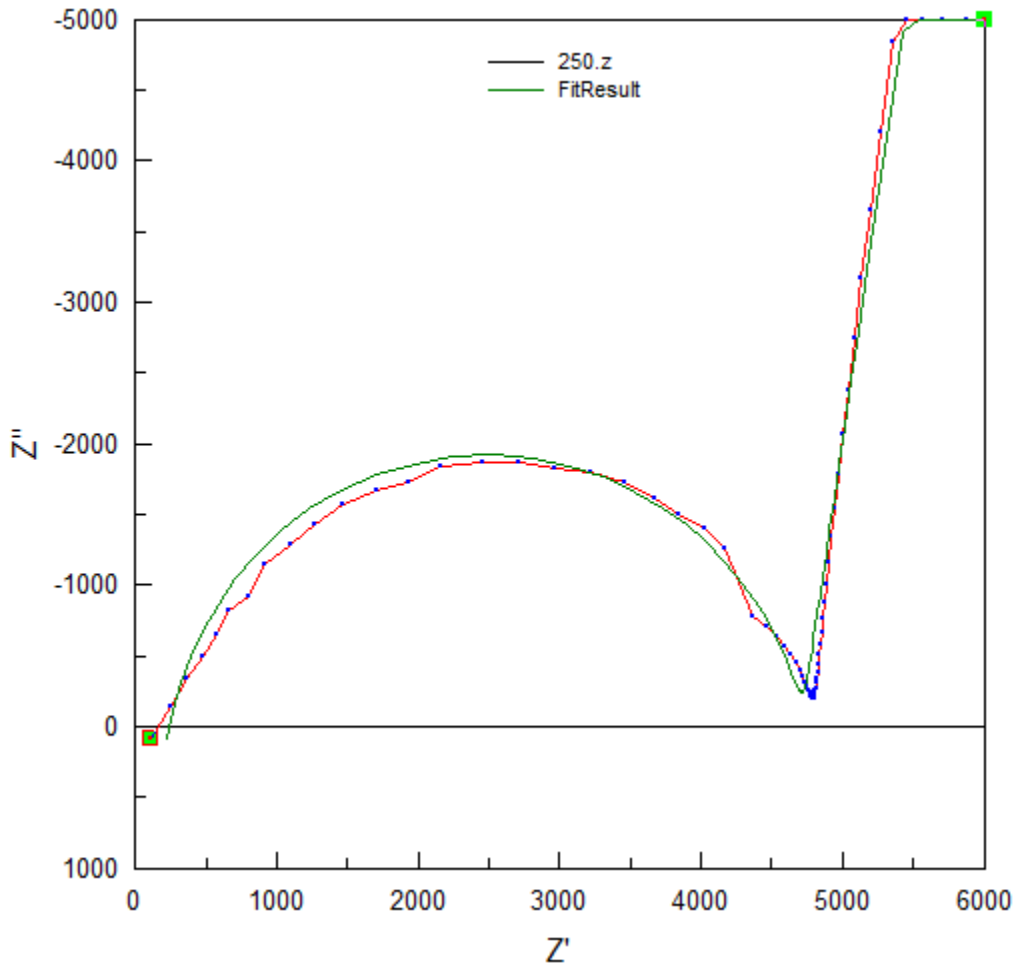


Figure B-2. Fit resulting from equivalent circuit analysis performed using ZView.

LIST OF REFERENCES

- 1 Steele, B. C. H. Material science and engineering: The enabling technology for the commercialisation of fuel cell systems. *Journal of Materials Science* **36**, 1053-1068 (2001).
- 2 Wachsman, E. D. & Lee, K. T. Lowering the Temperature of Solid Oxide Fuel Cells. *Science* **334**, 935-939, doi:10.1126/science.1204090 (2011).
- 3 Boivin, J. C. & Mairesse, G. Recent material developments in fast oxide ion conductors. *Chemistry of Materials* **10**, 2870-2888 (1998).
- 4 Laboratory, N. E. T. <<http://www.netl.doe.gov/technologies/coalpower/fuelcells/seca/primer/cell.html>>
- 5 Phadke, S. R. & Nino, J. C. Conductivity Enhancement in Lanthanum Phosphates. *Journal of the American Ceramic Society* **94**, 1817-1823 (2011).
- 6 Jacobson, A. J. Materials for Solid Oxide Fuel Cells†. *Chemistry of Materials* **22**, 660-674, doi:10.1021/cm902640j (2009).
- 7 Tarancón, A. Strategies for Lowering Solid Oxide Fuel Cells Operating Temperature. *Energies* **2**, 1130-1150 (2009).
- 8 Steele, B. C. H. Materials for IT-SOFC stacks: 35 years R&D: the inevitability of gradualness? *Solid State Ionics* **134**, 3-20, doi:10.1016/s0167-2738(00)00709-8 (2000).
- 9 Inaba, H. & Tagawa, H. Ceria-based solid electrolytes - Review. *Solid State Ionics* **83**, 1-16 (1996).
- 10 Kharton, V. V., Marques, F. M. B. & Atkinson, A. Transport properties of solid oxide electrolyte ceramics: a brief review. *Solid State Ionics* **174**, 135-149, doi:<http://dx.doi.org/10.1016/j.ssi.2004.06.015> (2004).
- 11 Andersson, D. A., Simak, S. I., Skorodumova, N. V., Abrikosov, I. A. & Johansson, B. Optimization of ionic conductivity in doped ceria. *Proceedings of the National Academy of Sciences of the United States of America* **103**, 3518-3521 (2006).
- 12 Fuda, K., Kishio, K., Yamauchi, S., Fueki, K. & Onoda, Y. O-17 Nmr-Study of Y₂o₃-Doped Ceo₂. *J. Phys. Chem. Solids* **45**, 1253-1257 (1984).
- 13 Kuharungrong, S. Ionic conductivity of Sm, Gd, Dy and Er-doped ceria. *Journal of Power Sources* **171**, 506-510 (2007).

- 14 Li, F. *et al.* Laser-assisted three-dimensional atom probe analysis of dopant distribution in Gd-doped CeO₂. *Scr. Mater.* **63**, 332-335 (2010).
- 15 Li, F., Ohkubo, T., Chen, Y. M., Kodzuka, M. & Hono, K. Quantitative atom probe analyses of rare-earth-doped ceria by femtosecond pulsed laser. *Ultramicroscopy* **111**, 589-594, doi:10.1016/j.ultramic.2010.12.011 (2011).
- 16 Omar, S., Wachsman, E. D., Jones, J. L. & Nino, J. C. Crystal Structure-Ionic Conductivity Relationships in Doped Ceria Systems. *Journal of the American Ceramic Society* **92**, 2674-2681 (2009).
- 17 Ou, D. R. *et al.* Evidence of intragranular segregation of dopant cations in heavily yttrium-doped ceria. *Electrochem. Solid State Lett.* **10**, P1-P3 (2007).
- 18 Steele, B. C. H. Appraisal of Ce_{1-y}Gd_yO_{2-y/2} electrolytes for IT-SOFC operation at 500 degrees C. *Solid State Ionics* **129**, 95-110 (2000).
- 19 Omar, S., Wachsman, E. D. & Nino, J. C. A co-doping approach towards enhanced ionic conductivity in fluorite-based electrolytes. *Solid State Ionics* **177**, 3199-3203 (2006).
- 20 Omar, S., Wachsman, E. D. & Nino, J. C. Higher conductivity Sm³⁺ and Nd³⁺ co-doped ceria-based electrolyte materials. *Solid State Ionics* **178**, 1890-1897 (2008).
- 21 Ou, D. R., Ye, F. & Mori, T. Defect clustering and local ordering in rare earth co-doped ceria. *Physical Chemistry Chemical Physics* **13**, 9554-9560 (2011).
- 22 van Herle, J., Seneviratne, D. & McEvoy, A. J. Lanthanide co-doping of solid electrolytes: AC conductivity behaviour. *Journal of the European Ceramic Society* **19**, 837-841 (1999).
- 23 Wang, F.-Y., Wan, B.-Z. & Cheng, S. Study on Gd³⁺ and Sm³⁺ co-doped ceria-based electrolytes. *Journal of Solid State Electrochemistry* **9**, 168-173, doi:10.1007/s10008-004-0575-0 (2005).
- 24 Yamamura, H., Katoh, E. & Kakinuma, K. Electrical conductivity in rare-earth cation co-doped ceria solid-solution systems. *Journal of the Ceramic Society of Japan* **110**, 1021-1024 (2002).
- 25 Park, K. & Hwang, H. K. Electrical conductivity of Ce_{0.8}Gd_{0.2-x}Dy_xO_{2-δ} (0 ≤ x ≤ 0.2) co-doped with Gd³⁺ and Dy³⁺ for intermediate-temperature solid oxide fuel cells. *Journal of Power Sources* **196**, 4996-4999 (2011).

- 26 Lee, K. T. *Comprehensive Development of High Performance Solid Oxide Fuel Cells for Intermediate and Low Temperature Applications* PhD thesis, University of Florida, (2010).
- 27 Chourashiya, M. G., Bharadwaj, S. R. & Jadhav, L. D. Synthesis and characterization of electrolyte-grade 10%Gd-doped ceria thin film/ceramic substrate structures for solid oxide fuel cells. *Thin Solid Films* **519**, 650-657 (2010).
- 28 Ding, C. S. *et al.* Effect of thickness of Gd_{0.1}Ce_{0.9}O_{1.95} electrolyte films on electrical performance of anode-supported solid oxide fuel cells. *Journal of Power Sources* **195**, 5487-5492 (2010).
- 29 McWhorter, S., Read, C., Ordaz, G. & Stetson, N. Materials-based hydrogen storage: Attributes for near-term, early market PEM fuel cells. *Current Opinion in Solid State and Materials Science* **15**, 29-38, doi:10.1016/j.cossms.2011.02.001 (2011).
- 30 MacLean, H. L. & Lave, L. B. Evaluating automobile fuel/propulsion system technologies. *Progress in Energy and Combustion Science* **29**, 1-69, doi:10.1016/s0360-1285(02)00032-1 (2003).
- 31 Data, J.-I. C. f. D. Vol. 34 - 0394.
- 32 Guo, X. & Waser, R. Electrical properties of the grain boundaries of oxygen ion conductors: Acceptor-doped zirconia and ceria. *Prog. Mater. Sci.* **51**, 151-210 (2006).
- 33 Data, J.-I. C. f. D. Vol. 10-0173.
- 34 Data, J.-I. C. f. D. Vol. 4-802.
- 35 Barsoukov, E. & Macdonald, J. R. *Impedance Spectroscopy: Theory, Experiment, and Applications*. (Wiley, 2005).
- 36 Kidner, N. J., Perry, N. H., Mason, T. O. & Garboczi, E. J. The brick layer model revisited: introducing the nano-grain composite model. *Journal of the American Ceramic Society* **91**, 1733-1746 (2008).
- 37 Gobel, M. C., Gregori, G., Guo, X. X. & Maier, J. Boundary effects on the electrical conductivity of pure and doped cerium oxide thin films. *Physical Chemistry Chemical Physics* **12**, 14351-14361 (2010).
- 38 Beckel, D. *et al.* Thin films for micro solid oxide fuel cells. *Journal of Power Sources* **173**, 325-345, doi:http://dx.doi.org/10.1016/j.jpowsour.2007.04.070 (2007).

- 39 Eason, R. *Pulsed Laser Deposition of Thin Films: Applications-Led Growth of Functional Materials*. (Wiley-Interscience, 2006).
- 40 Willmott, P. R., Spillmann, H. & Huber, J. R. Design and synthesis of novel thin films and structures by reactive crossed-beam laser ablation. *Journal of Materials Chemistry* **12**, 397-402 (2002).
- 41 Smith, H. M. & Turner, A. F. Vacuum Deposited Thin Films Using a Ruby Laser. *Appl. Optics* **4**, 147-& (1965).
- 42 Ashfold, M. N. R., Claeysens, F., Fuge, G. M. & Henley, S. J. Pulsed laser ablation and deposition of thin films. *Chemical Society Reviews* **33**, 23-31 (2004).
- 43 Boyd, I. W. Thin film growth by pulsed laser deposition. *Ceramics International* **22**, 429-434, doi:10.1016/0272-8842(95)00086-0 (1996).
- 44 Bäuerle, D. *et al.* Pulsed laser deposition. *Applied Physics A: Materials Science & Processing* **69**, S48 (1999).
- 45 Christen, H. M. & Eres, G. Recent advances in pulsed-laser deposition of complex oxides. *Journal of Physics: Condensed Matter* **20**, 264005 (2008).
- 46 Ohring, M. *Materials Science of Thin Films*. (Elsevier Science, 2001).
- 47 Chrisey, D. B. & Hubler, G. K. *Pulsed Laser Deposition of Thin Films*. (John Wiley & Sons, 1994).
- 48 Singh, R. K., Holland, O. W. & Narayan, J. Theoretical-Model for Deposition of Superconducting Thin-Films Using Pulsed Laser Evaporation Technique. *J. Appl. Phys.* **68**, 233-247 (1990).
- 49 Panzner, M., Dietsch, R., Holz, T., Mai, H. & Völlmar, S. Scale-up of pulsed laser deposition (PLD) for 4"-wafer coating. *Applied Surface Science* **96-98**, 643-648, doi:10.1016/0169-4332(95)00536-6 (1996).
- 50 Greer, J. A. & Tabat, M. D. Large-Area Pulsed-Laser Deposition - Techniques and Applications. *J. Vac. Sci. Technol. A-Vac. Surf. Films* **13**, 1175-1181 (1995).
- 51 Dam, B., Rector, J. H., Johansson, J., Kars, S. & Griessen, R. Stoichiometric transfer of complex oxides by pulsed laser deposition. *Applied Surface Science* **96-8**, 679-684 (1996).
- 52 Arnold, C. B. & Aziz, M. J. Stoichiometry issues in pulsed-laser deposition of alloys grown from multicomponent targets. *Applied Physics a-Materials Science & Processing* **69**, S23-S27 (1999).

- 53 Ohring, M. *The Materials Science of Thin Films*. (Acad. Press, 1992).
- 54 Stokes, R. J. & Evans, D. F. *Fundamentals of Interfacial Engineering*. (Wiley, 1997).
- 55 Thornton, J. A. High-Rate Thick-Film Growth. *Annu. Rev. Mater. Sci.* **7**, 239-260 (1977).
- 56 Kelly, P. J. & Arnell, R. D. Magnetron sputtering: a review of recent developments and applications. *Vacuum* **56**, 159-172 (2000).
- 57 Nefedov, A., Abromeit, A., Morawe, C. & Stierle, A. High-resolution x-ray scattering study of platinum thin films on sapphire. *J. Phys.-Condes. Matter* **10**, 717-730 (1998).
- 58 Nelson, J. B. & Riley, D. P. An Experimental Investigation of Extrapolation Methods in the Derivation of Accurate Unit-Cell Dimensions of Crystals. *Proceedings of the Physical Society of London* **57**, 160-177 (1945).
- 59 Giannuzzi, L. A. & Stevie, F. A. A review of focused ion beam milling techniques for TEM specimen preparation. *Micron* **30**, 197-204 (1999).
- 60 Kempshall, B. W., Giannuzzi, L. A., Prenitzer, B. I., Stevie, F. A. & Da, S. X. Comparative evaluation of protective coatings and focused ion beam chemical vapor deposition processes. *J. Vac. Sci. Technol. B* **20**, 286-290 (2002).
- 61 McHargue, C. J. *et al.* Etching of amorphous Al₂O₃ produced by ion implantation. *Nucl. Instrum. Methods Phys. Res. Sect. B-Beam Interact. Mater. Atoms* **127**, 596-598 (1997).
- 62 Wucherer, L. *Synthesis and characterization of electroceramic foams for 3-3 piezoelectric composites [electronic resource] / by Laurel Wucherer*. (University of Florida, 2008).
- 63 Kidner, N. J., Homrighaus, Z. J., Ingram, B. J., Mason, T. O. & Garboczi, E. J. Impedance/dielectric spectroscopy of electroceramics - Part 1: Evaluation of composite models for polycrystalline ceramics. *J. Electroceram.* **14**, 283-291 (2005).
- 64 Bellino, M. G., Lamas, D. G. & de Reza, N. E. W. Enhanced ionic conductivity in nanostructured, heavily doped ceria ceramics. *Adv. Funct. Mater.* **16**, 107-113 (2006).
- 65 Rupp, J. L. M. & Gauckler, L. J. Microstructures and electrical conductivity of nanocrystalline ceria-based thin films. *Solid State Ionics* **177**, 2513-2518 (2006).

- 66 Tuller, H. L. Ionic conduction in nanocrystalline materials. *Solid State Ionics* **131**, 143-157, doi:10.1016/s0167-2738(00)00629-9 (2000).
- 67 Swanson, M., Sunder, M., Tangtrakarn, N., Krishna, L. & Moran, P. D. Impact of the surface/interface on the ionic conductivity of thin film Gd-doped CeO₂. *Solid State Ionics* **189**, 45-49 (2011).
- 68 Huang, H., Gur, T. M., Saito, Y. & Prinz, F. High ionic conductivity in ultrathin nanocrystalline gadolinia-doped ceria films. *Applied Physics Letters* **89** (2006).
- 69 Rodrigo, K. *et al.* Electrical characterization of gadolinia-doped ceria films grown by pulsed laser deposition. *Applied Physics a-Materials Science & Processing* **101**, 601-607 (2010).
- 70 Joo, J. H. & Choi, G. M. Electrical conductivity of thin film ceria grown by pulsed laser deposition. *Journal of the European Ceramic Society* **27**, 4273-4277 (2007).
- 71 Abid, M., Paul-Boncour, V. & Touroude, R. Pt/CeO₂ catalysts in crotonaldehyde hydrogenation: Selectivity, metal particle size and SMSI states. *Appl. Catal. A-Gen.* **297**, 48-59 (2006).
- 72 Liu, W., Li, B., Liu, H. Q. & Pan, W. Electrical conductivity of textured Sm(3+) and Nd(3+) Co-doped CeO₂ thin-film electrolyte. *Electrochim. Acta* **56**, 3334-3337 (2011).
- 73 Tsuchiya, M., Bojarczuk, N. A., Guha, S. & Ramanathan, S. Microstructural effects on electrical conductivity relaxation in nanoscale ceria thin films. *J. Chem. Phys.* **130** (2009).
- 74 Kilner, J. A. & Waters, C. D. The Effects of Dopant Cation Oxygen Vacancy Complexes on the Anion Transport-Properties of Nonstoichiometric Fluorite Oxides. *Solid State Ionics* **6**, 253-259 (1982).
- 75 Dholabhai, P. P., Adams, J. B., Crozier, P. A. & Sharma, R. In search of enhanced electrolyte materials: a case study of doubly doped ceria. *Journal of Materials Chemistry* **21**, 18991-18997 (2011).
- 76 Guan, X. F., Zhou, H. P., Wang, Y. & Zhang, J. Preparation and properties of Gd³⁺ and Y³⁺ co-doped ceria-based electrolytes for intermediate temperature solid oxide fuel cells. *Journal of Alloys and Compounds* **464**, 310-316 (2008).
- 77 Sha, X. Q. *et al.* Study on La and Y co-doped ceria-based electrolyte materials. *Journal of Alloys and Compounds* **428**, 59-64 (2007).
- 78 Zheng, Y. F. *et al.* Effect of Dy on the properties of Sm-doped ceria electrolyte for IT-SOFCs. *Journal of Alloys and Compounds* **509**, 1244-1248 (2011).

- 79 Dikmen, S. Effect of co-doping with Sm(3+), Bi(3+), La(3+), and Nd(3+) on the electrochemical properties of hydrothermally prepared gadolinium-doped ceria ceramics. *Journal of Alloys and Compounds* **491**, 106-112 (2010).
- 80 Zheng, Y. F. *et al.* The effect of Sr on the properties of Y-doped ceria electrolyte for IT-SOFCs. *Journal of Alloys and Compounds* **486**, 586-589 (2009).
- 81 Singh, N., Singh, N. K., Kumar, D. & Parkash, O. Effect of co-doping of Mg and La on conductivity of ceria. *Journal of Alloys and Compounds* **519**, 129-135 (2012).
- 82 Shannon, R. D. Revised Effective Ionic-Radii and Systematic Studies of Interatomic Distances in Halides and Chalcogenides. *Acta Crystallographica Section A* **32**, 751-767 (1976).
- 83 Vegard, L. & Dale, H. Tests on mixed crystals and alloys. *Zeitschrift Fur Kristallographie* **67**, 148-162 (1928).
- 84 Tian, C. in *MRS Fall Meeting*.
- 85 Brugner, F. S. & Blumenth.Rn. Electrical Conductivity of Single-Crystal CeO₂. *Journal of the American Ceramic Society* **54**, 57-& (1971).
- 86 Yamamura, H. *et al.* Multiple doping effect on the electrical conductivity in the (Ce(1-x-y)La(x)My)O₂-delta (M = Ca, Sr) system. *Electrochemistry* **68**, 455-459 (2000).
- 87 Mori, T., Ikegami, T. & Yamamura, H. Application of a crystallographic index for improvement of the electrolytic properties of the CeO₂-Sm₂O₃ system. *J. Electrochem. Soc.* **146**, 4380-4385 (1999).
- 88 Kilner, J. A. & Brook, R. J. A Study of Oxygen Ion Conductivity in Doped Nonstoichiometric Oxides. *Solid State Ionics* **6**, 237-252 (1982).
- 89 Li, L. *et al.* Ionic conductivity across the disorder–order phase transition in the NdO_{1.5}–CeO₂ system. *Solid State Ionics* **221**, 15-21, doi:10.1016/j.ssi.2012.06.007 (2012).
- 90 Zhang, T. S., Ma, J., Kong, L. B., Hing, P. & Kilner, J. A. Preparation and mechanical properties of dense Ce_{0.8}W_{0.2}O₂-delta ceramics. *Solid State Ionics* **167**, 191-196 (2004).
- 91 Ou, D. R. *et al.* Microstructures and electrolytic properties of yttrium-doped ceria electrolytes: Dopant concentration and grain size dependences. *Acta Materialia* **54**, 3737-3746 (2006).

- 92 Ou, D. R. *et al.* Oxygen vacancy ordering in heavily rare-earth-doped ceria. *Applied Physics Letters* **89**, 171911-171913 (2006).
- 93 Zhang, T. S., Ma, J., Kong, L. B., Chan, S. H. & Kilner, J. A. Aging behavior and ionic conductivity of ceria-based ceramics: a comparative study. *Solid State Ionics* **170**, 209-217 (2004).
- 94 Mori, T. *et al.* Influence of particle morphology on nanostructural feature and conducting property in Sm-doped CeO₂ sintered body. *Solid State Ionics* **175**, 641-649 (2004).
- 95 Mori, T., Drennan, J., Lee, J. H., Li, J. G. & Ikegami, T. Oxide ionic conductivity and microstructures of Sm- or La-doped CeO₂-based systems. *Solid State Ionics* **154**, 461-466 (2002).
- 96 Vanderah, T. in *Electronic Materials and Applications* (Orlando, FL, 2011).
- 97 Chavan, S. V., Mathews, M. D. & Tyagi, A. K. Phase relations and thermal expansion studies in the CeO₂-NdO_{1.5} system. *Materials Research Bulletin* **40**, 1558-1568 (2005).
- 98 Parks, T. C. & Bevan, D. J. M. Mixed Oxides of Type Mo₂ (Fluorite)-Mo_{1.5} .6. Phase Relationships in Systems CeO₂-SmO_{1.5} and CeO₂-NdO_{1.5}. *Revue De Chimie Minerale* **10**, 15-28 (1973).
- 99 Li, B., Liu, Y., Wei, X. & Pan, W. Electrical properties of ceria Co-doped with Sm³⁺ and Nd³⁺. *Journal of Power Sources* **195**, 969-976 (2010).
- 100 Liu, Y., Li, B., Wei, X. & Pan, W. Citric-Nitrate Combustion Synthesis and Electrical Conductivity of the Sm³⁺ and Nd³⁺ Co-Doped Ceria Electrolyte. *Journal of the American Ceramic Society* **91**, 3926-3930 (2008).
- 101 Dikmen, S., Aslanbay, H., Dikmen, E. & Sahin, O. Hydrothermal preparation and electrochemical properties of Gd³⁺ and Bi³⁺, Sm³⁺, La³⁺, and Nd³⁺ codoped ceria-based electrolytes for intermediate temperature-solid oxide fuel cell. *Journal of Power Sources* **195**, 2488-2495 (2010).
- 102 Stephens, I. E. L. & Kilner, J. A. Ionic conductivity of Ce_{1-x}Nd_xO_{2-x/2}. *Solid State Ionics* **177**, 669-676 (2006).
- 103 Aneflous, L., Musso, J. A., Villain, S., Gavarrri, J. R. & Benyaich, H. Effects of temperature and Nd composition on non-linear transport properties in substituted Ce_{1-x}Nd_xO_{2-delta} cerium dioxides. *Journal of Solid State Chemistry* **177**, 856-865 (2004).

- 104 Fu, Y.-P. & Chen, S.-H. Preparation and characterization of neodymium-doped ceria electrolyte materials for solid oxide fuel cells. *Ceramics International* **36**, 483-490 (2010).
- 105 Grover, V., Achary, S. N. & Tyagi, A. K. Structural analysis of excess-anion C-type rare earth oxide: a case study with $Gd_{1-x}Ce_xO_{1.5+x/2}$ ($X = 0.20$ and 0.40). *Journal of Applied Crystallography* **36**, 1082-1084 (2003).
- 106 Chakraborty, K. R., Krishna, P. S. R., Chavan, S. V. & Tyagi, A. K. A neutron diffraction study on ceria-neodia solid solutions. *Powder Diffraction* **21**, 36-39 (2006).
- 107 Stephens, P. W. Phenomenological model of anisotropic peak broadening in powder diffraction. *Journal of Applied Crystallography* **32**, 281-289 (1999).
- 108 ASTM. (1996).
- 109 Heyn, E. *The Metallographist* **5**, 39-64 (1903).
- 110 Chourashiya, M. G., Patil, J. Y., Pawar, S. H. & Jadhav, L. D. Studies on structural, morphological and electrical properties of $Ce_{1-x}Gd_xO_{2-(x/2)}$. *Materials Chemistry and Physics* **109**, 39-44 (2008).
- 111 Etsell, T. H. & Flengas, S. N. Electrical Properties of Solid Oxide Electrolytes. *Chemical Reviews* **70**, 339-& (1970).
- 112 Balazs, G. B. & Glass, R. S. Ac-Impedance Studies of Rare-Earth-Oxide Doped Ceria. *Solid State Ionics* **76**, 155-162 (1995).
- 113 Reis, S. L., Souza, E. C. C. & Muccillo, E. N. S. Solid solution formation, densification and ionic conductivity of Gd- and Sm-doped ceria. *Solid State Ionics* **192**, 172-175 (2011).
- 114 Perez-Coll, D., Sanchez-Lopez, E. & Mather, G. C. Influence of porosity on the bulk and grain-boundary electrical properties of Gd-doped ceria. *Solid State Ionics* **181**, 1033-1042 (2010).
- 115 Harwig, H. A. & Gerards, A. G. Electrical-Properties of Alpha, Beta, Gamma and Delta Phases of Bismuth Sesquioxide. *Journal of Solid State Chemistry* **26**, 265-274 (1978).
- 116 Yashima, M. & Ishimura, D. Crystal structure and disorder of the fast oxide-ion conductor cubic Bi_2O_3 . *Chemical Physics Letters* **378**, 395-399 (2003).
- 117 Bevan. in *4th Conference on Rare-Earths Research*. P441.

- 118 Ye, F. *et al.* Simulation of ordering in large defect clusters in gadolinium-doped ceria. *Solid State Ionics* **179**, 1962-1967 (2008).
- 119 Toshiyuki Mori, J. D., Yarong Wang, Graeme Auchterlonie, Ji-Guang Li, Anya Yago. Influence of nano-structural feature on electrolytic properties in Y2O3 doped CeO2 system. *Science and Technology of Advanced Materials* **4**, 213 (2003).
- 120 Omar, S. *Enhanced Ionic Conductivity of Ceria-based Compounds for the Electrolyte Application in SOFCs* Ph.D. thesis, University of Florida, (2008).
- 121 Bachelet, R. *et al.* Enhanced thermal stability of Pt electrodes for flat epitaxial biferroic-YMnO3/Pt heterostructures. *Applied Physics Letters* **95** (2009).

BIOGRAPHICAL SKETCH

Robert Kasse was born at Fort Wainwright, Alaska in 1989. He has since lived in North Carolina, Indiana, Georgia, Pennsylvania, and Germany before ending up in Florida where he graduated from Niceville Senior High School in 2008. Robert began attending the University of Florida the following August and graduated with a B.S. in Materials Science and Engineering, specializing in ceramics, and a minor in Business Administration in May of 2012. During the summer of 2011, Robert was awarded the SMART Scholarship for Service by the Department of Defense, with the 96th Test Wing at Eglin Air Force Base as his sponsoring facility. He will begin working at Eglin in fulfillment of his two year obligation shortly after graduating with his master's degree.